Fall 2007

Computational study of flow over elliptic airfoils for rotor/wing unmanned aerial vehicle applications

Timothy William Assel

Department:

COMPUTATIONAL STUDY OF FLOW OVER ELLIPTIC AIRFOILS FOR ROTOR/WING UNMANNED AERIAL VEHICLE APPLICATIONS

BY

TIMOTHY WILLIAM ASSEL

A THESIS

PRESENTED TO THE FACULTY OF THE GRADUATE SCHOOL OF THE

UNIVERSITY OF MISSOURI-ROLLA

IN PARTIAL FULFILLMENT OF THE REQUIREMENTS FOR THE DEGREE

MASTER OF SCIENCE IN AEROSPACE ENGINEERING

2007

APPROVED BY

_____	_____
DR. FATHI FINAISH, ADVISOR	DR. D.W. RIGGINS

_____

DR. K.M. ISAAC

ABSTRACT

Elliptic airfoil geometries have been used extensively in the development of Rotor/Wing aircraft. Most recently elliptic airfoils have been employed in the development of Rotor/Wing Unmanned Aerial Vehicles (UAVs). UAVs play an expanding role in military and civil applications. Much research has been conducted recently in the area of Vertical Take-off and Landing (VTOL) UAVs, and a significant amount of research has gone into the development of a Rotor/Wing UAV for VTOL applications. However, a lack of research has been published regarding the aerodynamic performance and flow characteristics of elliptic airfoils in parameter ranges which would be applicable in the design and development of Rotor/Wing UAVs. This data is of significant importance to Rotor/Wing UAV design and development due to the complexity of flow developments about elliptic airfoils including: flow separation over the leading edge, flow reattachment over suction surface of the airfoil, and vortex shedding downstream of the airfoil. The purpose of this study will be to conduct a parametric investigation on the performance of elliptic airfoils for Rotor/Wing Unmanned Aerial Vehicles. The objective of this study is to conduct a two-dimensional, aerodynamic analysis on a various elliptic airfoil parameters, compare the results of the analysis with theoretical predictions and experimental results, and evaluate handling and performance characteristics of Rotor/Wing UAVs during hover, transition, and forward flight. It is hoped that the results of this study would provide a better understanding of the aerodynamic performance and flow characteristics of elliptic airfoils, and that the results of this study would be employed in the research and development of future Rotor/Wing technology and VTOL UAV designs.

ACKNOWLEDGMENTS

I would first like to thank my advisor, Dr. Fathi Finaish, who has devoted time and patience to guide me throughout my research, has spent years working with me to develop a basis of knowledge and skills for investigation into ideas and presentation of results, and has provided the wisdom, the insight and the opportunity for intellectual independence and creativity which has made this thesis a possibility.

I am also very grateful to the members of my committee: Dr. Issac and Dr. Riggins, who have been mentors during my college career and have provided the encouragement and inspiration that has brought me through the completion of this study.

I would also like to thank the Department of Mechanical and Aerospace Engineering at the University of Missouri-Rolla for providing the education, facilities and funding necessary for me to complete my academic studies.

I would like to express a deep appreciation for my fellow researchers and friends in the UMR Flight Simulation Laboratory who assisted and educated me in the most random, diverse, and unexpected ways; including: Keith Norton, Peter Cross, Josiah Elliot, Tyler Winter and Ben Bettis.

Lastly, I would like to express my greatest thankfulness for my family, who have always been there for me with support, encouragement and wisdom; especially my Father, who from my very beginning has taught me the value of hard work and determination, the importance of learning and common sense and, most importantly, to have faith in God and to trust always in His wisdom and grace.

TABLE OF CONTENTS

Page

ABSTRACT iii
ACKNOWLEDGMENTS iv
LIST OF ILLUSTRATIONS vii
LIST OF TABLES xi
NOMENCLATURE xii
1. INTRODUCTION 1
1.1. RECENT ADVANCEMENTS IN UAV TECHNOLOGY 1
1.1.1. Expanding Interest in UAVs. 1
1.1.2. Brief Survey of VTOL UAVs Currently in Development. 1
1.2. LITERATURE SURVEY 6
1.2.1. Brief History of Rotor/Wing Research. 7
1.2.2. Recent Developments in Canard Rotor/Wing Technology 8
1.2.3. Studies in Flow over Elliptic Airfoils and Cylinders 10
1.3. SCOPE OF THIS STUDY 13
1.3.1. The Flow Problem and Selected Parameter Range 14
1.3.2. Validation of Methodology 155
2. COMPUTATIONAL APPROACH 17
2.1. FLOWFIELD SIMULATION ABOUT AN AIRFOIL 17
2.1.1. Flowfield Grid Generation Technique ....**Error! Bookmark not defined.**
2.1.1.1 Surface Geometry Definition Technique. 17
2.1.1.2 Surface Grid Generation Technique. 18
2.1.1.3 Volume Grid Generation Technique. 21
2.1.2. Flowfield Solution Methodology .....**Error! Bookmark not defined.**
2.1.2.1 Description of Flow Solver 26
2.1.2.2 Flow Input Parameters 26
2.1.2.3 Boundary Conditions 26
2.1.2.4 Turbulence Models 27
2.1.2.5 Post-Processing 27

2.1.2.5.1 Numerical Analysis 27
2.1.2.5.2 Visual Analysis 28
3. VALIDATION OF METHODOLOGY 29
3.1. VALIDATION TEST CASE PROCEDURES 29
3.1.1. Validation Test Case Grid Generation 29
3.1.2. Flow Solver Input Parameters 30
3.2. RESULTS OF CFD ANALYSIS FOR A 16% ELLIPTIC AIRFOIL 31
3.2.1. Note on Laminar Separation Bubble 43
3.3. EXPERIMENTAL DATA FOR A 16% THICK ELLIPTIC AIRFOIL 43
3.4. COMPARISON OF CFD RESULTS WITH EXPERIMENTAL DATA 47
3.4.1. Note on Pitching Moment Coefficient 53
3.5. CONCLUDING REMARKS 54
4. RESULTS AND DISCUSSION 55
4.1. PARAMETRIC STUDY OF ELLIPTIC AIRFOIL PERFORMANCE 55
4.1.1. Influence Reynolds Number on Airfoil Lift Characteristics 55
4.1.2. Influence of Reynolds Number on Airfoil Drag Characteristics 61
4.1.3. Influence of Reynolds Number on Lift to Drag Performance 63
4.1.4. Influence of Reynolds Number on Pitching Moment 64
4.1.5. Influence of Reynolds Number on Flow Developments 65
4.1.6. Influence of Thickness Ratio on Airfoil Lift Characteristics 73
4.1.7. Influence of Thickness Ratio on Airfoil Drag Characteristics 77
4.1.8. Influence of Thickness Ratio on Lift to Drag Performance 79
4.1.9. Influence of Thickness Ratio on Pitching Moment 81
4.1.10. Influence of Thickness Ratio on Flow Developments 82
4.2. CONCLUSIONS 93
5. CONCLUSIONS AND OUTLOOK 98
5.1. CONCLUSIONS 98
5.2. FUTURE WORK 99
BIBLIOGRAPHY 102
VITA 105

LIST OF ILLUSTRATIONS

Figure Page

1.1 Photo of the A160 Hummingbird on an airport taxiway near Victorville, CA..... 2

1.2 Photo of MQ-8B Fire Scout in Hover..... 3

1.3 Goldeneye in Transition from Hover to Forward Flight..... 4

1.4 Depiction of iSTAR UAV showing transition from hover to forward flight 4

1.5 Photo of Bell Eagle Eye in Hover..... 5

1.6 Boeing X-50A in hover mode..... 6

1.7 Photo of Sikorsky S-72 modified as X-Wing testbed..... 7

1.8 Top, front and side view schematic of Boeing X-50A Dragonfly..... 8

1.9 Schematic of CRW conversion process from hover to fixed-wing flight..... 10

1.10 Plot of wake vortex structures taken from Reference 21..... 12

1.11 Schematic of flow configuration (not to scale)..... 14

2.1 Surface Geometry of Elliptical Airfoil created in AGPS..... 18

2.2 Extract-Grid Point Distribution Methods available in AGPS..... 19

2.4 Surface Grid generated in AGPS using Linear Point Distrubution 20

2.5 Surface Grid generated in AGPS using Cosine Point Distribution..... 21

2.6 Comparison of an Unstructured Grid (a) and a Structured Grid (b)..... 21

2.7 Tecplot rendering of a non-orthoganal, structured, volume grid showing the viscous region (top left), focus region (top right) and outer region (bottom)..... 24

2.8 Computer Screenshots of a C-grid volume grid generated about a NACA 0009 surface grid using Hypgen showing far field, close-up, and boundary layer views 25

3.1 Surface grid generated in AGPS with 250 points in curvature point distribution 30

3.2 Plot of flow development over an elliptic airfoil showing pressure distribution and streamlines.. 31

3.3 Plot of flow development over an elliptic airfoil showing pressure distribution and streamlines.. 32

3.4 Plot of flow development over an elliptic airfoil showing pressure distribution and streamlines.. 32

3.5 Plot of flow development over an elliptic airfoil showing pressure distribution and streamlines.. 33

3.6 Plot of flow development over an elliptic airfoil showing pressure distribution and streamlines. 33

3.7 Plot of vortex development downstream of an elliptic airfoil showing pressure distribution and streamlines. 34

3.8 Plot of vortex development downstream of an elliptic airfoil showing pressure distribution and streamlines. 35

3.9 Plot of vortex development downstream of an elliptic airfoil showing pressure distribution and streamlines. 35

3.10 Plot of vortex development downstream of an elliptic airfoil showing pressure distribution and streamlines. 36

3.11 Plot of vortex development downstream of an elliptic airfoil showing pressure distribution and streamlines. 36

3.12 Plot of normalized velocity vectors in the separated flow region of an elliptic airfoil. 37

3.13 Plot of normalized velocity vectors in the separated flow region of an elliptic airfoil. 37

3.14 Plot of normalized velocity vectors in the separated flow region of an elliptic airfoil. 38

3.15 Plot of normalized velocity vectors in the separated flow region of an elliptic airfoil. 38

3.16 Plot of normalized velocity vectors in the separated flow region of an elliptic airfoil.. 39

3.17 Plot of surface pressure distribution around an elliptic airfoil. 40

3.18 Plot of surface pressure distribution around an elliptic airfoil. 40

3.19 Plot of surface pressure distribution around an elliptic airfoil. 41

3.20 Plot of surface pressure distribution around an elliptic airfoil. 41

3.21 Plot of surface pressure distribution around an elliptic airfoil. 42

3.22 Close-up of boundary layer velocity profiles within a laminar separation bubble developed near the airfoil trailing edge. 43

3.23 Wake vortex structure with streamlines [Obtained from Reference 21] 44

3.24 Wake vortex structure with streamlines [Obtained from Reference 21] 44

3.25 Wake vortex structure with streamlines [Obtained from Reference 21] 44

3.26 Wake vortex structure with streamlines [Obtained from Reference 21] 45

3.27 Wake vortex structure with streamlines [Obtained from Reference 21] 45

3.28 Surface pressure distributions at various angles of attack [Obtained from

Reference 21] 46
3.29 Comparison of experimental and CFD flowfield data. 47
3.30 Comparison of experimental and CFD flowfield data. 47
3.31 Comparison of experimental and CFD flowfield data. 48
3.32 Comparison of experimental and CFD flowfield data. 48
3.33 Comparison of experimental and CFD flowfield data. 48
3.34 Flow characteristics over an elliptic section from Hoerner [28] 50
3.35 Lift coefficient with respect to angle of attack [Obtained from Reference 21] 51
3.36 Lift coefficient with respect to angle of attack obtained using FOMOCO 51
3.37 Drag coefficient with respect to angle of attack [Obtained from Reference 21] 52
3.38 Drag coefficient with respect to angle of attack obtained using FOMOCO 52
3.39 Pitching Moment Coefficient with respect to Angle of Attack [Obtained from Reference 21] 53
3.40 Pitching Moment Coefficient with respect to Angle of Attack obtained using FOMOCO 53
4.1 Dependence of Lift Coefficient on angle of attack for a range of Reynolds number between $1*10^5$ and $8*10^6$. 56
4.2 Dependence of Lift Coefficient on angle of attack for a range of Reynolds numbers between $1*10^5$ and $8*10^6$. 57
4.3 Dependence of Average Lift Slope on Reynolds number, for $\alpha \varepsilon [0°, 6°]$. 58
4.4 Dependence of Stall Angle on Reynolds number for a range of Reynolds numbers between $1*10^5$ and $2*10^6$. 59
4.5 Dependence of Maximum Lift Coefficient on Reynolds number for a range of Reynolds numbers between $1*10^5$ and $8*10^6$. 60
4.6 Dependence of Drag Coefficient on angle of attack for a range of Reynolds numbers between $1*10^5$ and $8*10^6$. 61
4.7 Dependence of drag coefficient on angle of attack for a range of Reynolds numbers between $1*10^5$ and $2*10^6$. 62
4.8 Dependence of Lift to Drag Ratio on Angle of Attack and Reynolds number. 63
4.9 Dependence of Maximum Observed Lift to Drag Ratio on Reynolds number. 64
4.10 Dependence of Pitching Moment Coefficient on Reynolds number. 65
4.11 Pressure distribution and flow streamlines around elliptic airfoil for various Reynolds numbers. 66
4.12 Streamline visualizations of flow developments close to leading edge. 67

4.13 Plots of surface pressure distribution showing pressure drops caused by separation bubbles over the leading edge. 69

4.14 Streamlines visualizations of vortex developments near trailing edge. 70

4.15 Pressure distribution and flow streamlines around elliptic airfoil for various Reynolds numbers. 72

4.16 Dependence of Lift Coefficient on angle of attack for a range of thickness ratios between 5% and 25%. 73

4.17 Dependence of Lift Coefficient on angle of attack for a range of thickness ratios between 5% and 25%. 74

4.18 Dependence of average lift slope on thickness ratio for angles of attack between 1° and 5° 76

4.19 Dependence of stall angle on thickness ratio for a range of thickness ratios between 5% and 25%. 76

4.20 Dependence of maximum lift coefficient on thickness ratio for a range of thickness ratios between 5% and 25%. 77

4.21 Dependence of Drag Coefficient on angle of attack for a range of thickness ratios between 5% and 25%. 78

4.22 Dependence of Drag Coefficient on angle of attack for a range of thickness ratios between 5% and 25%. 79

4.23 Dependence of Lift to Drag Ratio on Angle of Attack for a Range of Thickness Ratios between 5% and 25%. 80

4.24 Dependence of Maximum Observed L/D on Thickness Ratio. 80

4.25 Dependence of Pitching Moment Coefficient on Thickness Ratio. 81

4.26 Pressure distribution and flow streamlines around elliptic airfoil for various Reynolds numbers. 82

4.27 Streamline visualizations of flow developments near the airfoil leading edge. 84

4.28 Streamline visualizations of flow developments near the airfoil leading edge. 85

4.29 Plots of surface pressure distribution showing pressure drops caused by separation bubbles over the leading edge. 86

4.30 Streamlines visualizations of vortex developments near trailing edge. 87

4.31 Pressure distribution and flow streamlines around elliptic airfoil for various Reynolds numbers. 89

4.32 Pressure distribution and flow streamlines around elliptic airfoil for various Reynolds numbers. 91

LIST OF TABLES

Table Page

1.1 Selected Parameter Range..... 15

3.1 Comparison of Flow Separation and Vortex Structure…….……49

4.1 Lift slopes for the investigated range of Reynolds numbers and average Lift Slope for attack angles between 0 and 6 degrees..... 58

4.2 Lift slopes for angles of attack between 1° and 5° and a range of thickness ratios between 5% and 25%. 75

NOMENCLATURE

Symbol	Description
Re	Reynolds Number
α	Angle of Attack
t/c	Thickness Ratio
M_∞	Mach Number
C_L	Lift Coefficient
C_D	Drag Coefficient
$C_{L,max}$	Maximum Lift Coefficient
L/D	Lift to Drag Ratio
C_M	Pitching Moment Coefficient
C_M	Pitching Moment Coefficient

1. INTRODUCTION

1.1. RECENT ADVANCEMENTS IN UAV TECHNOLOGY

Developments in Unmanned Aerial Vehicle (UAV) Technology have seen a recent surge in interest and effort due to increased reliance on remotely piloted and autonomous air vehicles in military and homeland security applications. Overall, the extent and intensity of studies on new and emerging areas of UAV research has experienced rapid growth in the aerospace industry and in the academic sector.

1.1.1. Expanding Interest in UAVs. Unmanned Aerial Vehicles have gained a crucial role in modern military and civil tactics. Operations in which UAVs have been deployed include reconnaissance, surveillance, target acquisition, electronic warfare and bomb damage assessment. Currently, more than three dozen nations are active in developing UAV technology, and the leader in advancements of UAV technology is the US. Over five dozen different programs including the American Predator, Global Hawk and Shadow make up the United States' arsenal of UAV [1].

Notably, the greatest benefit obtained from employing UAVs in military or homeland security applications is removing the necessity for a human operator to enter into hazardous or risky situations. In addition, advancements in unmanned technology allow UAVs to be less expensive, higher performing, and more maneuverable. UAVs do not require life-support systems and are not limited by pilot G-force tolerance. These advantages have accelerated UAVs to the forefront of research and development. Interest in UAVs has expanded to emerging civil applications including: pipeline and powerline monitoring, search and rescue, wildlife and forest fir observation, and scientific observation [1].

1.1.2. Brief Survey of VTOL UAVs Currently in Development. One area of interest that has seen recent growth and in which there is great potential for research innovation has been Vertical Takeoff and Landing (VTOL) UAVs. A significant number of military warfare and homeland security applications require that the UAV takeoff and land in field conditions where there is little or no space available for ground roll. These conditions necessitate the need for UAVs which can either takeoff and land vertically, or can be launched and recovered by ground support systems. Launch and recovery systems

are typically large, unwieldy and add additional cost to the overall system. Though bulky launch and recovery equipment is not required for aircraft which are capable of vertical takeoff and landing, current VTOL UAV designs are not as efficient in forward flight and have the added difficulty of transitioning from hover to forward flight and vice versa. In order to overcome these obstacles, much more research into emerging VTOL technologies is still needed.

A diverse group of VTOL UAV design concepts are rising to the forefront of industry research and development. Major contenders in the VTOL UAV lineup include rotorcraft, ducted fans, and tilt rotors. Rotorcraft UAVs generally consist of traditional helicopter configurations. One of the leading rotorcraft UAV is the A160 Hummingbird. The hummingbird was originally developed by Frontier, which was purchased in 2004 by The Boeing Company, who is currently developing the vehicle. Shown in Figure 1.1, below, the autonomously-flown A160 will break helicopter barriers by reaching higher altitudes, increasing hover time, and traveling greater distances at high velocities, “The aircraft's unique characteristics address current and emerging requirements of the U.S. armed forces, the U.S. Department of Homeland Security, and international military and security organizations.” [3].

Figure 1.1 Photo of the A160 Hummingbird on an airport taxiway near Victorville, CA.

Another notable unmanned helicopter is the Northrop Grumman MQ-8B Fire Scout. With derivatives for both Navy and the Army, the Fire Scout has the ability to takeoff and land autonomously from any aviation capable warship, at unprepared and unimproved landing zones, and in close proximity to combat personnel and Tactical Operations Centers [4]. Shown in Figure 1.2, below, the Fire Scout has the versatility to conduct such missions as: surveillance, target acquisition, target tracking and designation, and battle damage assessment [5].

Figure 1.2 Photo of MQ-8B Fire Scout in Hover

A growing number of ducted fan VTOL UAVs are currently under development. Ducted Fan UAV designs which have had good success consist of tail-sitters in which a fan or propeller is surrounded by duct. These configurations include Aurora's Goldeneye UAV and Allied Aerospace's iSTAR Miniature UAV. The Goldeneye-80, Aurora's most recently developed Tactical System for DARPA, is designed for low-cost RSTA (reconnaissance, surveillance, and target acquisition) missions [6]. Shown in Figure 1.3, below, Goldeneye can "the GoldenEye 80 takes off and lands vertically but can transition to horizontal flight using wings." [7].

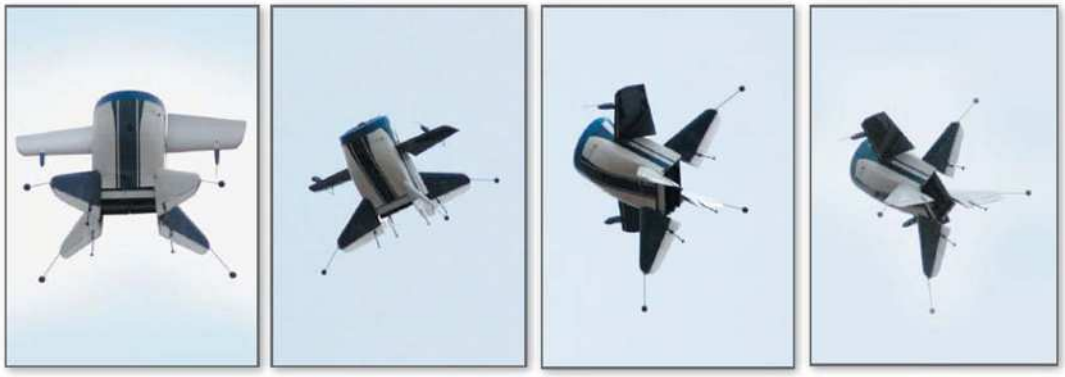

Figure 1.3 Goldeneye in Transition from Hover to Forward Flight

The iSTAR Miniature UAV, under development by Allied Aerospace, is a small lift augmented ducted fan which can takeoff vertically and transition into forward flight. The iSTAR is primarily a surveillance vehicle with a camera mounted on top, but the vehicle also offers high speed horizontal flight to conduct a variety of challenging missions. Shown below, in Figure 1.4, the iSTAR uses the duct surrounding the propeller as an airfoil in forward flight, providing the necessary lift.

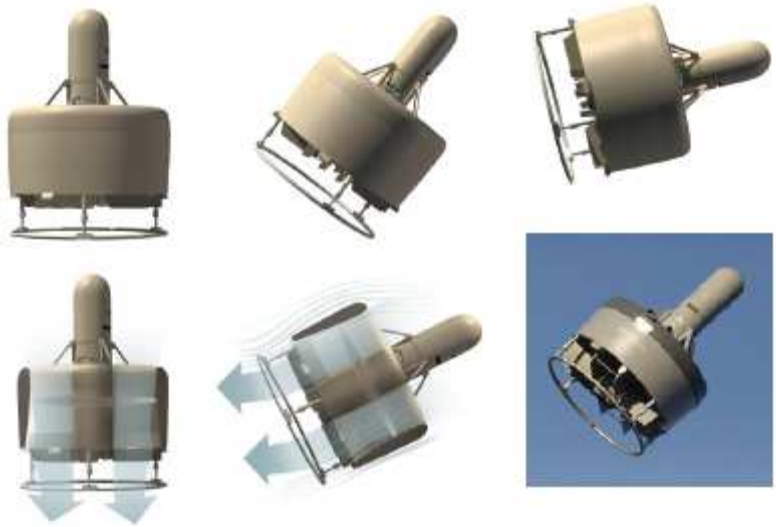

Figure 1.4 Depiction of iSTAR UAV showing transition from hover to forward flight

Only one tilt rotor UAV has been developed so far, which has been the Bell Eagle Eye UAS. This UAV has rotors mounted at each of two wing tips, which can rotate from vertical orientation during takeoff, hover, and landing to horizontal orientation for high speed forward flight. “The Eagle Eye’s ability to takeoff and land vertically and then seamlessly transition to forward flight as a high speed fixed wing aircraft provides operational advantages to land and sea commanders that cannot be found with any other UAV product.” [8].

Figure 1.5 Photo of Bell Eagle Eye in Hover

An unconventional VTOL UAV which has also played a leading role in current research and development efforts has been the Boeing Canard Rotor/Wing (CRW) UAV. “The Canard Rotor/Wing (CRW) program explores innovative VTOL technologies and concepts with the potential for significant performance improvements that would satisfy stressing mission needs.” [9]. The CRW UAVs revolutionary concept combines the hover capabilities of a rotorcraft with the forward flight qualities of a fixed-wing aircraft [10].

Shown in Figure 1.6, below, this pilotless aircraft has a specially designed rotor which can lock into a fixed-wing position for jet cruise.

Figure 1.6 Boeing X-50A in hover mode

1.2. LITERATURE SURVEY

The survey of currently under development VTOL UAVs revealed that new and innovative design concepts have proven to be reliable, safe, and technologically advanced for a variety of critical and necessary missions. These ground-breaking prototypes and technology demonstrators have laid a foundation for future breakthroughs in VTOL UAV technology. Perhaps one of the most exciting and pioneering technology demonstrator is the Boeing X-50A Dragonfly. However, this vehicle requires a very complex and hazardous method for transitioning from hover to forwards flight. During conversion from rotorcraft to fixed-winged aircraft, the canard wing and horizontal tail provide necessary lift while the rotor blade stops turning and functions as a fixed wing [11]. Although much research and prototype flight testing have already been conducted, a demonstration from hover to forward flight has not yet been completed successfully. Clearly, a substantial amount of research and analysis into Rotor/Wing flight

characteristics is still needed if enhanced CRW platforms are going to be available for service in the projected 2012 timeframe [11].

1.2.1. Brief History of Rotor/Wing Research. The bulk of research completed on the CRW design concept has been conducted by Boeing Phantom Works, previously by McDonnell Douglas, and is built upon work on the Sikorsky X-Wing [12]. The Sikorsky S-72 X-Wing, shown in Figure 1.7, below, was a hybrid vehicle with a four-blade rotor which also served as a fixed wing during forward flight [13].

Figure 1.7 Photo of Sikorsky S-72 modified as X-Wing testbed

Various companies, including Boeing, participated in the X-Wing program along with Sikorsky, the primary contributor. One of the main complications with the X-Wing was the use of circulation control for varying the lift on the Rotor/Wing blades. Also, the rotor/wing needed to provide all necessary lift during conversion from rotor to fixed wing. The X-Wing concept for conversion from rotor to fixed wing was confirmed with wind tunnel testing, however, a program funded to demonstrate the concept on a manned aircraft was terminated before an attempt at conversion could be made [14].

Work on the rotor/wing concept was rejuvenated in the early 90's due to a rise of interest from both the military and commercial sectors for high-speed rotorcraft which prompted NASA to fund the McDonnell Douglas Helicopter Company to investigate technology for a high speed Hughes Rotor/Wing configuration. Sizing Studies for the investigation showed that the Rotor/Wing concept was the best concept for a variety of

missions. The superiority of the Rotor/Wing concept displayed in the investigation justified a renewal of interest into the development of a successful Rotor/Wing aircraft. “This revisit of the Hughes Rotor/Wing directly led to the formulation of the Canard Rotor/Wing concept.” [14].

As a result of the extensive research conducted by McDonnell Dougles, later Boeing, the Rotor/Wing concept has broken through difficulties of historical stopped rotor vehicles and evolved into a new paradigm. Previous concepts used the rotor/wing to provide lift in all modes of flight including: rotary, transition, and fixed wing. The CRW concept is not dependent on the rotor/wing during transition because the canard wing and horizontal tail can provide enough lift and control to supplement loss of lift by the main rotor/wing during its conversion to fixed-wing mode. This new concept allows the CRW to build on proven technologies from past designs and employ innovative ideas to accommodate for known obstacles [14].

1.2.2. Recent Developments in Canard Rotor/Wing Technology. Key features of the current CRW concept include: the reaction-drive system, the rotor/wing, and the conversion process. Figure 1.8, below, shows top, side and front view of the CRW configuration.

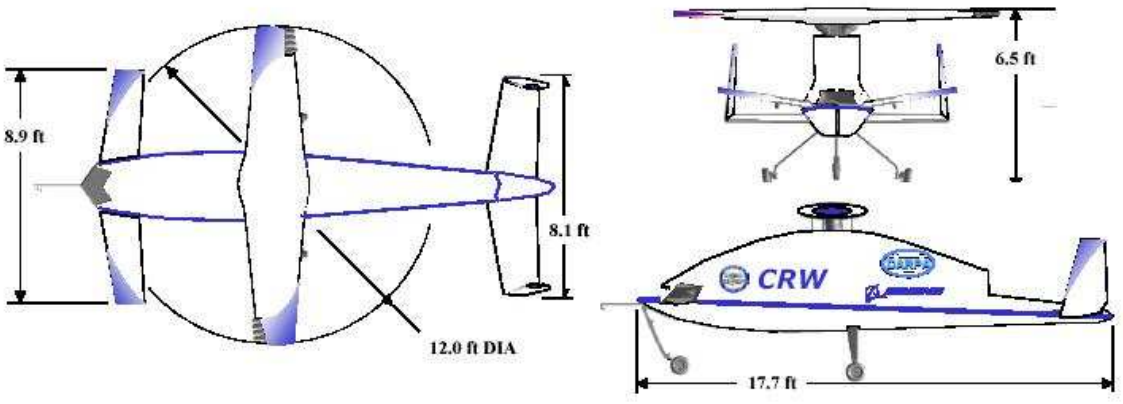

Figure 1.8 Top, front and side view schematic of Boeing X-50A Dragonfly

Using a reaction-drive system to propel a rotor through the air with jet nozzles blowing exhaust out of the rotor tips, as opposed to spinning the rotor with torque from a shaft drive system, is a proven technology implemented on a previous experimental helicopter programs. The fact that the reaction-drive system is less effective than shaft drive in rotary mode is outweighed, in this case, by two main benefits. Firstly, reaction-drive systems do not need the heavy transmissions and drive systems necessary for high-speed proprotor driven configurations. This significant decrease in system weight allows reaction-drive configurations to achieve higher performance in low-speed and high-speed modes. Secondly, a single jet engine is capable of providing propulsive power in both rotary-wing and fixed wing modes. Also, the reaction-drive system has the added, high-speed mode advantage of eliminating the anti-torque system needed by conventional rotorcraft. Anti-torque systems incur unwanted drag in high-speed flight, while the reaction-drive system allows for full utilization of turbofan thrust at high-speeds during fixed-wing mode. Overall, the reaction drive system reduces unnecessary complexity typically associated with high-speed, convertible aircraft [14].

In a rotor/wing configuration, the trailing edge of the retreating blade in rotary-wing flight converts into the leading edge of the fixed wing in forward flight. In order to accommodate for this hindrance, the airfoil sections of the rotor/wing need to have blunt leading and trailing edges. This requirement is fulfilled by employing an elliptic airfoil, however, the blunt trailing edge incurs more profile drag than a sharp trailing edge on a typical airfoil. Research into techniques for reducing the drag, ranging from active flow control to deployable flaps, continues to be investigated. Some of these techniques have potential for significant improvements in drag reduction. However, the added complexity of most drag reduction techniques would infringe upon the overall simplicity of the CRW system [14].

A defining characteristic of the CRW is the offloading of the rotor/wing during conversion. To accomplish this, the canard wing and horizontal tail must provide all necessary lift during transition. High-lift devices located on the canard and horizontal tail provide the added lift during conversion and also serve as control surfaces during fixed-wing mode. Since the canard and tail lifting surfaces are de-coupled from the rotor, they can move independently to maintain stability and level altitude. As the power required to

rotate the rotor decreases with the offloading of lift onto the canard and tail, jet engine exhaust gases can be diverted to a rear jet nozzle to provide the propulsive force for forward flight. As a result of the increase in forward thrust, the aircraft is accelerated to conversion speed while a combination of aerodynamic and mechanical braking slows the rotor to a stopped position. Once the rotor is fully locked into the fixed-wing position, aerodynamic loading is transferred from the canard and tail to the rotor/wing, completing the conversion process. Overall, the CRW conversion process, shown below in Figure 1.9, reduces unwanted forces and moments acting on the rotor disc while the rotor is decelerating to a fixed position [14].

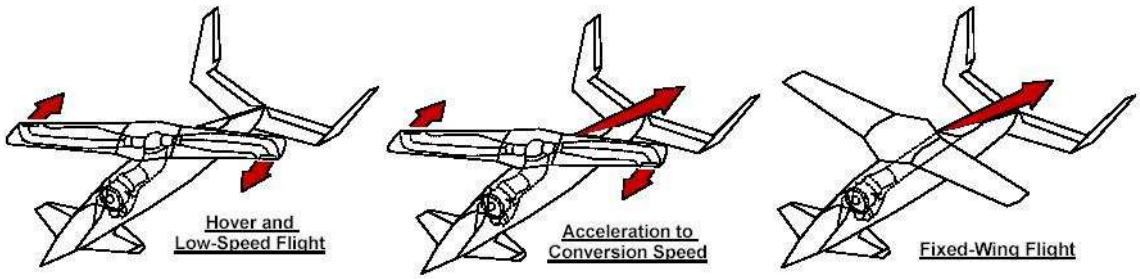

Figure 1.9 Schematic of CRW conversion process from hover to fixed-wing flight

Although the CRW conversion process provides significant benefits, non-ideal load conditions on the rotor, caused by wind gusts or maneuvers during transition, can ultimately become hazardous to the vehicle. Testing and analysis of the CRW indicated that a significant amount of transient aerodynamic loads did affect the rotor/wing during conversion even though all lift was transferred to the canard wing and horizontal tail. This occurs because the rotor is decelerating through a non-uniform free stream, and thus transfers unsteady loads to the airframe. “Prediction of the amplitude of these unsteady loads is an important part of sizing the control surfaces and actuators of the flight control system.” [15].

1.2.3. Studies in Flow over Elliptic Airfoils and Cylinders. One difficulty for predicting aerodynamic loading on the rotor/wing is due to vortex shedding off the blunt trailing edge of the elliptic airfoil. Flow separation over this sharply curved trailing edge, as opposed to attached flow over a gradually curved sharp trailing edge, causes vortices

to form directly aft of the airfoil. This creates a turbulent flow field which is difficult to predict using conventional methods. A significant amount of work has been conducted to study flow past elliptic cylinders. Early studies utilized wind tunnel testing and theoretical analysis to study aerodynamic forces, boundary layers, and velocity distribution [16] – [19], while, more recently, numerical methods have been employed to study vortex structures aft of elliptic cylinders for a limited range of very small Reynolds numbers, between 30 and 200 [20]. This range of Reynolds numbers would not be applicable in UAV design. Some work with elliptic airfoils which could be applied in UAV design has been conducted. Kwon and Park have investigated vortex flow structures and aerodynamic characteristics using wind tunnel testing for a single thickness ratio and Reynolds number [21]. Also, turbulent viscous flow over elliptic cylinders has been solved using two-dimensional, incompressible, Navier-Stokes equations for a limited range of thickness ratios, between 60% and 120%, and Reynolds numbers, between 200 and 1,000 [22].

Studies into turbulent viscous flow over elliptic cylinders have concluded that thickness ratio and Reynolds number both have significant effects on vortex shedding as well as lift and drag forces. Kim [22] found that most of the total drag force on elliptic cylinders during turbulent viscous airflow was incurred by pressure drag. Increases in pressure drag were predominantly affected by increases in thickness ratio; as the thickness ratio was increased, the amplitude of drag force oscillations, and thus the drag force, increased. Kim also found that vortex shedding behind the elliptic cylinder formed periodic and asymmetric flow patterns, which caused periodic forces normal to the direction of the free stream, lift. In the study the coefficient of lift was found to increase linearly with increases in thickness ratio. Additionally, the frequency of vortex shedding increased as the Reynolds number increased, however, the frequency was decrease when the thickness ratio decreased. While the study reported by Kim employed numerical analysis, Kwon [21] investigated flow over elliptic airfoils using wind tunnel testing. Kwon [21] measured aerodynamic forces and moments as well as the velocity field around and behind the airfoil for a single thickness ratio and Reynolds number. Figure 1.10, below, shows plots of the flow field aft of an elliptic airfoil, for smooth and tripped flow. Wind tunnel tests for smooth flow was conducted without any trip devices to cause

turbulent flow, while tripped cases used trip dots to cause turbulent flow over the airfoil. As can be seen in the plots, streamlines for tripped and un-tripped flow aft of an elliptic airfoil differ distinctly in that the vortices flow in opposite directions.

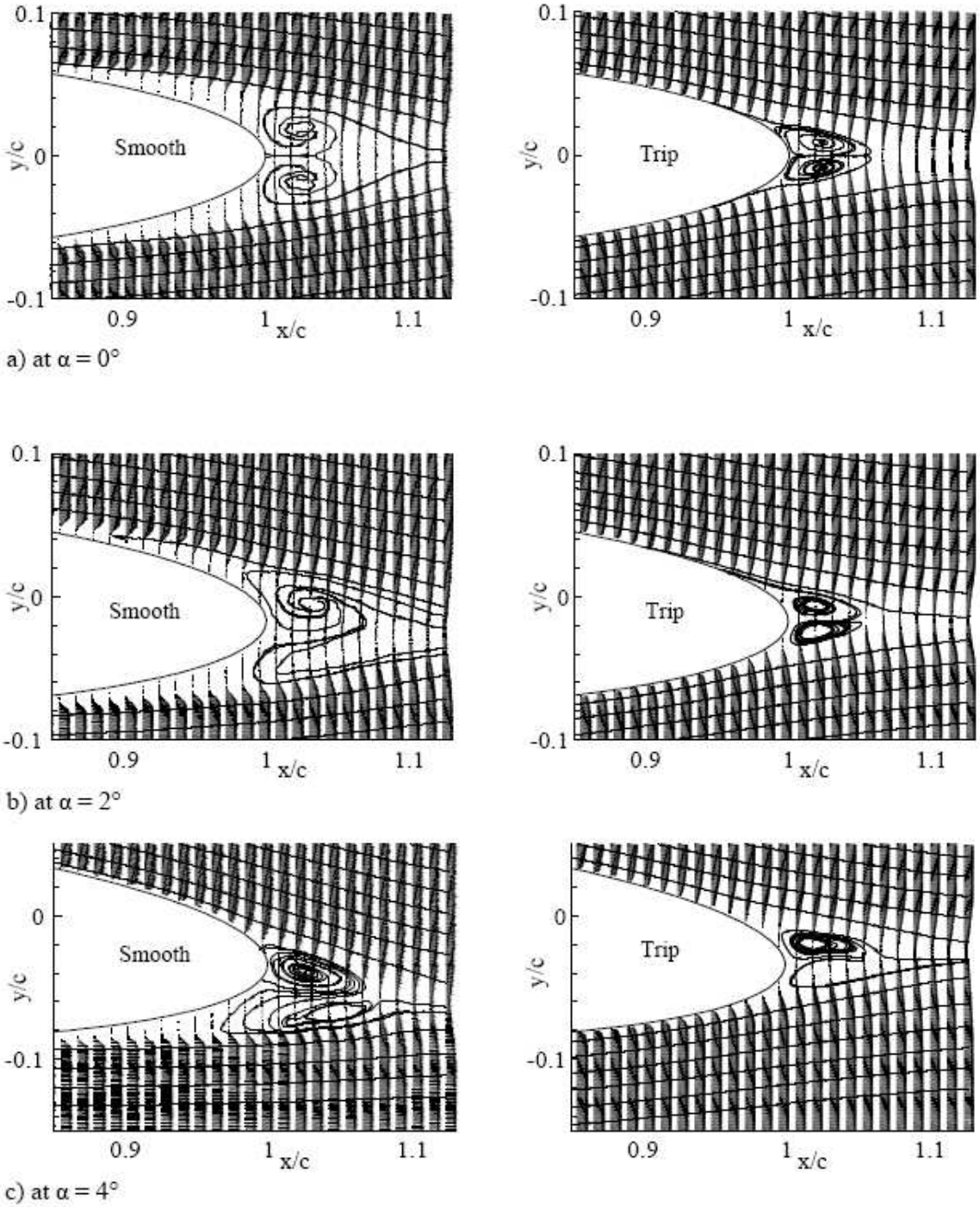

Figure 1.10 Plot of wake vortex structures taken from Reference 21

In Kwon and Park's study, the angle of attack of the elliptic airfoil was varied to investigate effects of boundary layer separation. For a smooth airfoil in a range of angles of attack between -4° to 4°, the point on the suction side where the boundary layer separated was found to move closer to the trailing edge while the point on the pressure side on which the boundary layer separated remained fixed. This caused an asymmetric flow behavior which altered the surface pressure distribution and increased the lift force in a similar manner as would a conventional flap, which caused an increase in drag coefficient. Results for tripped flow did not show this increase in drag for attack angles between -4° and 4°. Kwon found that vortex shedding aft of a thin elliptic airfoil had a significant affect on lift and drag forces; and aerodynamic characteristics of elliptic airfoils have been found to differ greatly from the characteristics of conventional airfoils. In his study, Kwon noted that an accurate judgment on the origination of wake structures could not be made using results from wind tunnel tests alone which only show velocity profiles, and Kwon went on to suggest that more further work regarding wake vortex structures could more clearly indicate laminar to turbulent boundary layer transition over elliptic airfoils.

1.3. SCOPE OF THIS STUDY

Outcome from the VTOL UAV survey and the literature study into Rotor/Wing research and development has shown that the CRW-UAV concept is a unique and innovative solution for a high-speed unmanned aircraft with vertical takeoff and landing capabilities. This concept has great potential for technological breakthroughs and much research and development is still needed. One of the most critical issues delaying fruition of a successful CRW technology demonstration is adverse effects caused by the unloaded rotor/wing during transition. These effects would be more adequately studied by gaining a more in depth understanding of aerodynamic characteristics associated with elliptic airfoils employed in rotor/wing design configurations. Greater understanding of elliptic airfoils could be obtained by utilizing CFD flow solvers to conduct detailed analysis of parameters which have significant effects on aerodynamic performance. Detailed

parametric analyses of elliptic airfoils would also aid in studying aerodynamic performance in rotary and fixed-wing flight modes. In conclusion, a parametric study into the aerodynamic performance of elliptic airfoils would benefit future research in CRW technology development and could serve as a tool for new rotor-wing design concepts.

1.3.1. The Flow Problem and Selected Parameter Range. The flow problem investigated in this study will be turbulent viscous flow over elliptic airfoils. Elliptic airfoils possess a unique characteristic, in that, the blunt trailing edge causes flow separation and vortex shedding in the flow field aft of the airfoil, even at low angles of attack, as opposed to conventional airfoils which have a sharp trailing edge. This characteristic is difficult to predict, due to its turbulent nature, and has received much interest in recent studies. Now that vast improvements have been made in the development of computational flow solving, complex numerical algorithms may be implemented on computational grids of very high point densities. These improvements allow for in depth parametric studies to be conducted for a reasonable cost and in a practical amount of time. CFD has proven to be a useful tool in aerodynamic design and analysis, even for objects which incur complex flow structures like elliptic airfoils.

This study will investigate two-dimensional flowfields surrounding elliptic airfoils for a range of parameters. These parameters include: Reynolds number (Re), angle of attack (α), and thickness ratio (t/c). Figure 1.11, below, shows a schematic of parameters investigated in this study. One objective of this study is to produce data for the parameter range investigated which may be employed in the design and development of rotor/wing unmanned aerial vehicles.

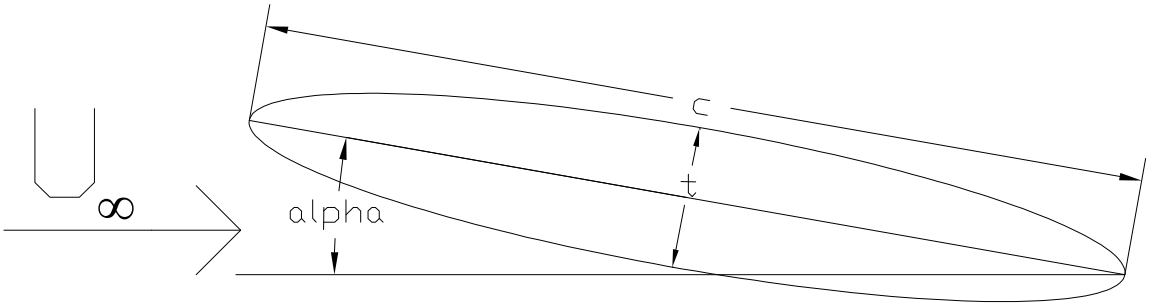

Figure 1.11 Schematic of flow configuration (not to scale)

In consideration of the prospective benefits to CRW development that could be obtained from a comprehensive understanding of elliptic airfoils, the decision was made to define the scope of this study to investigate flow about airfoils with blunt leading and trailing edges. In order for this investigation to be useful as a design tool, analyses of flow field simulations for a range of airfoil designs which are varied for specified parameters must be conducted. The selected parameters should incur an identifiable effect on aerodynamic performance and should be varied for a reasonable range of rotary and fixed wing flight conditions. To accomplish this, CFD analysis will be conducted for a wide range of flow conditions, as a rotor/wing will experience high Reynolds numbers during rotary flight, low Reynolds numbers during transition, and medium-ranged Reynolds numbers during fixed-wing flight ($1*10^5$ to $8*10^6$). Also, thickness ratio will be studied parametrically for thin airfoils (5% to 25%) for angles of attack varying from 0° to 20°. This will allow the study to investigate the effects of vortex shedding aft of the airfoil on lift and drag forces. By utilizing available flow solving software to integrate force and moment coefficients, the lift and drag performance can be correlated to plots of pressure distributions, streamlines and velocity vectors. Visualizations of flow developments including flow separation, vortex separation, and vortex shedding downstream of the airfoil, as well as plots of the surface pressure on the top and bottom of the airfoil, will also be investigated

Table 1.1 – Selected Parameter Range

Parameter	**Selected Range**		
Re	$1*10^5$	to	$8*10^6$
α	0°	to	20°
t/c	5%	to	25%

1.3.2. Validation of Methodology. Initially, the methodology used to conduct the CFD analysis will be validated by comparing results for aerodynamic characteristics of a symmetrical, 16% thick elliptic airfoil at a Reynolds number of 3×10^5 to results of wind tunnel testing conducted by Kwon [21]. This comparison will show that the griding

methods, boundary conditions, and flow parameters used to conduct the analysis were accurate and will verify the CFD analysis process that will be used to conduct the subsequent parametric study.

2. COMPUTATIONAL APPROACH

2.1. FLOWFIELD SIMULATION ABOUT AN AIRFOIL

The use of computational flow solvers is vital in the design process as an inexpensive means of predicting and optimizing aerodynamic performance. Throughout the evolution of CFD technology, many numerical simulation methods have been developed and employed. Successful applications of Navier-Stokes solution methods using structured grids have helped this method to be considered one of the most accurate. One approach to the structured grid Navier-Stokes method is the overset grid. In this approach, flowfield grids generated over a surface component overlaps with other grids and communication between sets of grids is achieved through numerical integration in the overlap region [23]. The advantage of this method is that high quality local grids can be easily generated. This study will utilize available software to apply the overset grid approach for the structured grid Navier-Stokes method to analyze the aerodynamic performance of a two-dimensional wing cross-section. Analyzing the aerodynamic performance of an airfoil using CFD involves two main processes: grid generation and flow solving.

2.1.1. Flowfield Grid Generation Technique. There are many methods for generating flow field grids. Many techniques have been developed for the definition of surface geometry, extractions of surface grids, and generation of volume grids. Generated flowfield grids are required to have enough resolution in high velocity and pressure gradient areas for CFD codes to accurately converge towards a solution [24].

2.1.1.1 Surface Geometry Definition Technique. Defining a surface geometry is the first step in generating an external flowfield grid about an aerodynamic body. Defining a surface geometry with adequate resolution is a critical step in the CFD process. Most of the grid areas where high resolutions are required usually occur near surfaces with large amounts of curvature. The definition of a surface in regions where large curvature exists must be very precise so that surface grid points extracted from the geometry accurately and smoothly represent the intended features of the selected aerodynamic bodies. An elliptical airfoil is a relatively simple shape and can be

adequately rendered by almost any Computer Aided Drafting (CAD) software. However, for the sake of simplicity and in consideration of software availability, the Aerodynamic Grid and Paneling System (AGPS) developed by The Boeing Company was the selected software for the defining of surface geometry in this study. AGPS is user friendly and has extensive capabilities in surface creation/manipulation, import/export, as well as grid extraction. Figure 2.1, below, illustrates the surface geometry of an elliptic airfoil as created using AGPS. In this study, the surface was defined as a solid curve which is oriented in the y-plane. The curve begins and ends at the trailing edge with counter-clockwise parameterization.

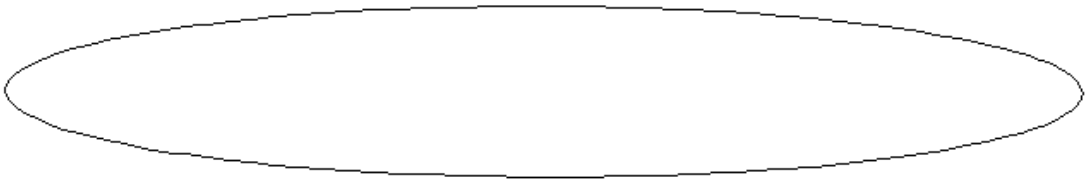

Figure 2.1 Surface Geometry of Elliptical Airfoil created in AGPS

2.1.1.2 Surface Grid Generation Technique. In order to create a surface grid, grid points must be extracted from a defined curve or surface. This task was completed easily employing AGPS. Since the surface definition was already created in AGPS, the next step was to simply use the “extract-grid” command, which can extract a grid from a curve our surface. The elliptical airfoil was defined as a three dimensional curve in the xz-plane. Using the “extract-grid” command, grid points can be established along curve in a variety of point distributions. Figure 2.2, below, compares the different point distribution methods supported in AGPS.

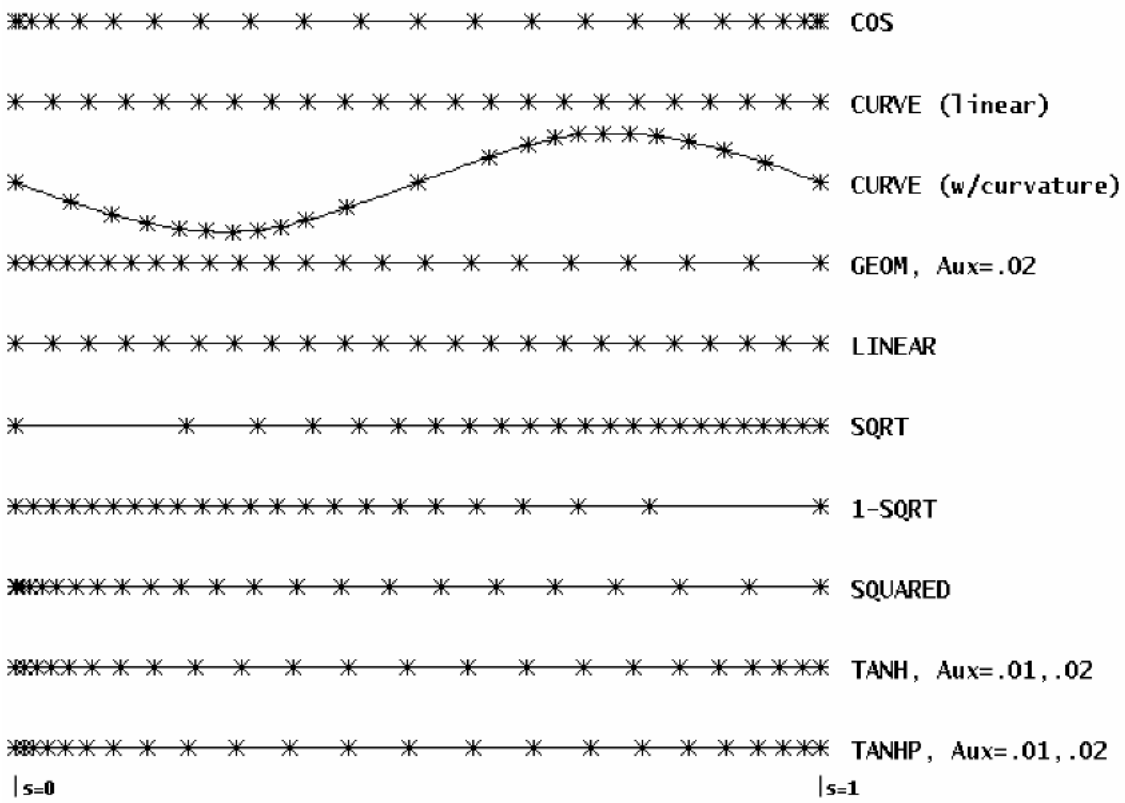

Figure 2.2 Extract-Grid Point Distribution Methods available in AGPS

As can be seen in Figure 2.2, each method provides different, useful ways to allocate point densities in different grid regions. For example, a linear point distribution spaces points evenly along a curve or surface, while the curvature integral distribution spaces points close together in regions of high curvature and farther apart in regions of low curvature. These features can be very useful because CFD codes converge more efficiently and produce better results if higher point densities are allocated in regions of high curvature and large flow gradients. Also, the more points existing in a flowfield grid, the more time and memory allocation required to execute a test case. If higher point densities can be effectively clustered in high intensity flow regions and a sparse array of points spaced over low intensity flow regions, then greater flow simulation efficiency can be achieved. Flow simulation efficiency is vitally important in a CFD analysis, especially in a parametric study, where many consecutive test cases will be executed for one grid.

In this study, the curvature integral distribution method provides a simple and effective technique for extracting points. As can be seen in Figure 2.3, using the curvature method clusters points in regions of high curvature, while using other methods do not distribute the points in a satisfactory distribution. For example, Figure 2.4 shows a similar grid extracted using the linear distribution method, while Figure 2.5 shows an additional similar grid extracted using the cosine distribution method. In the grid produced using the linear distribution method, grid points are distributed in equal intervals over areas of high curvature (high flow gradient regions) and low curvature (low flow gradient regions). This is not optimal to CFD analysis because an excessive amount of time and memory allocation will be spent on low intensity flow regions and not enough on high intensity regions. In the grid produced using the cosine distribution method, more grid points are clustered close to the trailing edge and fewer grid points are spaced over the leading edge. While this point distribution is effective at placing more points in the trailing edge where highly turbulent flow is encountered, the linear distribution method does not allocate enough points around the leading edge where a stagnation point occurs. Neither of these distribution methods is as effective at clustering points in areas of high flow intensity as the curvature point distribution method.

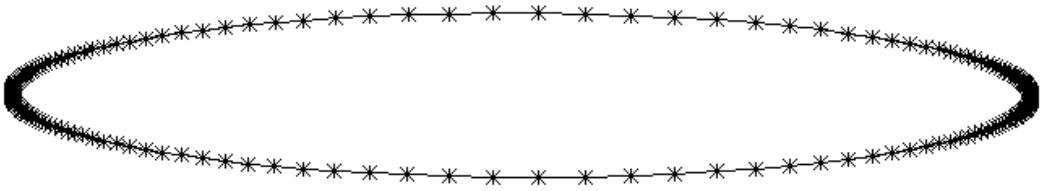

Figure 2.3 Surface Grid generated in AGPS using Curvature Point Distribution

Figure 2.4 Surface Grid generated in AGPS using Linear Point Distrubution

Figure 2.5 Surface Grid generated in AGPS using Cosine Point Distribution

2.1.1.3 Volume Grid Generation Technique. The final step in generating a flowfield grid is extending a volume grid out from points on the surface grid. There are many volume grid generation techniques that have been employed in creating two-dimensional flowfield grids. Some volume grids employ zonal methods to generate varying point densities in areas of particular interest, while other methods use continuous volume grid generation for simplicity and stability. Most volume grid generation techniques can be categorized into one of two types: structured and unstructured. Unstructured volume grids utilize non-orthogonal shaped cells which allow the technique to more easily grow out of complex geometries. This technique is commonly employed in flowfields with multiple components of complex geometries. Structured grids are more difficult to grow out of complex geometries, however, the relatively simple grid-cell geometry of structured grids allow them to require less memory allocation and converge in a more timely manner than unstructured grids. Figure 2.6, below, shows a comparison of an unstructured grid (a) and a structured grid (b).

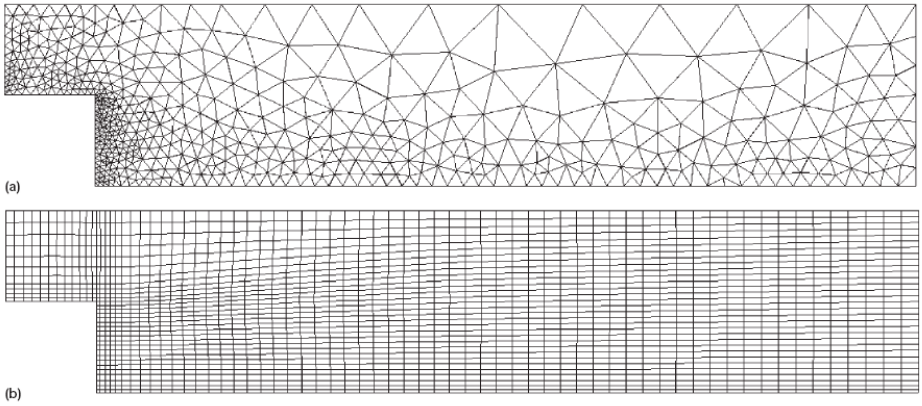

Figure 2.6 Comparison of an Unstructured Grid (a) and a Structured Grid (b)

The structured volume grid technique can be further categorized into two sub-types: orthogonal volume grids and non-orthogonal volume grids. Orthogonal volume grids consist of rectangular shaped grid-cells. Employing this technique is adequate for a simple, perpendicularly oriented, flat surface. However, this technique becomes quite difficult to grow over curved surfaces. In these instances, rectangular grid points rarely lie on the exact surface, where high point-densities are needed to effectively simulate boundary layers occurring viscous flow over a surface. Non-orthogonal volume grid techniques are needed to effectively generate a volume grid over a curved surface. Non-orthogonal volume grids can accurately enforce boundary conditions in grid regions which "grow" out from a surface grid utilizing coordinate transformations to create a boundary-fitted system. This method is much more effective for generating flowfield grids over curved surfaces and is supported by software made available by NASA.

As in the surface grid generation technique, regions, where high flow gradients are to be expected, are populated with higher point densities than regions where low flow gradients are to be expected. This task is accomplished by varying the density of grid-point layers over consecutive "L-Regions". In this study, volume grids were generated for three regions: viscous region, focus region, and outer region. The viscous region is a thin layer directly surrounding the surface which is generated with a very high grid-point density. In this region the interval spacing between the layers are constant and is the smallest interval spacing for the entire volume grid. This region clusters many grid points close to the viscid surface to accurately simulate flow gradients in the boundary layer. The focus region includes the next region outside of the viscous region. This region deals with the primary areas of interest of the grid. The inner most layer of this region has in interval spacing equal to that of the viscous region, while the interval spacing increases as field propagates outward. This allows the focus region to transition smoothly from the high point-densities of the viscous region to the low point-densities of the outer region. The outer region is the largest of the three regions and expands outward for many chord lengths away from the surface boundary. Very small amounts of change in flow are observed in the outer region, therefore, generating increasingly lower point-densities in the outer region as the grid layers approach the outermost boundary of the volume grid

allows the flowfield simulation to run more efficiently with less time and memory usage. Figure 2.7, below, shows the viscous, focus, and outer regions about an elliptic airfoil.

In this study, volume grids were generated using software created by NASA, which is available to students, called HYPGEN (Hyperbolic Grid Generator). HYPGEN expands points outward from a surface grid input. Surface grids generated by AGPS can be exported as a Plot3D file and loaded into another NASA code named OVERGRID. OVERGRID is equipped with a very user-friendly, graphical user interface (GUI), which allows the user to select the desired Plot3D file, input grid generating parameters, generate the grid, and write the generated grid to a file. The HYPGEN input parameters allow the user to designate the grid size and interval spacing of the various L-Regions as well as specifying boundary condition types. HYPGEN is equipped with a variety of available options for many different input parameters which will not be discussed in detail by this report, however, more information can be obtained from Reference 25.

HYPGEN was employed to generate the volume grids shown in Figure 2.7. The volume grid shown was expanded 10 chord lengths outward from an elliptic surface grid. Boundary condition types specified for this volume grid utilized the periodic boundary condition type for the j-parameter direction and the constant y interior and boundary slices in the k-parameter direction.

Generating a volume grid over an airfoil can be accomplished with one of two grid types: C-grid and O-grid. C-grids have designated inflow and outflow boundaries and are used as flowfield grids for airfoils with sharp trailing edges. C-grids are created by first generating a wake surface boundary slicing backward out of the trailing edge. This can be accomplished in OVERGRID using WKCUT (Wake Cut). A volume grid can be expanded outward from the airfoil and wake surface grids using HYPGEN. This method is advantageous because the forward facing grid boundary can be easily specified as the inflow boundary and the rearward facing boundary can be easily specified as the outflow boundary. However, some difficulty arises in specifying the other two boundary conditions. The boundary condition for the airfoil surface must be set as a viscid wall, while the wake surface must be specified as an inflow/outflow boundary. Figure 2.8, below, shows a C-grid generated over an airfoil surface grid with a sharp trailing edge.

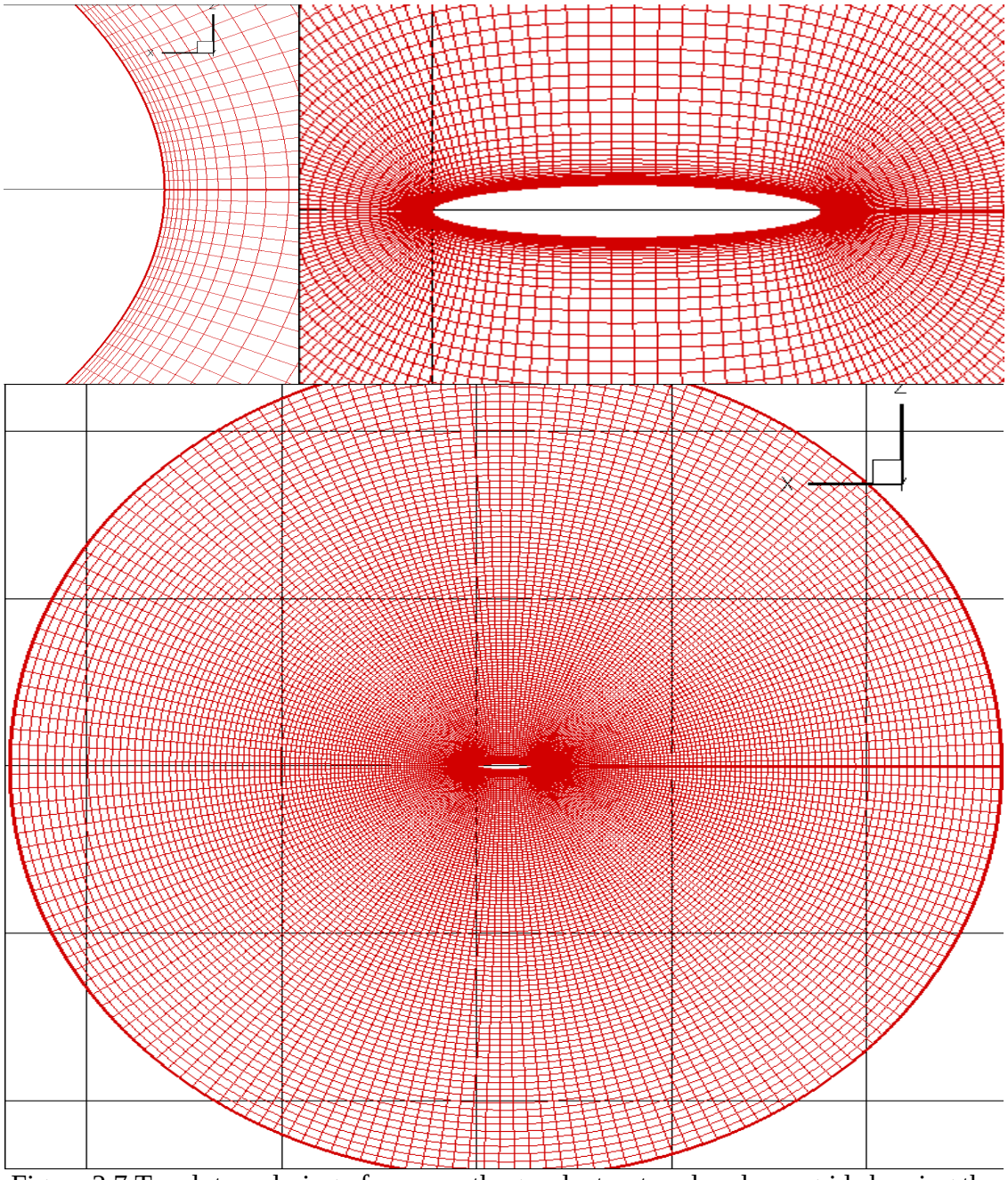

Figure 2.7 Tecplot rendering of a non-orthoganal, structured, volume grid showing the viscous region (top left), focus region (top right) and outer region (bottom)

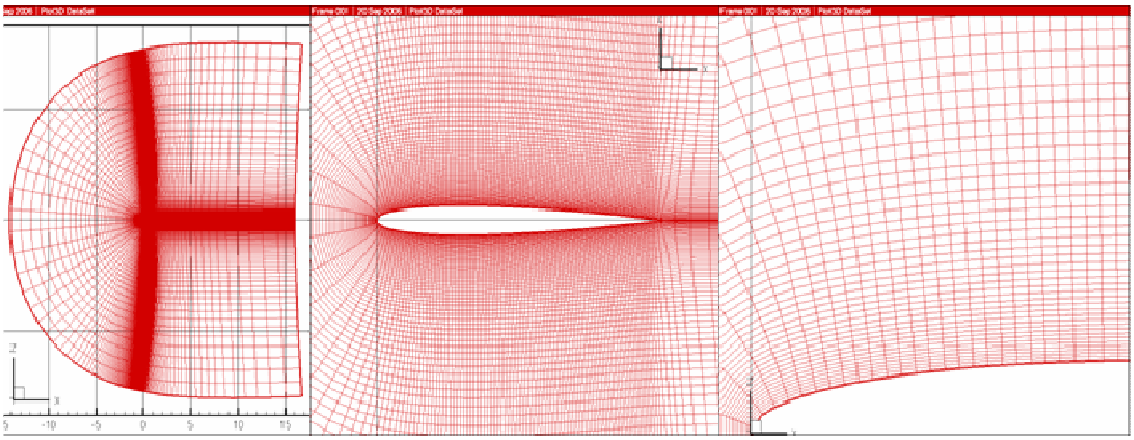

Figure 2.8 Computer Screenshots of a C-grid volume grid generated about a NACA 0009 surface grid using Hypgen showing far field, close-up, and boundary layer views

For generating a volume grid over an airfoil with a blunt trailing edge, an O-grid technique must be employed. This is because a wake surface cut can not easily be created for a blunt trailing edge. In an O-grid, layers of points are expanded out from the airfoil surface to the outer boundary. The inner airfoil surface boundary can be specified with a viscid wall boundary condition, while the outer boundary must be specified with and inflow/outflow boundary condition. Since the surface grid begins and ends at the trailing edge, a boundary exists between the inner boundary trailing edge and the outer boundary trailing edge, which must be specified with a periodic boundary condition. An example of an O-grid over an elliptic airfoil was shown, previously, in Figure 2.7.

2.1.2. Flowfield Solution Methodology. Simulating a flowfield about a structured, overset grid using Navier-Stokes governing equations involves complex flow solvers to conduct the numerical analysis methods. Application of these methods to flow problems using flow solvers is a time-consuming iterative procedure requiring significant amounts of processing power and memory usage. Developing the knowledge and skills to approach this significant of a computational undertaking can prove challenging. The following section gives a brief overview of flow solving and post-processing methodology employed in this study.

2.1.2.1 Description of Flow Solver. As previously stated, the selected flowfield solution method was the overset-structured grid, Navier-Stokes solution method. This solution method has proven to be one of the most accurate, with noteworthy potential for advanced flowfield analysis. In some cases, more simplified versions of governing flow equations or less accurate numerical methods may be implemented to generate faster results [24]. While these solution methods are sufficient to obtain basic conclusions about a particular flowfield, they may not be produce adequate results for a thorough investigation of boundary layer developments around and vortex structures aft of elliptic airfoils. For this application, a flow solver with the capability of accurately modeling low subsonic, viscous and laminar-turbulent transitional flows must be employed.

In order to meet the flow solver requirements of simulating a flowfield about an elliptic airfoil, an available flow solver which employs the overset-structured grid, Navier-Stokes solution method must be used to carry out the analysis. The selected flow solver for this application was NASA OVERFLOW. This flow solving code uses time-accurate, Reynolds-Averaged Navier Stokes (RANS) equations. OVERFLOW was originally developed to simulate the flow field about the space shuttle, and has been modified to handle low-speed conditions and conventional flight regimes. More information about OVERFLOW can be obtained from the OVERFLOW manual [26].

2.1.2.2 Flow Input Parameters. Free-stream conditions for flowfield simulations in OVERFLOW are driven by flow input parameters. These parameters include: angle of attack (α), sideslip angle (β), free-stream Mach number (M_∞), Reynolds number (Re) and static temperature (T). Angle of attack and sideslip angle specifies the flow direction. Other flow parameters including ratio of specific heats, Prandtl number, and free-stream turbulence can also be specified, however, these inputs are not necessary for low speed flows, as in this study.

2.1.2.3 Boundary Conditions. One of the most challenging and critical aspects of simulating an accurate flowfield is specification of boundary conditions. OVERFLOW is equipped with many types of boundary conditions to model different types of flow conditions. Boundary condition types for a given volume grid are specified for ranges of grid points in the OVERFLOW input deck. In order for OVERFLOW to complete a flow solving iteration, a boundary condition type must be specified for each grid point on the

boundary of the domain. Boundary condition types used in this study include: viscous adiabatic wall, free-stream/characteristic condition, periodic condition, and plane symmetry. The viscous adiabatic wall boundary condition is applied along the surface of the airfoil. The free-stream/characteristic condition is applied to the far-field boundary of the domain. The periodic condition is applied at the periodic volume grid boundary which expands out from the trailing edge of the airfoil. Plane symmetry is applied to the Y-plane boundary to allow for two-dimensional flow analysis. There are many other boundary conditions which can be applied, however, these boundary conditions have been found to work most effectively for flowfield simulation about an elliptic airfoil.

2.1.2.4 Turbulence Models. One aspect of flowfield solution methodology that has been an area of interest for research and development has been in the area of turbulence models. Turbulence models can have a significant influence over flow behavior, especially in regions of boundary layer separation and vortex shedding. Accurate prediction of flow behavior in turbulent regions has long been difficult. OVERFLOW offers five different turbulence models for predicting turbulent flow, including the Spalart-Allmaras (SA) model. This model is relatively new, and has achieved much success in accurately predicting free-shear regions. For this reason, the SA model was used in this study.

2.1.2.5 Post-Processing. The OVERFLOW flow solver outputs primitive flow parameters (density, velocity components, etc) which must be post-processed into standard flow conditions. Data can be easily extracted from OVERFLOW solution files using numerical and visual analysis. Numerical analysis can be done with simple computer programs included in the OVERFLOW package, while visual analysis must be conducted using more robust software packages [24].

2.1.2.5.1 Numerical Analysis. Many different types of quantitative investigations can be conducted for a given flowfield solution file. The primary form of numerical analysis employed in this study is investigation into pressure, force and moment coefficients. Pressure coefficients can be easily calculated from a flowfield solution file using Tecplot. Tecplot can then be utilized to plot the pressure coefficients over the top and bottom surfaces of the airfoil. These plots can be very useful in analyzing and comparing the pressure distributions occurring along the surface of an airfoil for varying

flow parameters. Force and moment coefficients for a flowfield solution may be obtained using software included in the OVERLOW package called FOMOCO. This software integrates the force and moment coefficients over an airfoil. Data obtained from FOMOCO can then be organized into charts and tables using Excel. A combination of results extracted using Tecplot and FOMOCO can provide an effective comparison of flow parameter ranges and can aid in gaining a satisfactory understanding of airfoil performance.

2.1.2.5.2 Visual Analysis. Visual analysis is essential to gaining an understanding of boundary layer separation and trailing edge vortex structures. Using visual analysis, one can transform quantitative data into a physical representation of the flowfield. This fact bestows added value to the flowfiled analysis by allowing an analyst to easily envision flow features occurring in particular areas of interest. The three main plotting techniques employed in this study include: contour plots, streamline plots, and velocity vector plots. Contour plots can be used to illustrate gradients of flowfield solution data using color scaling techniques. Streamline plots allow an analyst to see the development of streamlines and vortices occurring about and aft of an airfoil. Similarly, velocity vector plots are employed to show velocity profiles occurring in the boundary layer as well as boundary layer separation and vortex structure. Each of these techniques is available in Tecplot graphing package, for further information on Tecplot see Reference [27].

3. VALIDATION OF METHODOLOGY

In order to ensure the accurate computational results, an extensive validation of methodology test case was conducted. When using CFD analysis, it is easy to make unexpected mistakes which can significantly alter the flowfield solutions. By comparing results produced from CFD analysis with wind tunnel test results, an analyst can validate their processes and methodology. Validation test cases were completed for specified input parameters based on experimental wind tunnel test data found in Reference 21.

3.1. VALIDATION TEST CASE PROCEDURES

The purpose of a validation test case was to verify that the flowfield solution results obtained from CFD analysis compared similarly to experimental data. This validation test case compared flowfield solution results for specified flow input parameters to experimental wind tunnel test data found in a previous study. The intent of the validation cases was not to authenticate the flow solving software, but merely to provide confidence in the accuracy of procedures and methodology which were employed in the parametric study.

3.1.1. Validation Test Case Grid Generation. In order to conduct the validation test case a volume grid was generated employing the methodology outlined in the previous section. The first step was to create a surface definition of the elliptic airfoil. Airfoil surface definition was based upon the 16% thickness elliptic airfoil studied by Kwon [21]. The surface definition was created using AGPS. This consisted of a two-dimensional ellipse, oriented in the XZ-plane, which had a chord length of one unit in the positive X-axis and a maximum thickness of 0.16 units in the Z-axis located at one-half of the chord length along the X-axis. The surface definition for the 16% thick elliptic airfoil has been placed in Appendix A. From this surface definition, a surface grid of 250 points was extracted using curvature point distribution in AGPS, as seen in Figure 3.1, below. This point distribution was used so that many points would be clustered in areas of large curvature, where the largest flow gradients will typically exist.

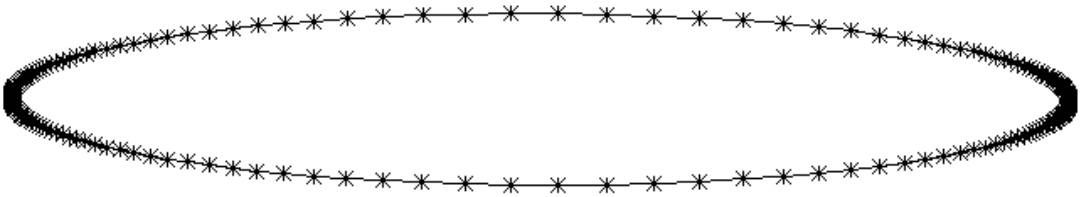

Figure 3.1 Surface grid generated in AGPS with 250 points in curvature point distribution

This generated surface grid was exported from AGPS as an array of three surface grids, all oriented in the XZ-plane with one the main grid located at Y = 0, and two identical side grids translated a unit length apart from the main grid, one in the positive Y-direction and the other in the negative Y-direction. The entire array was exported in the Plot-3D ASCII format required for import into the Chimera Grid Tools (CGT) package. Once the Plot-3D file was read into CGT, a volume grid was generated utilizing HYPGEN. The volume grid was expanded out from the surface grid using the methodology outlined in the second chapter. The boundary condition used to grow the volume grid included periodic boundaries at the minimum and maximum J-parameter, both of which were located at the trailing edge of the airfoil surface. Constant Y interior and boundary slices were specified for the minimum and maximum K-parameter. This specified the volume grid as a two-dimensional grid in the Y-plane.

Three L-regions were used to grow the volume grid outward from the surface boundary. The first L-region specified a highly dense point density close to the boundary surface. This region consisted of three point layers each spaced 0.0001 chord lengths apart. The second L-region consisted of 200 point layers expanding outward 0.5 chord lengths. This region clustered large point densities in the primary areas of interest close to the surface of the airfoil. The third L-Region expanded out into the far field flow region surrounding the airfoil. The region spaced 100 point layers 14.5 chord lengths in all directions into the free stream, creating a total of 303 point layers expanding 15 chord lengths outward from the surface of the airfoil.

3.1.2. **Flow Solver Input Parameters.** Flow solver input parameters are specified for OVERFLOW using an input deck, which consists of over 120 separate input parameters. The scope of this study involves a small portion of the potential input

parameters, so many of the default settings will be retained. The input deck will be used, primarily, to specify the freestream flow conditions: Reynolds number (Re), Mach number (M_∞) , and angle of attack (α).

3.2. RESULTS OF CFD ANALYSIS FOR A 16% ELLIPTIC AIRFOIL

For the validation test case, CFD analysis was conducted on a 16% thick elliptical airfoil for a Reynolds number of $3.0*10^5$ and a free stream velocity of 25 m/s. Flow fields were simulated for a range of attack angles between -4 and 8 degrees at 2 degree intervals. The following figures show contour plots with streamlines showing vortex development aft of an elliptical airfoil at an attack angle of 0 degrees. As can be seen in the figures, flow separation occurs over the blunt trailing edge, creating two opposing vortices aft of the airfoil.

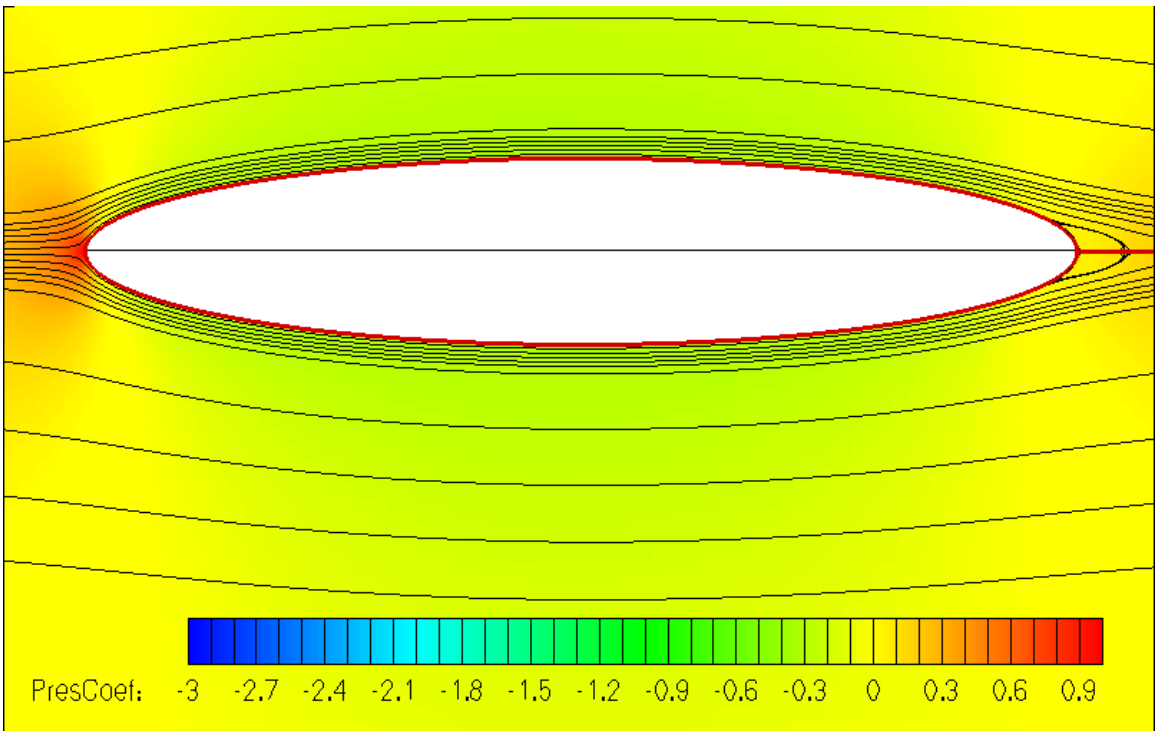

Figure 3.2 – Plot of flow development over an elliptic airfoil showing pressure distribution and streamlines.
Re = $3*10^5$, t/c = 16%, α = 0°

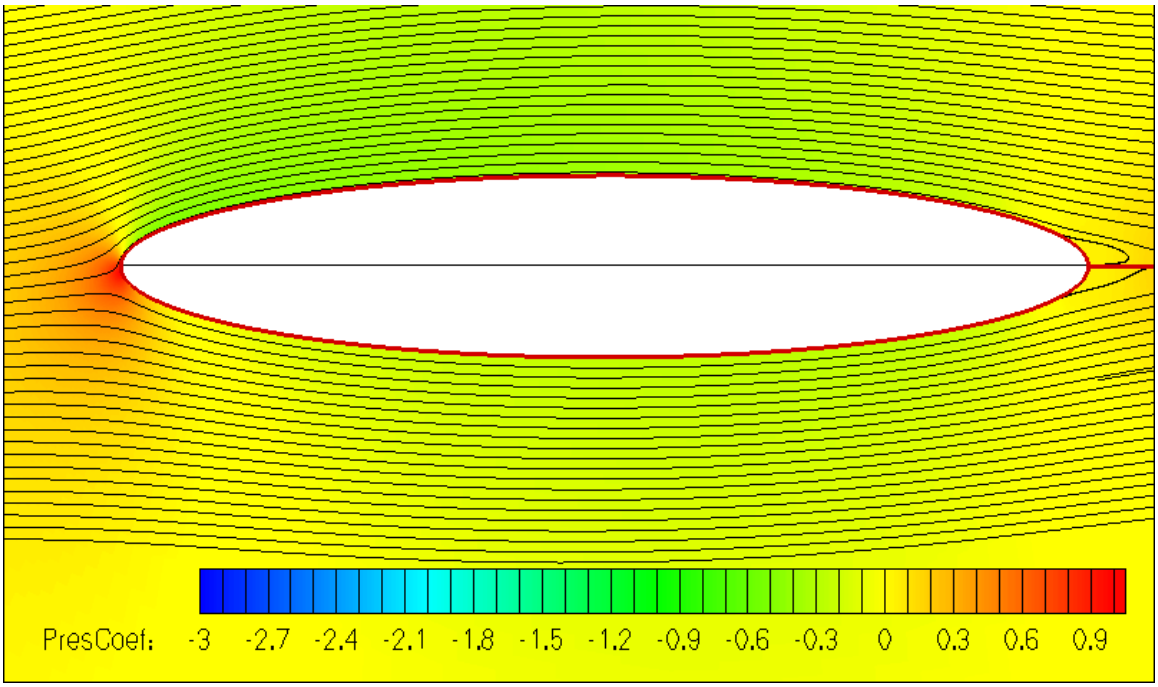

Figure 3.3 - Plot of flow development over an elliptic airfoil showing pressure distribution and streamlines.
Re = $3*10^5$, t/c = 16%, α = 2°

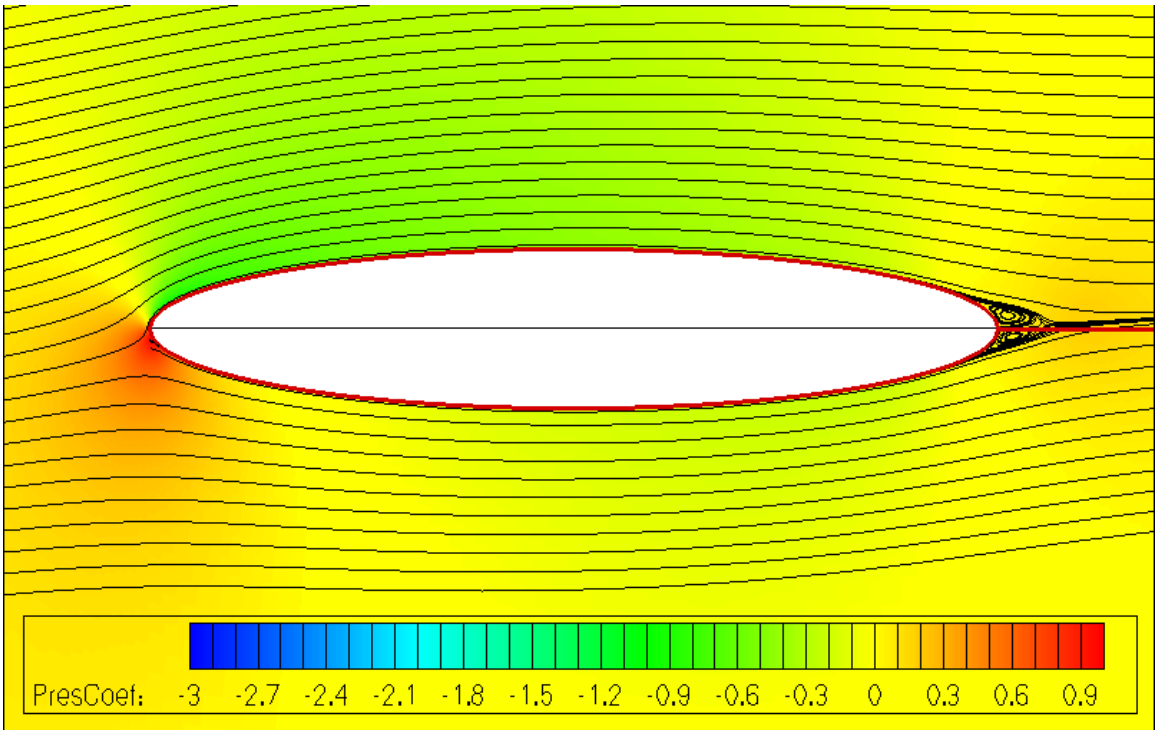

Figure 3.4 - Plot of flow development over an elliptic airfoil showing pressure distribution and streamlines.
Re = $3*10^5$, t/c = 16%, α = 4°

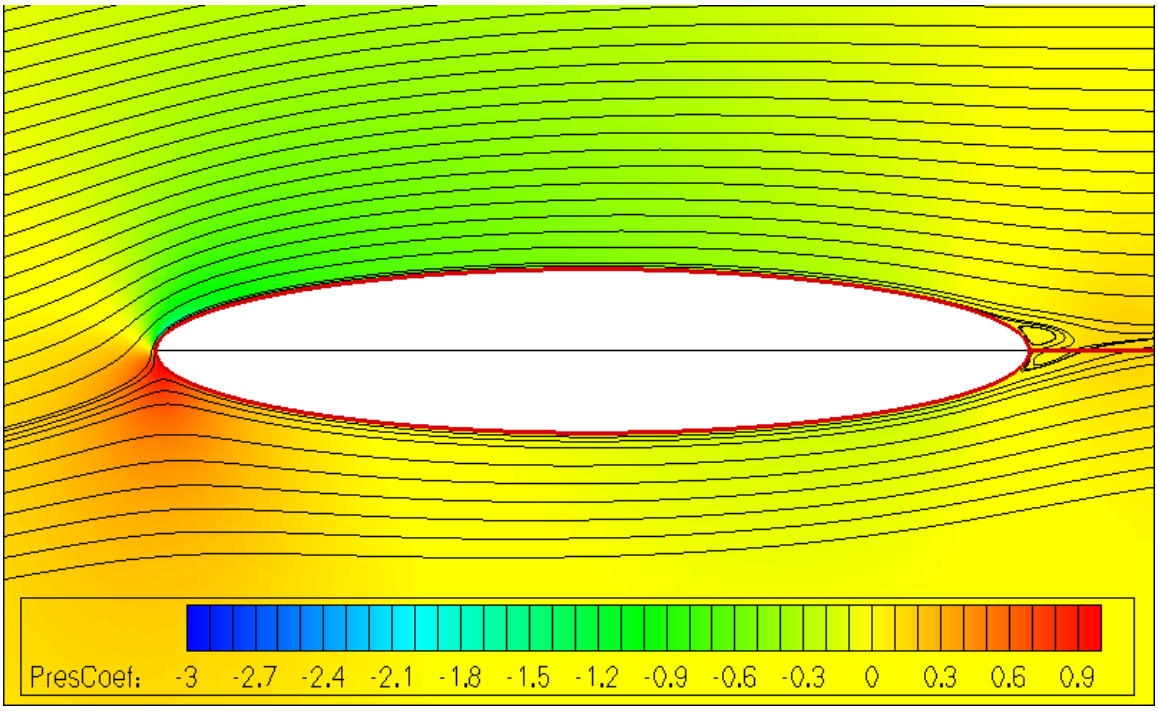

Figure 3.5 - Plot of flow development over an elliptic airfoil showing pressure distribution and streamlines.
Re = $3*10^5$, t/c = 16%, α = 6°

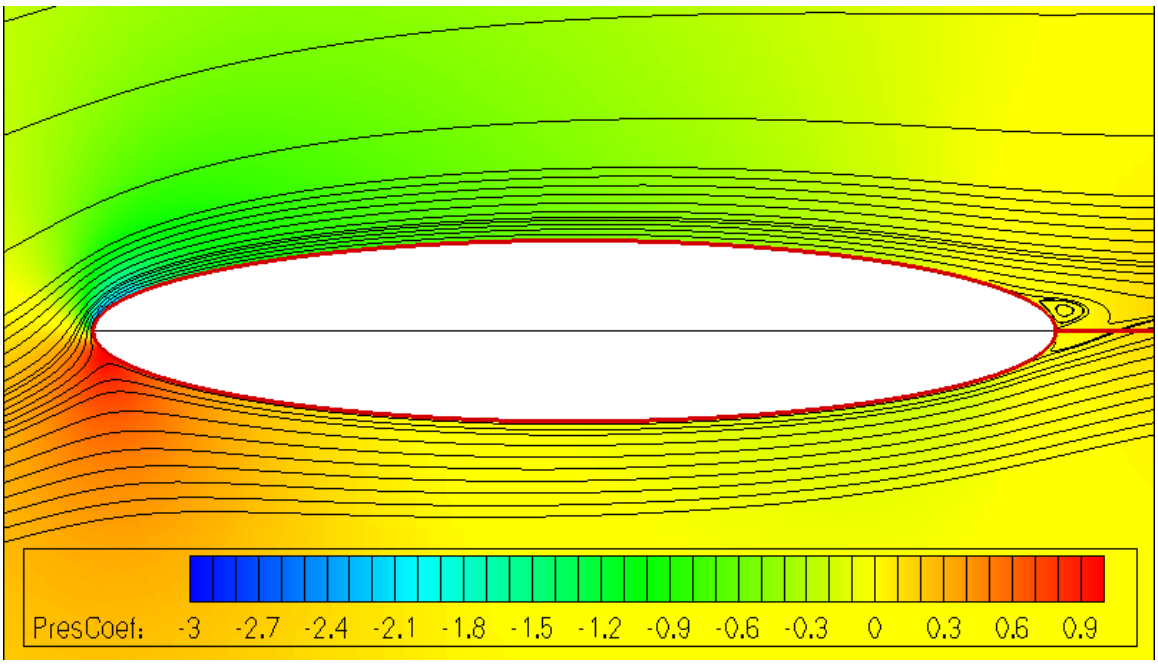

Figure 3.6 - Plot of flow development over an elliptic airfoil showing pressure distribution and streamlines.
Re = $3*10^5$, t/c = 16%, α = 8°

At α=0°, flow was observed to be symmetrical, as shown in Figure 3.2. At α=2° the aft vortices are shifted upwards, causing the upper vortex to be larger than the lower vortex. As can be seen in Figures 3.3 and 3.4, flow over the top of the airfoil flowed over and around the upper vortex and was pulled back towards the airfoil trailing edge by both vortices. When the flow hit the trailing edge, it then flowed either upward along the trailing edge into the upper vortex or downward along the bottom side of the airfoil and into the lower vortex. At higher angles of attack, flow velocity over the top of the airfoil increased, causing more flow around the upper vortex and in between the two aft vortices, as can be seen in Figures 3.5 and 3.6. The increase in flow between the aft vortices caused the lower vortex to shift backwards, away from the trailing edge, and also decreased the cross-sectional area of the lower vortex. This occurrence can be visualized more clearly in Figures 3.7 through 3.11, which show vortex development aft of the blunt trailing edge for a 16% thick elliptic airfoil.

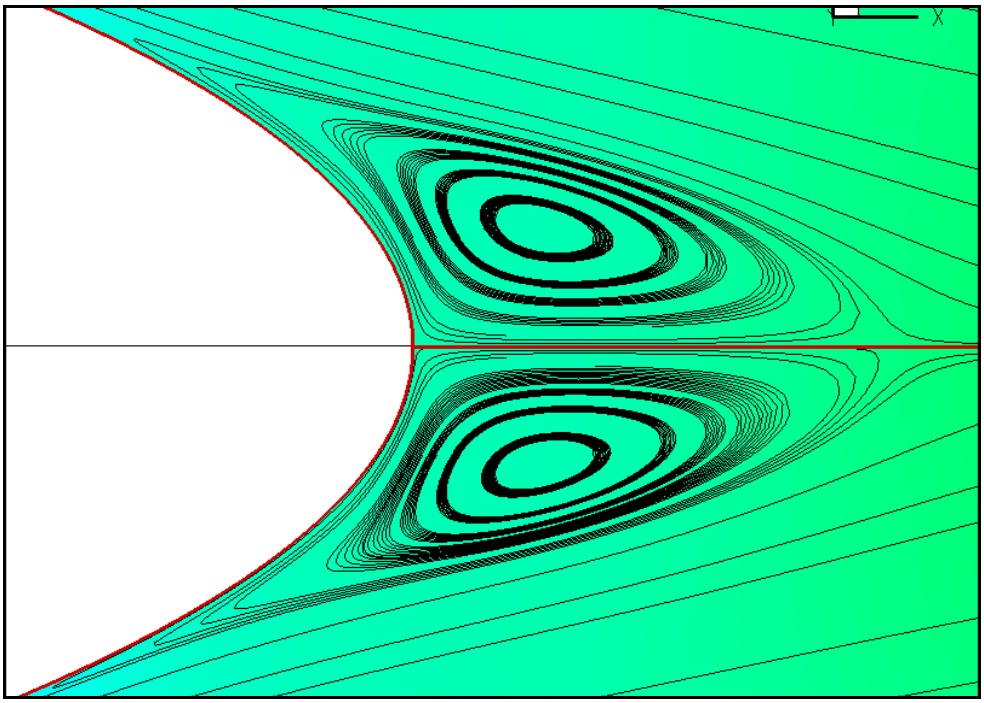

Figure 3.7 - Plot of vortex development downstream of an elliptic airfoil showing pressure distribution and streamlines.
$Re = 3*10^5$, t/c = 16%, α = 0°

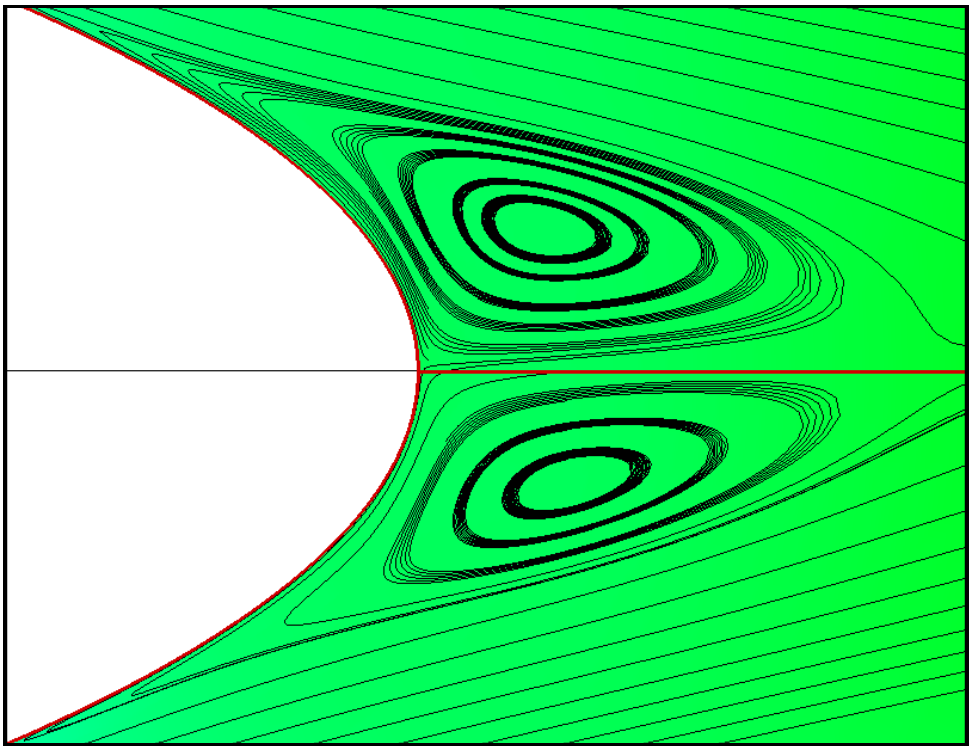

Figure 3.8 Contour - Plot of vortex development downstream of an elliptic airfoil showing pressure distribution and streamlines.
Re = $3*10^5$, t/c = 16%, α = 2°

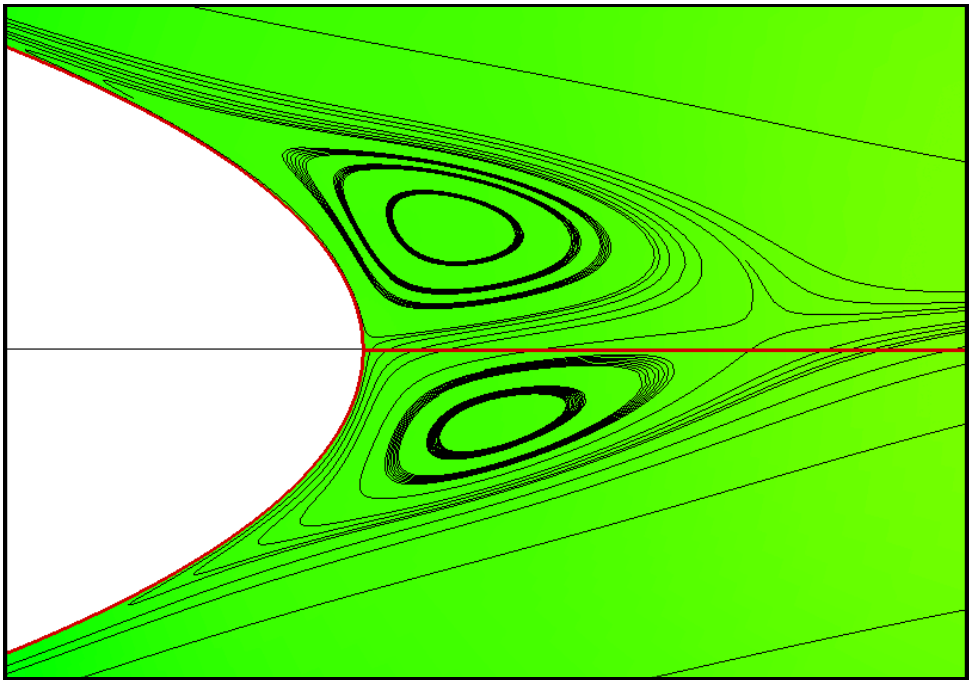

Figure 3.9 - Plot of vortex development downstream of an elliptic airfoil showing pressure distribution and streamlines.
Re = $3*10^5$, t/c = 16%, α=4°

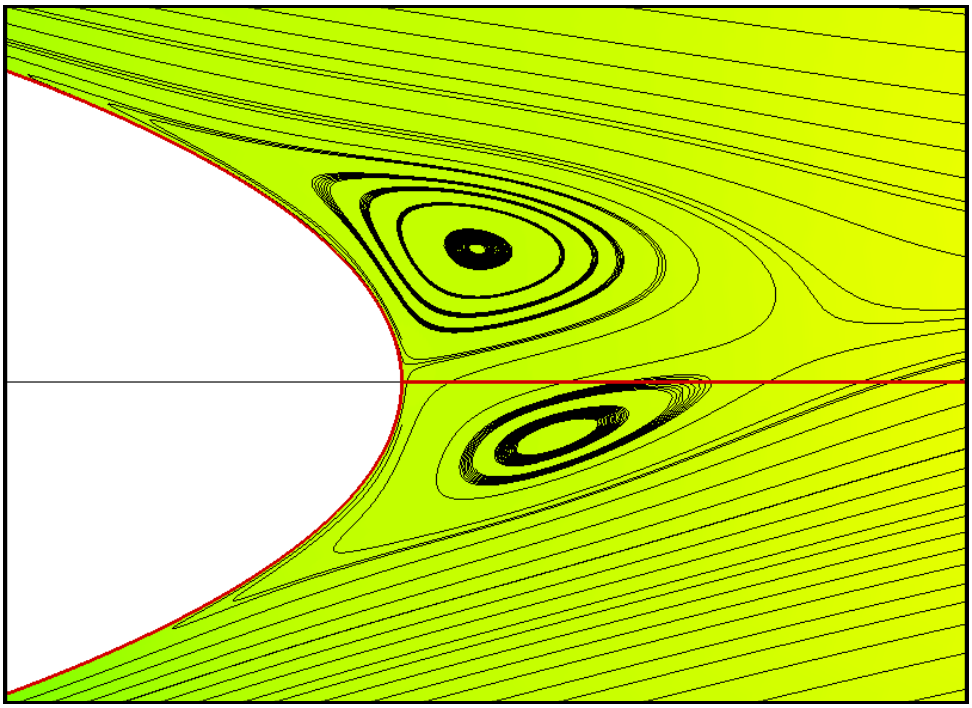

Figure 3.10 - Plot of vortex development downstream of an elliptic airfoil showing pressure distribution and streamlines.
Re = $3*10^5$, t/c = 16%, α=6°

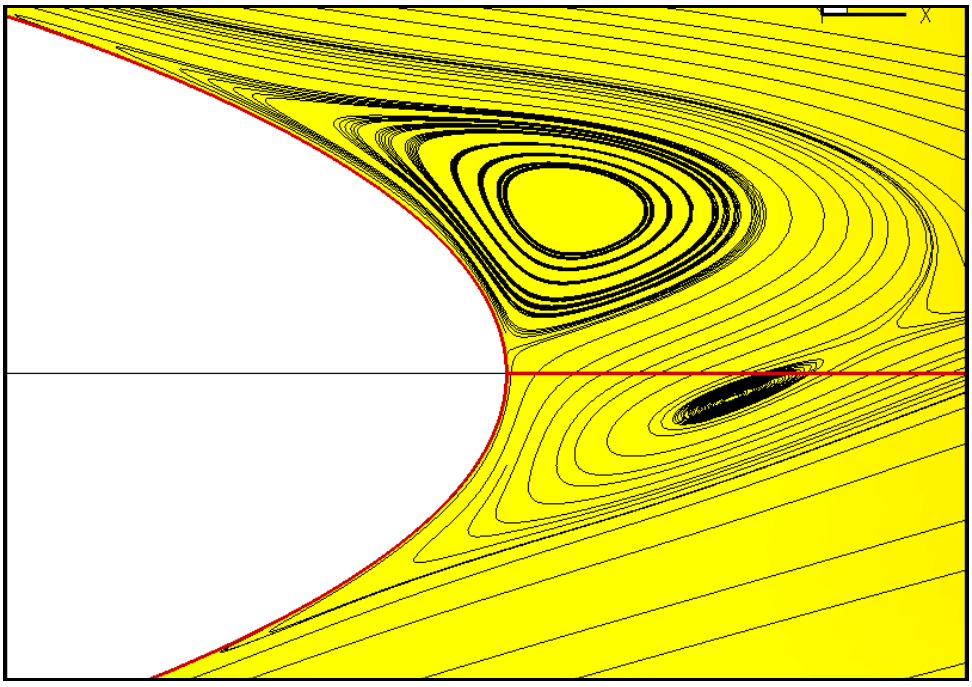

Figure 3.11 - Plot of vortex development downstream of an elliptic airfoil showing pressure distribution and streamlines.
Re = $3*10^5$, t/c = 16%, α=8°

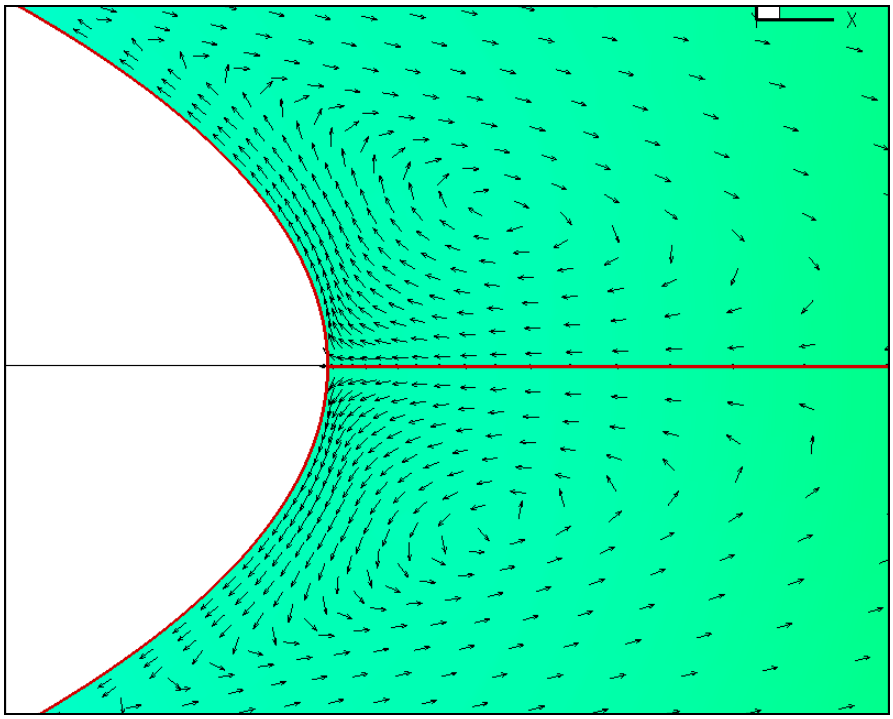

Figure 3.12 - Plot of normalized velocity vectors in the separated flow region of an elliptic airfoil.
Re = $3*10^5$, t/c = 16%, α =0°

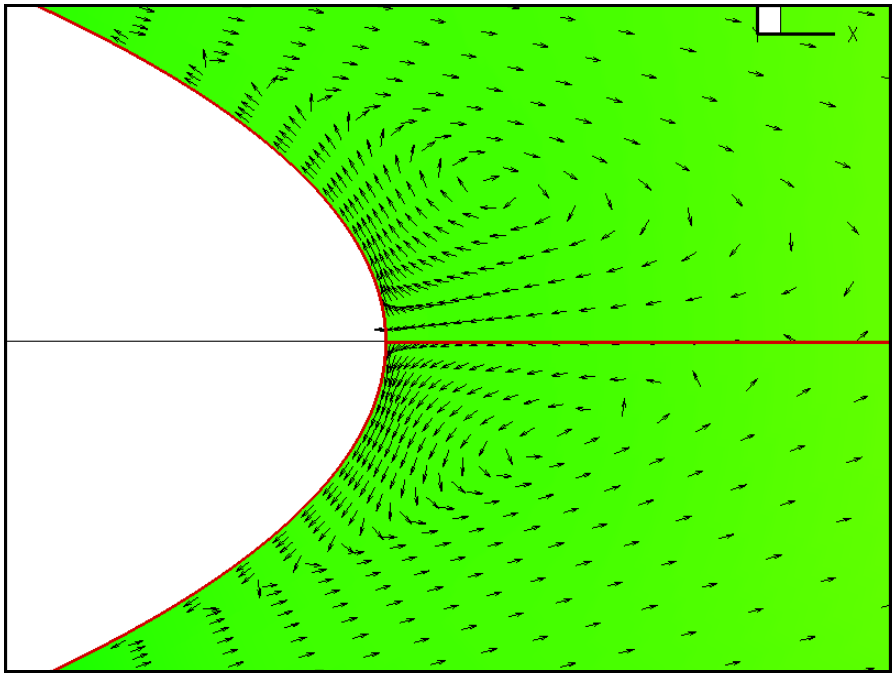

Figure 3.13 - Plot of normalized velocity vectors in the separated flow region of an elliptic airfoil.
Re = $3*10^5$, t/c = 16%, α =2°

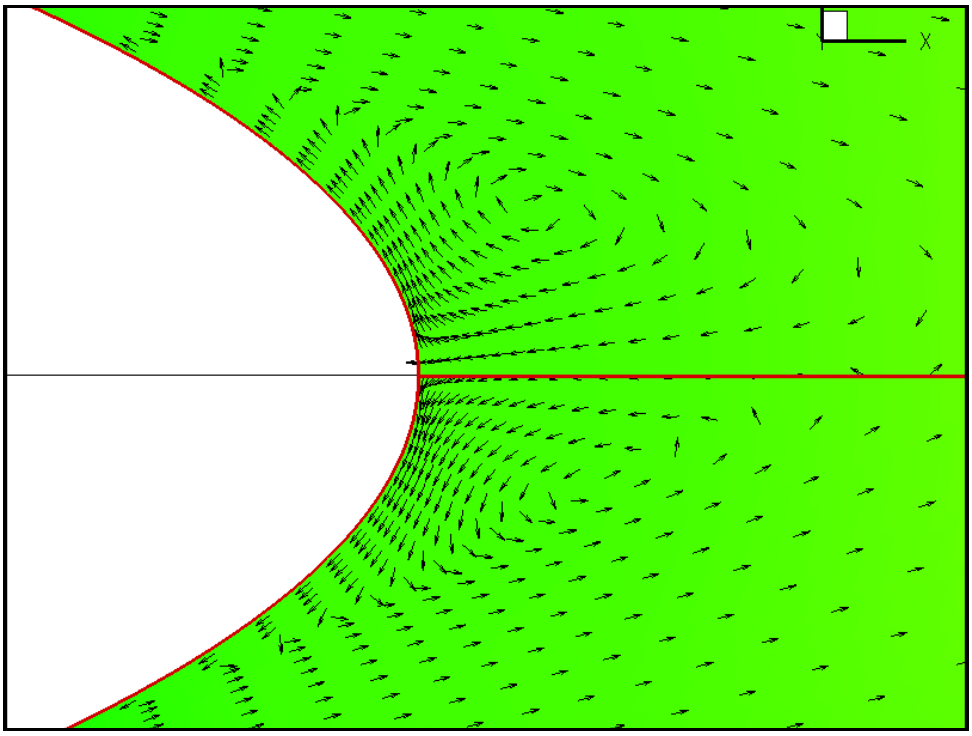

Figure 3.14 - Plot of normalized velocity vectors in the separated flow region of an elliptic airfoil.
Re = $3*10^5$, t/c = 16%, α =4°

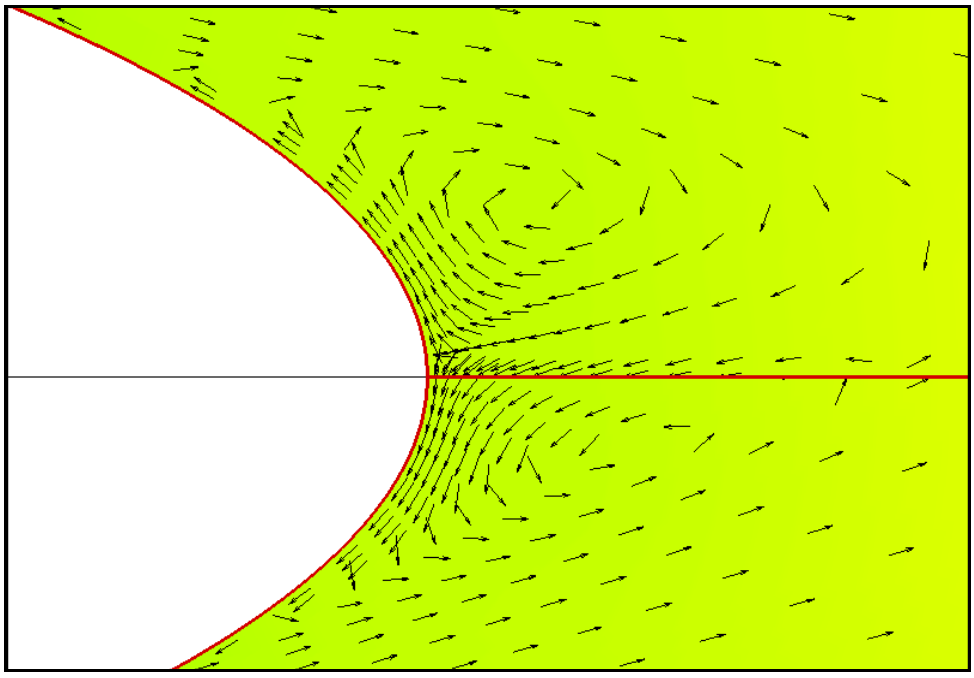

Figure 3.15 - Plot of normalized velocity vectors in the separated flow region of an elliptic airfoil.
Re = $3*10^5$, t/c = 16%, α =6°

At α=8°, the cross-sectional area of the lower vortex had diminished significantly. The vortex had shifted backwards to the point of being almost aft of the upper vortex, which caused more of the flow over the bottom surface of the airfoil to remain attached. As can be seen in Figures 3.15 and 3.16, the stagnation point moved down to the lower side of the airfoil leading edge.

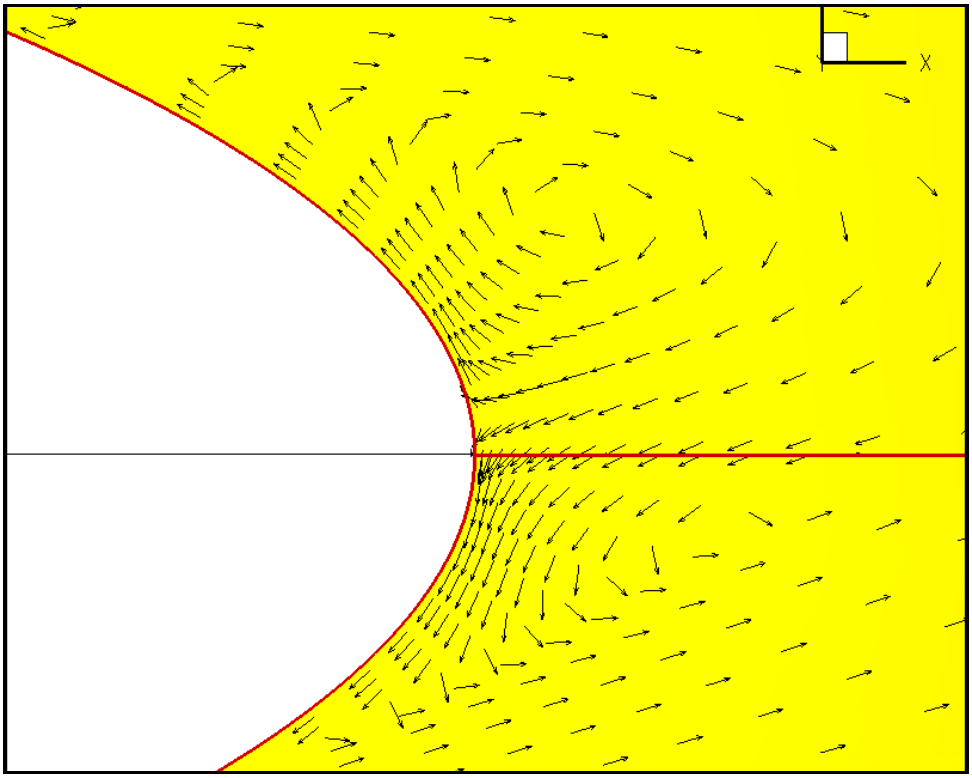

Figure 3.16 - Plot of normalized velocity vectors in the separated flow region of an elliptic airfoil..
Re = $3*10^5$, t/c = 16%, α=8°

For attack angles greater than 6°, variations in the distribution of surface pressure over the top and bottom surfaces of the airfoil began to become interesting. Flow over the top surface increased greatly over the first quarter of the surface causing a considerably lower pressure distribution in that region. The pressure increased over the top surface as flow approached the blunt trailing edge. Another interesting observation was the increase in flow velocity over the back half of the bottom surface of the airfoil, which caused a

decrease in surface pressure. The following figures show surface distribution plots for 16% thick elliptic airfoils at a Reynolds number of $3*10^5$ for attack angles of 0°, 2°, 4°, 6°, and 8°.

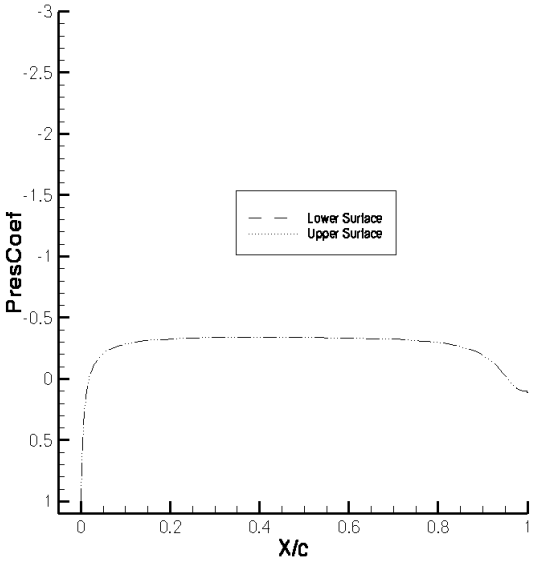

Figure 3.17 – Plot of surface pressure distribution around an elliptic airfoil.
Re = $3*10^5$, t/c = 16%, α = 0°

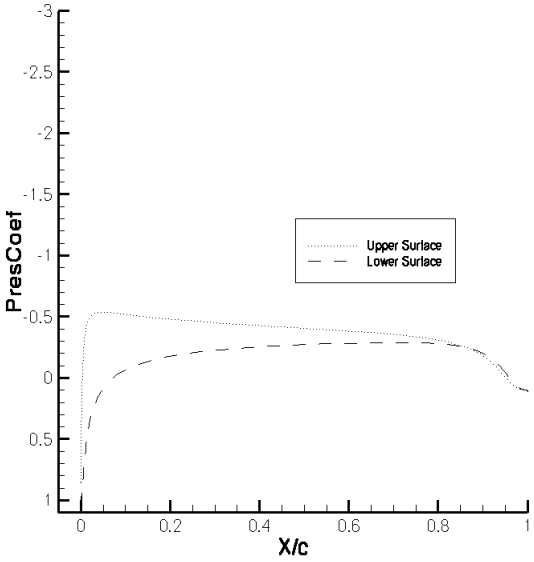

Figure 3.18 – Plot of surface pressure distribution around an elliptic airfoil.
Re = $3*10^5$, t/c = 16%, α = 2°

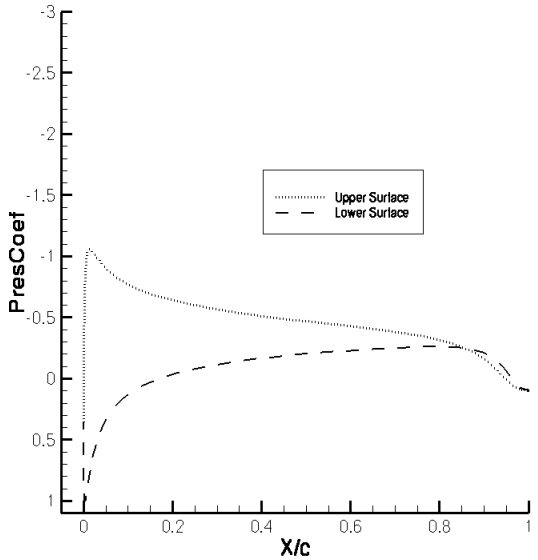

Figure 3.19 – Plot of surface pressure distribution around an elliptic airfoil.
Re = $3*10^5$, t/c = 16%, α = 4°

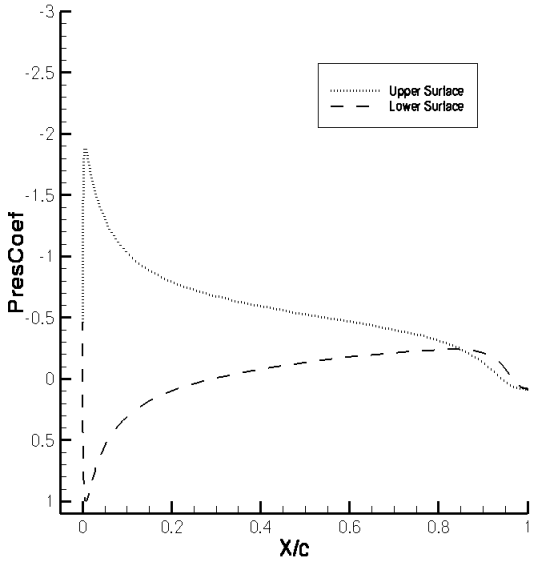

Figure 3.20 – Plot of surface pressure distribution around an elliptic airfoil.
Re = $3*10^5$, t/c = 16%, α = 6°

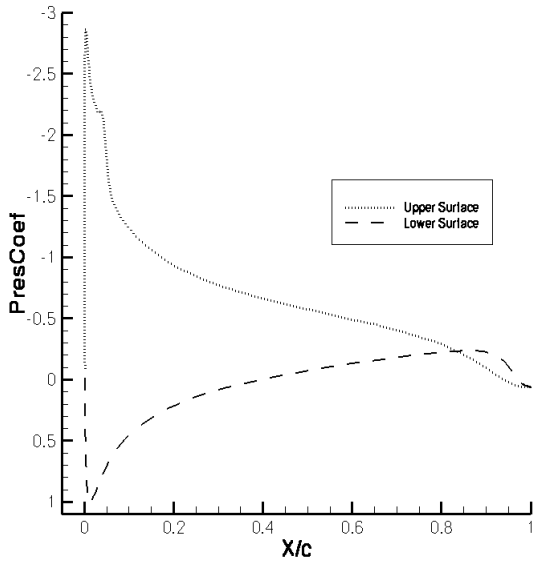

Figure 3.21 – Plot of surface pressure distribution around an elliptic airfoil. Re = $3*10^5$, t/c = 16%, α = 8°

As can be seen in Figure 3.17, the surface pressure distribution over the top and bottom sides of the airfoil were the same for α=0°. For attack angles greater than 0°, the surface pressure over the top surface was lower than the bottom surface for most of the chord length. However, for the last 5-10% of the chord length, the surface pressure over the top of the airfoil was greater than that of the bottom surface. As the angle of attack was increased, the surface pressure over the first half of the top surface dropped considerably, as can be observed in Figures 3.18 and 3.19. Surface pressure distribution on the bottom side of the airfoil trended nearly the same at each angle of attack, while the pressure distribution on the top side changed drastically, as seen in Figure 3.20. At α=8°, an interesting observation was noticed towards the leading edge of the top surface. The surface pressure in the first 10% of the chord was found to be relatively turbulent, as seen in Figure 3.21. Upon further investigation of the flowfield simulation, a laminar separation bubble (LSB) was observed in the turbulent surface pressure distribution region. The existence of an LSB in this region would explain the surface pressure distribution observed for α=8°.

3.2.1. Note on Laminar Separation Bubble. Laminar Separation Bubbles (LSB) are one of the most dominant flow formations observed in analysis of airfoils at low Reynolds numbers. Occurrence of a LSB is instigated when oncoming flow encounters an adverse pressure gradient in the boundary layer, producing a laminar shear layer. As the oncoming flow travels downstream, flow transitions to laminar to turbulent. This transition energizes the flow, causing reattachment to the airfoil surface. This was observed in CFD analysis for a 16% thick elliptic airfoil at $\alpha = 8°$, and $Re = 3 * 10^5$, as shown in Figure 3.22.

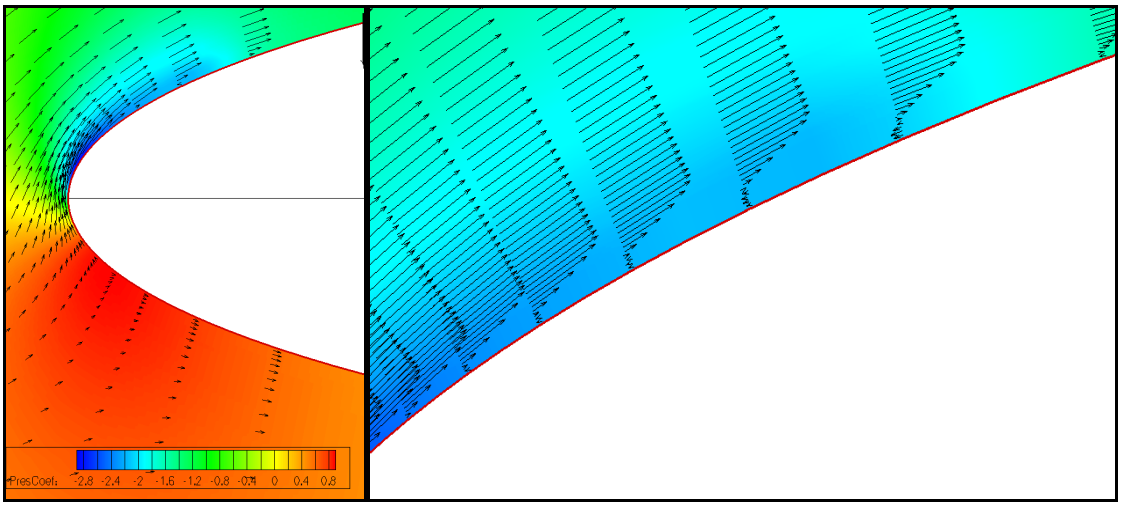

Figure 3.22 Close-up of boundary layer velocity profiles within a laminar separation bubble developed near the airfoil trailing edge.
$Re = 3*10^5$, t/c = 16%, $\alpha = 8°$

3.3. EXPERIMENTAL DATA FOR A 16% THICK ELLIPTIC AIRFOIL

Experimental data for a 16% elliptic airfoil at a Reynolds number of $3*10^5$ was obtained from Kwon [21]. In Kwon's study, lift and pitching moments were determined using surface pressure distributions and the drag coefficients were calculated employing wake velocity profiles. The following figures show plots wake vortex structure data obtained from wind tunnel testing using particle image velocimetry (PIV). In the "trip" test cases, boundary layer transition trip was used to understand the effects of flow separation on aerodynamic characteristics. For this, circular trip dots made of Vinyl tape were used [21]. Figures 3.23 through 3.27 show time averaged velocity vectors with streamlines aft of the airfoil for $\alpha = 0°$, 2°, 4°, 6°, and 8°.

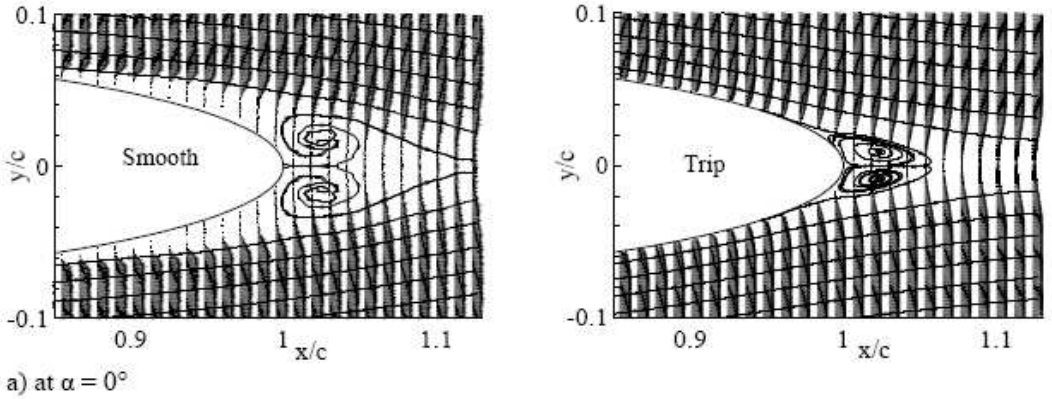

a) at α = 0°

Figure 3.23 Wake vortex structure with streamlines [Obtained from Reference 21]

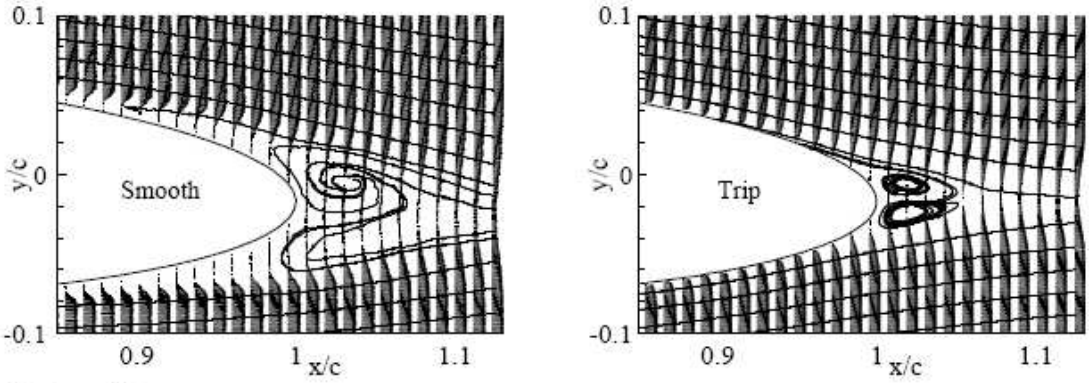

b) at α = 2°

Figure 3.24 Wake vortex structure with streamlines [Obtained from Reference 21]

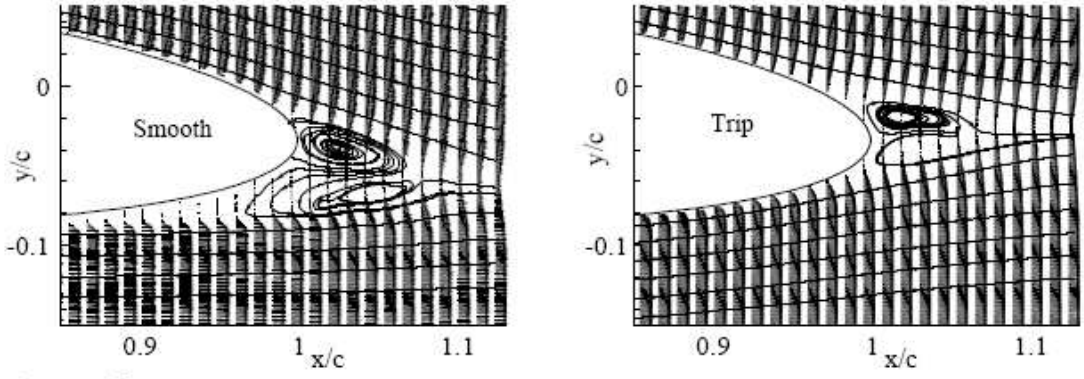

c) at α = 4°

Figure 3.25 Wake vortex structure with streamlines [Obtained from Reference 21]

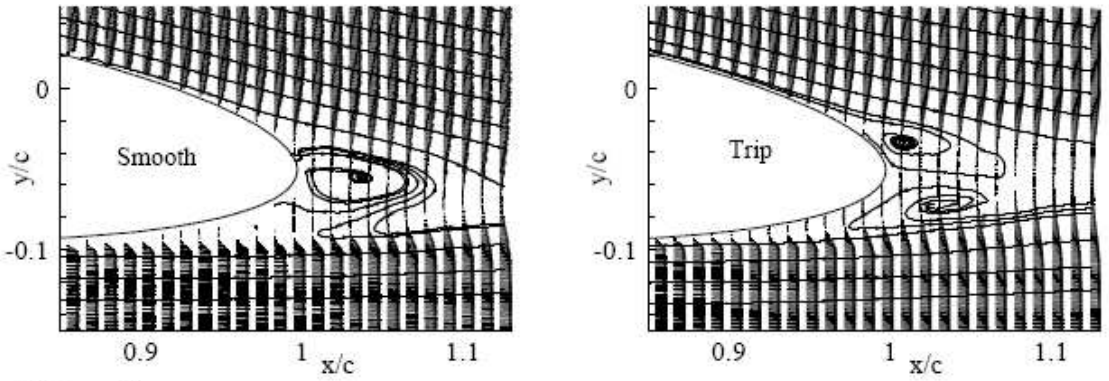

d) at α = 6°

Figure 3.26 Wake vortex structure with streamlines [Obtained from Reference 21]

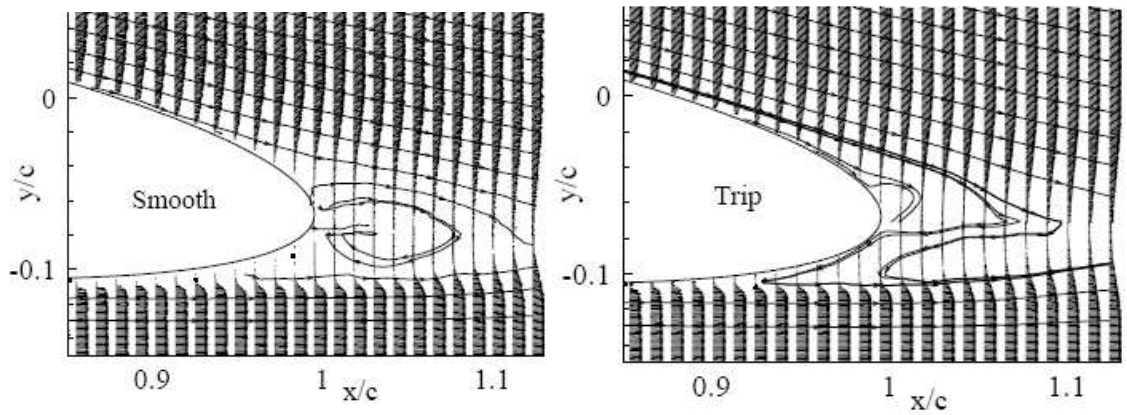

(e) at α = 8°

Figure 3.27 Wake vortex structure with streamlines [Obtained from Reference 21]

At α = 0°, flow for smooth and tripped flow separates into two symmetrical vortices, as seen in Figure 3.20. For higher angles of attack, aft vortices are not symmetrical. The vortex flow structures shown in the above figures for tripped flow compare similarly to the flow structures observed in the CFD Analysis. Kwon and Park [21] also studied surface pressure distributions. Figure 3.25, below, shows the surface pressure distributions for smooth and tripped cases at α = 0°, 2°, 4°, 6°, and 8°. At attack angles less than 6°, the tripped cases compare similarly to the surface pressure distributions observed in the CFD analysis.

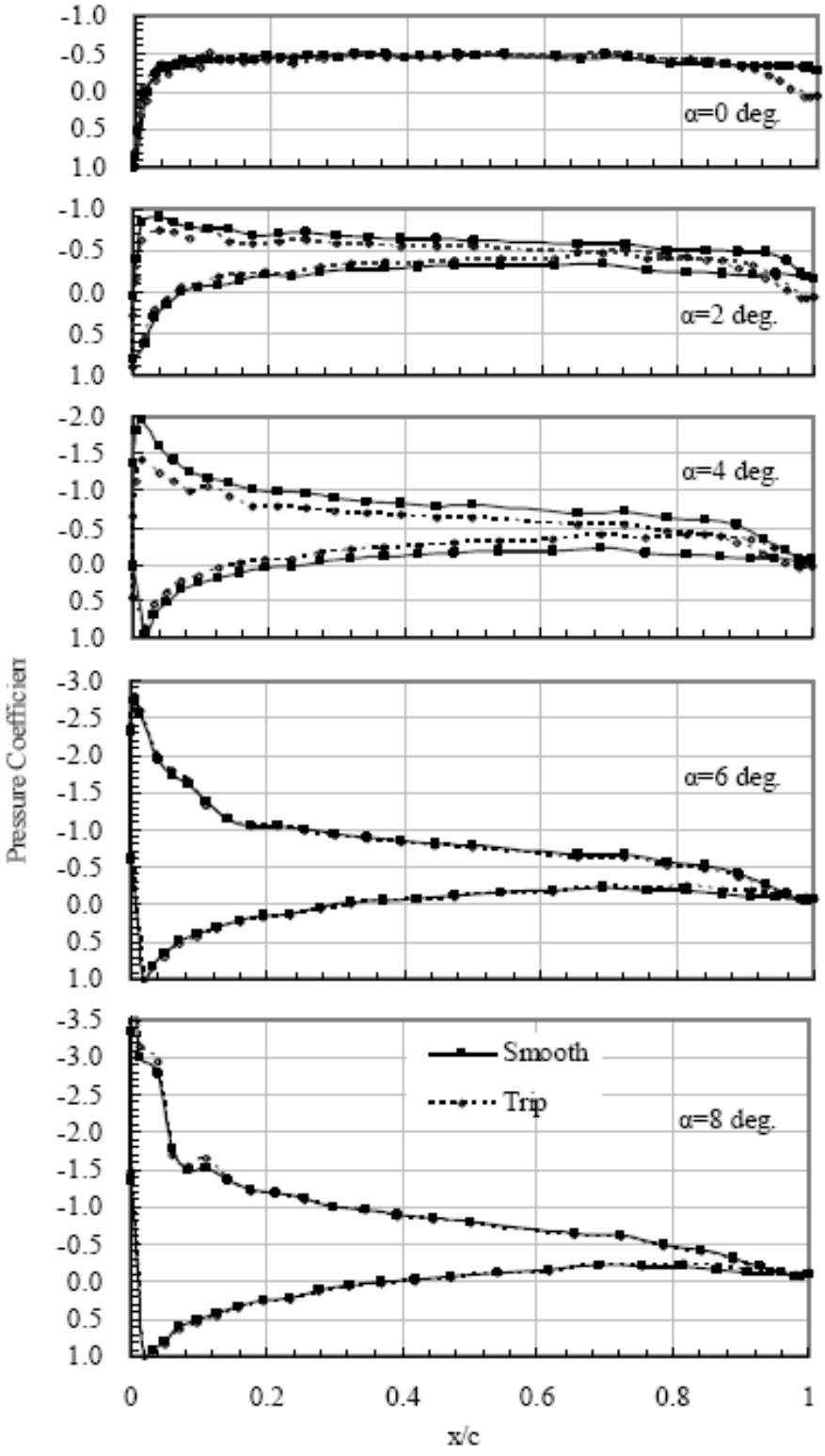

Figure 3.28 Surface pressure distributions at various angles of attack [Obtained from Reference 21]

At α = 8°, a leading edge separation bubble was observed on the suction side of the airfoil, which would explain the drop in surface pressure towards the leading edge of the airfoil. This phenomenon was also observed in CFD analysis.

3.4. COMPARISON OF CFD RESULTS WITH EXPERIMENTAL DATA

By comparing the results obtained from CFD analysis with the results taken from Kwon and Park [21], the CFD analysis methodology was validated. As previously stated, the wake vortex structures shown in the CFD vector and streamline plots compared similarly with PIV plots for the tripped wind-tunnel test cases. Figures 3.29 - 3.33 show comparisons of experimental and CFD flowfield data for various attack angles.

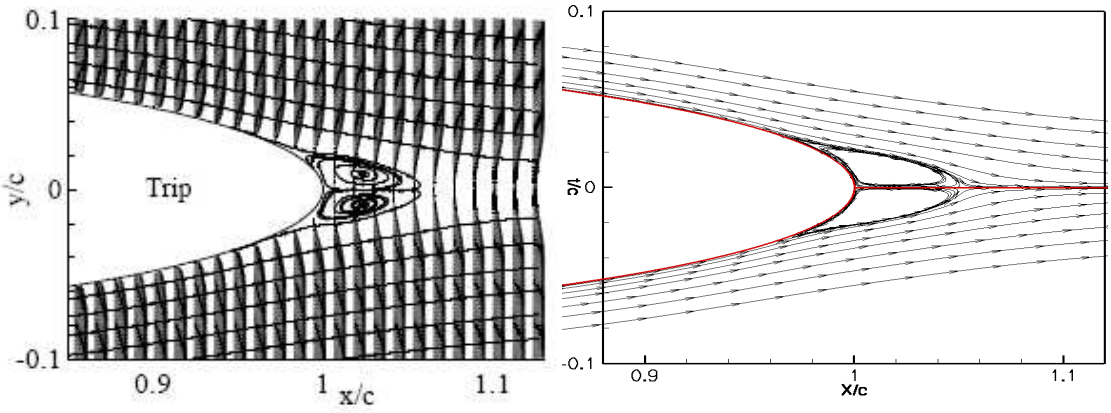

Figure 3.29 Comparison of experimental and CFD flowfield data.
Re=3*10^5, t/c =16%, α = 0°

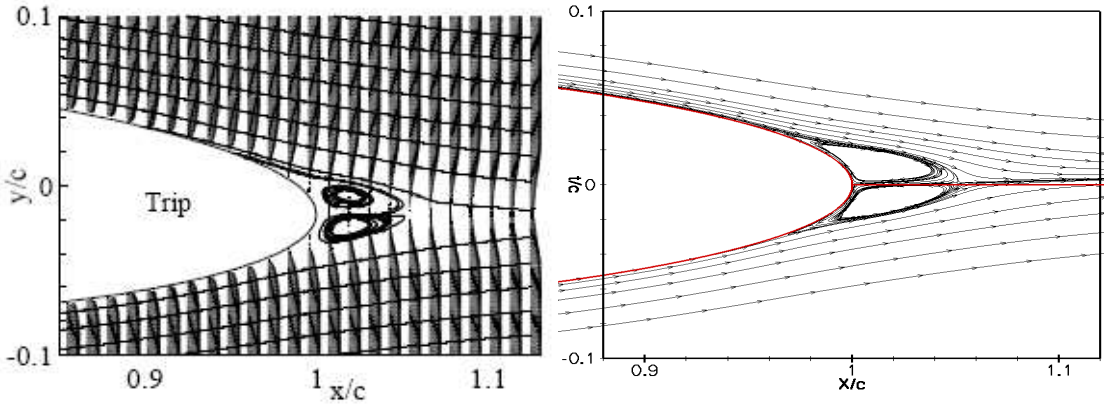

Figure 3.30 Comparison of experimental and CFD flowfield data.
Re=3*10^5, t/c =16%, α = 2°

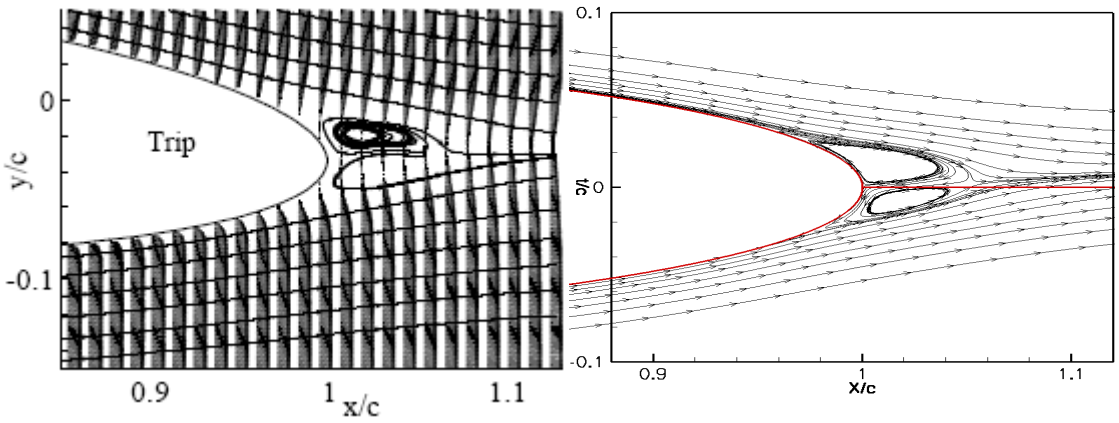

Figure 3.31 Comparison of experimental and CFD flowfield data.
Re=3*10^5, t/c =16%, α = 4°

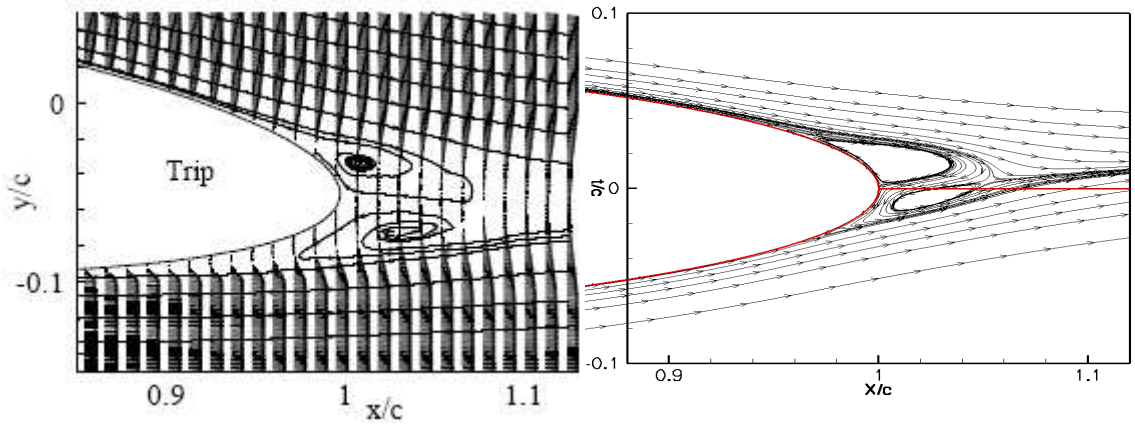

Figure 3.32 Comparison of experimental and CFD flowfield data.
Re=3*10^5, t/c =16%, α = 6°

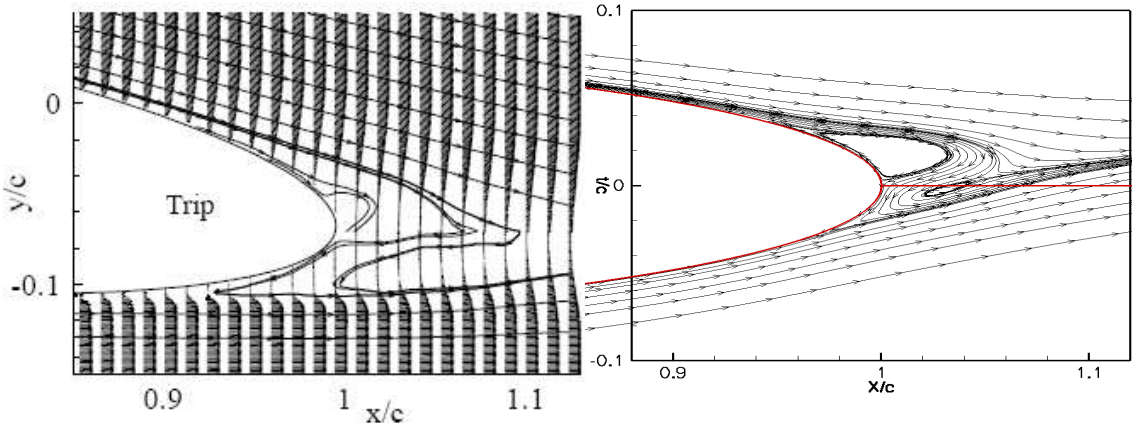

Figure 3.33 Comparison of experimental and CFD flowfield data.
Re=3*10^5, t/c =16%, α = 8°

As can be seen in Figure 3.29, for an angle of attack equal to 0°, boundary layer separation occurred in the tripped wind tunnel testing and in CFD analysis at a location along the x-axis approximately 97% of the chord length away from the leading edge. Also, vortex structures for tripped wind tunnel testing and CFD analysis extended aft the airfoil trailing edge approximately 5% of the chord length along the x-axis. Aft vortex structures on both top and bottom of the airfoil were approximately 2.5% of the chord length in height for both the wind tunnel testing data and CFD analysis.

For an angle of attack equal to 2°, as shown in Figure 3.30, the boundary layer separation point moved forward on the top surface, to 96% of the chord, while the bottom surface boundary layer separation point remained at 97% of the chord. Vortex structure extension past the trailing edge was reduced to 4% chord length for both wind tunnel and CFD data, showing similarity. For CFD data, upper and lower vortex structures shifted slightly upward, causing the upper vortex structure to have slightly more height than the lower. However, a limited number of data points in the wind tunnel plot caused the height of the vortex structures to be difficult to quantify. This tended to be the case for higher angle of attacks, vortex structure data for CFD analysis could easily be compared qualitatively and quantitatively, while a precise quantitative analysis of vortex structure data obtained wind tunnel testing would have been difficult to accomplish. Table 3.1 shows a comparison of vortex structure data obtained from CFD analysis for a 16% thick elliptic airfoil and a Reynolds number of $3 * 10^5$ for various angles of attack.

Table 3-1 Comparison of Flow Separation and Vortex Structure

α	Vortex	0°	2°	4°	6°	8°
Location of Boundary Layer Separation (%c)	Upper	97	96	95.5	95	93
	Lower	97	97	97	97	97
Wake Vortex Length (%c)	Upper	5	4	3.5	3	2
	Lower	5	4	4	4	4
Wake Vortex Height (%c)	Upper	2.5	2.5	3	3	3.5
	Lower	2.5	2	1.5	1	0.5

Surface pressure distribution plots obtained from CFD analysis compared similarly with surface distribution plots from tripped wind-tunnel test cases. Comparison

of CFD analysis results with wind-tunnel results showed more similarity at low angles of attack for tripped wind-tunnel test cases. At attack angles of 6° and greater CFD analysis compared similarly with both smooth and tripped wind-tunnel test cases. However, some contrast was observed between CFD analysis and wind-tunnel testing results regarding surface pressure distribution on the lower side of the blunt trailing edge. While observation of both CFD analysis and wind-tunnel testing showed strong suction forces along the front upper side of the airfoil, wind-tunnel testing results did not show suction forces along the convex lower side, as was observed in CFD analysis results.

A theoretical description of the lifting characteristics of an elliptic section was given by Hoerner [28]. Hoerner illustrated the flow over elliptic airfoils, shown in Figure 3.34, as having two separation points which move around the trailing edge from the pressure side to the suction side, creating suction on the lower side of the trailing edge.

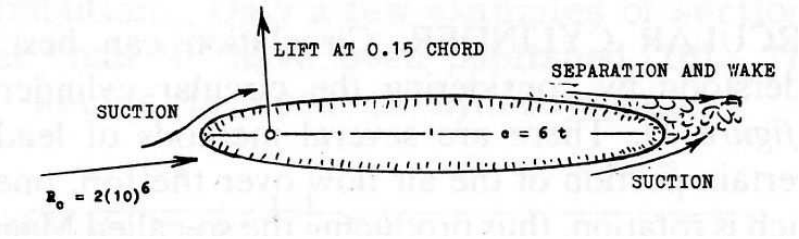

Figure 3.34 Flow characteristics over an elliptic section from Hoerner [28]

Hoerner also states that strong suction forces on the upper side of the leading edge, coupled with suction forces on the lower side of the trailing edge causes the center of lift to move to approximately 15% of the chord length. Also, the suction on the bottom side of the trailing edge would cause a small decrease in the lift coefficient of the airfoil. This phenomenon was observed more distinctly in CFD analysis than in the results of the wind-tunnel test cases. As shown in Figures 3.35, below, wind tunnel test results for tripped flow exhibited higher lift coefficients than was calculated by Hoerner for attack angles greater than 2°. Data for lift coefficient obtained from CFD analysis is plotted in a similar graph, Figure 3.36, below.

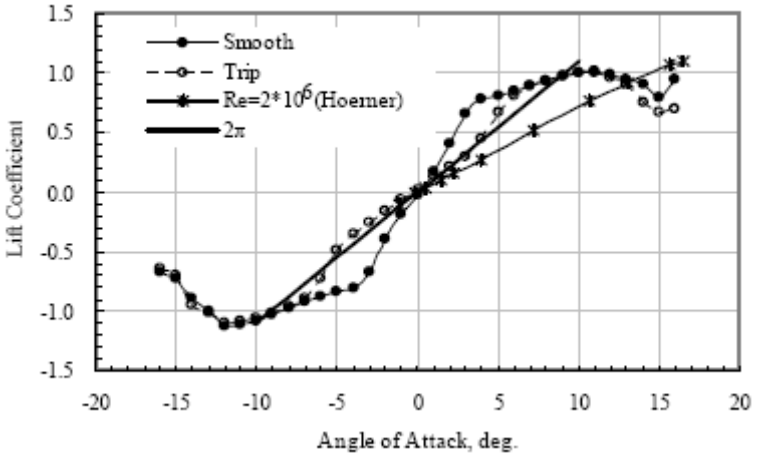

Figure 3.35 Lift coefficient with respect to angle of attack [Obtained from Reference 21]

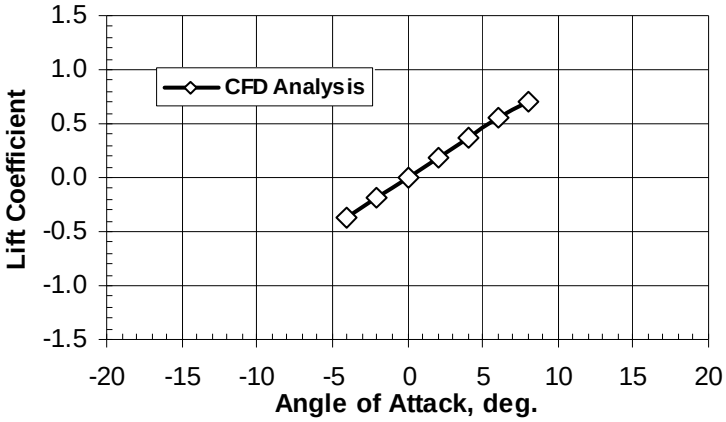

Figure 3.36 Lift coefficient with respect to angle of attack obtained using FOMOCO

As shown in Figure 3.36, above, results for lift coefficient observed from CFD analysis followed closely to results from Hoerner and wind-tunnel testing for attack angles of 2° and less. At higher attack angles, results of CFD analysis follows the symmetric lift coefficient of $2\pi\alpha$ up to $\alpha = 6°$. Greater than 6° the lift slope decreases similarly to the lift slope calculated by Hoerner, while the lift slope observed from wind-tunnel testing increased. Between $\alpha = 4°$ and $\alpha = -4°$, CFD data for lift coefficient stays within 0.05 below experimental data. Between 4° and 8°, experimental data diverges

away from CFD data. At α = 8°, experimental data begins to converge back towards CFD data, coming within 0.2 of the CFD data.

Although some contrast was observed between results of CFD analysis and wind-tunnel testing for lift coefficient, results for drag coefficient obtained from CFD analysis compared equivalently to results of tripped wind-tunnel test cases. Figure 3.37 shows the results of wind-tunnel testing for drag coefficient as a function of attack angle, while Figure 3.38 shows a similar plot for results of CFD analysis. For drag coefficient, CFD data and experimental tripped data remain within 0.002 for α < 4°. For 4° and greater, drag coefficient data for experimental and CFD remain within 0.01.

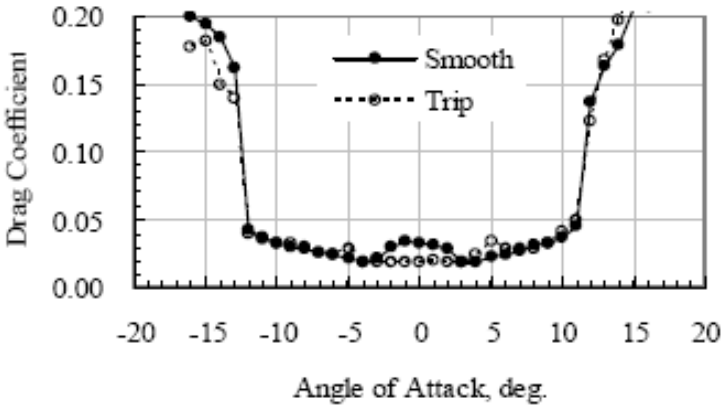

Figure 3.37 Drag coefficient with respect to angle of attack [Obtained from Reference 21]

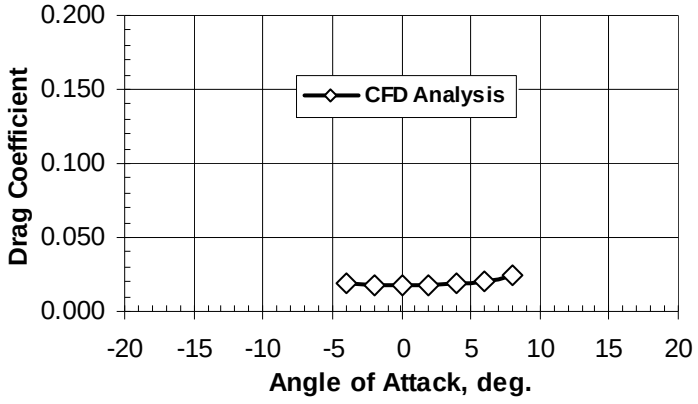

Figure 3.38 Drag coefficient with respect to angle of attack obtained using FOMOCO

As shown in Figures 3.37 and 3.38, above, results obtained from CFD analysis for drag coefficient appeared to be unaffected by increased suction on the lower side of the

trailing edge. This was demonstrated in that the drag coefficient plots for results of wind-tunnel testing and CFD analysis were identical.

3.4.1. Note on Pitching Moment Coefficient. Also investigated in this study, was the pitching moment coefficient. Figure 3.39 shows wind tunnel results for Pitching Moment Coefficient (C_M) with respect to angle of attack from Kwon [21]. Figure 3.40 shows results obtained for the C_M of a 16% thick elliptic airfoil at a Reynolds number of $3*10^6$ with respect to angle of attack.

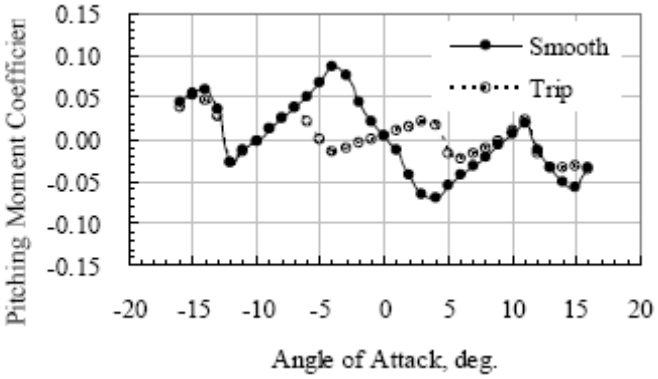

Figure 3.39 – Pitching Moment Coefficient with respect to Angle of Attack [Obtained from Reference 21]

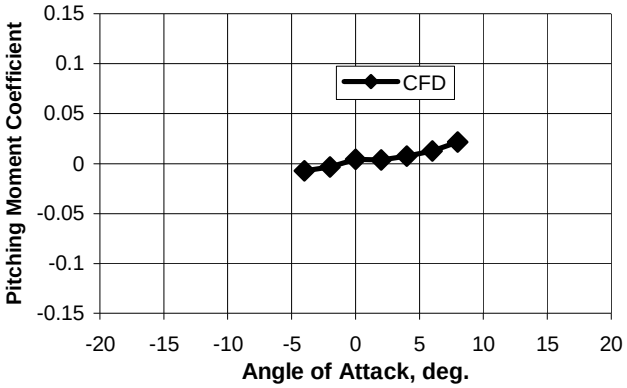

Figure 3.40 – Pitching Moment Coefficient with respect to Angle of Attack obtained using FOMOCO

As can be seen in Figure 3.39 and Figure 3.40, results obtained from CFD compared more closely to wind tunnel results for tripped flow than with wind tunnel results for smooth flow obtained from Kwon [21].

3.5. CONCLUDING REMARKS

The purpose of the validation test case was to verify the methodology used to obtain flowfield simulations about elliptic airfoils using CFD analysis. Validation of methodology was accomplished by comparing results obtained from CFD analysis with experimental wind-tunnel testing results. Comparison of results obtained from CFD analysis with wind-tunnel testing results showed that simulated flowfields of each compared similarly, as demonstrated by:

1) Wake vortex structures shown in the CFD vector and streamline plots compared well with PIV plots for the tripped wind-tunnel test cases.
2) Surface pressure distribution plots obtained from CFD analysis compared similarly with surface distribution plots from tripped wind-tunnel test cases.
3) Results for lift coefficient observed from CFD analysis followed closely to results from Hoerner and wind-tunnel testing for most attack angles.
4) Results for drag coefficient obtained from CFD analysis compared well to results of tripped wind-tunnel test cases.

While most of the results observed in the comparison of CFD analysis with wind-tunnel testing showed similar trends, contrast was observed in the flow around the lower side of the airfoil trailing edge. Results of CFD analysis showed greater suction force on the lower side of the airfoil trailing edge when compared with tripped wind-tunnel test case results. Overall, flowfield simulations generated using CFD analysis compared similarly to results obtained using experimental wind-tunnel analysis. This conclusion allows for reasonable verification of the methodology employed to simulate flowfields about an elliptical airfoil using CFD analysis.

4. RESULTS AND DISCUSSION

4.1. PARAMETRIC STUDY OF ELLIPTIC AIRFOIL PERFORMANCE

The goal of this study is to investigate the performance and aerodynamic characteristics of elliptic airfoils for a range of parameters. These parameters included: Reynolds number, thickness ratio, and angle of attack. Reynolds number was evaluated at values of $1*10^5$, $3*10^5$, $2*10^6$, and $8*10^6$. The Reynolds number range was chosen to show an identifiable effect on aerodynamic performance and are varied for a reasonable range of rotary and fixed wing flight conditions: high Reynolds numbers during rotary flight, low Reynolds numbers during transition, and medium-ranged Reynolds numbers during fixed-wing flight. Thickness ratio was evaluated for a range between 5% and 25% to account for a reasonable range of airfoil thicknesses that would be used on UAVs. Angle of attack was evaluated from 0° to 20° in order to analyze aerodynamic characteristics up to stall condition. Angle of attack was not studied for negative attack angles because the airfoil is symmetric and the results would mirror the positive attack angles. This section contains the results of the parametric study and discussion of the primary conclusions.

4.1.1. Influence Reynolds Number on Airfoil Lift Characteristics.

Aerodynamic performance for a 16% thick was determined using the methods developed in Chapter 2 and evaluated in Chapter 3. Plots of C_L and $C_{D,}$ for attack angles ranging from 0° to 20°, or until stall, were created for Reynolds numbers of $1*10^5$, $3*10^5$, $2*10^6$, and $8*10^6$. These Reynolds numbers were chosen to show changes in aerodynamic performance at different phases of fixed wing flight. A Reynolds number of $3*10^5$ would be observed for low speed flight and could also be used to analyze aerodynamic performance of miniature UAVs. The CRW UAV would have a Reynolds number of approximately $2*10^6$ during fixed wing flight while flying close to transition speed. The Reynolds number observed by the CRW UAV at maximum flight speed would be approximately $8*10^6$. Figure 4.1 shows a comparison of results for lift coefficient over the range of Reynolds numbers between $1*10^5$ and $8*10^6$.

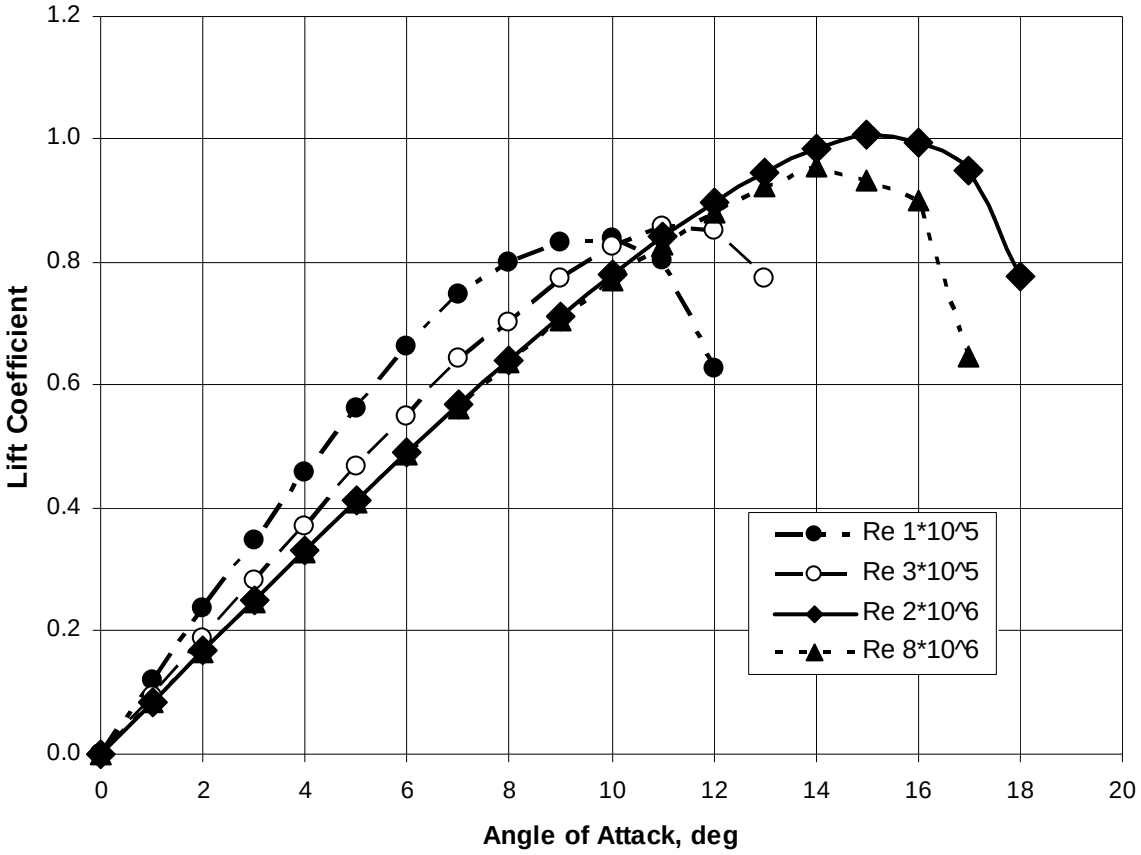

Figure 4.1 - Dependence of Lift Coefficient on angle of attack for a range of Reynolds number between $1*10^5$ and $8*10^6$.
t/c = 16%

As can be seen in Figure 4.1, for angles of attack between 0° and 8°, lower Reynolds numbers showed improved lift performance over higher Reynolds numbers. At 7° angle of attack, the lift coefficient at a Reynolds number equal to $1*10^5$ (approximately 0.74) showed an increase of 0.18 over lift coefficient at a Reynolds number equal to $8*10^6$ (approximately 0.56), which is a 32.5% improvement in lift. At 8° angle of attack, the lift coefficient at a Reynolds number equal to $1*10^5$ (approximately 0.80) showed an increase of 0.16 over lift coefficient at a Reynolds number equal to $8*10^6$ (approximately 0.64), which is a 25.7% improvement. For lower angles of attack, improvement in Lift Coefficient ranged up to 43.7%. In order to take a closer look into

lift performance at low angles of attack, Figure 4.2 shows the dependence of lift coefficient on angles of attack between 0° and 6° for a range of Reynolds number between $1*10^5$ and $8*10^6$.

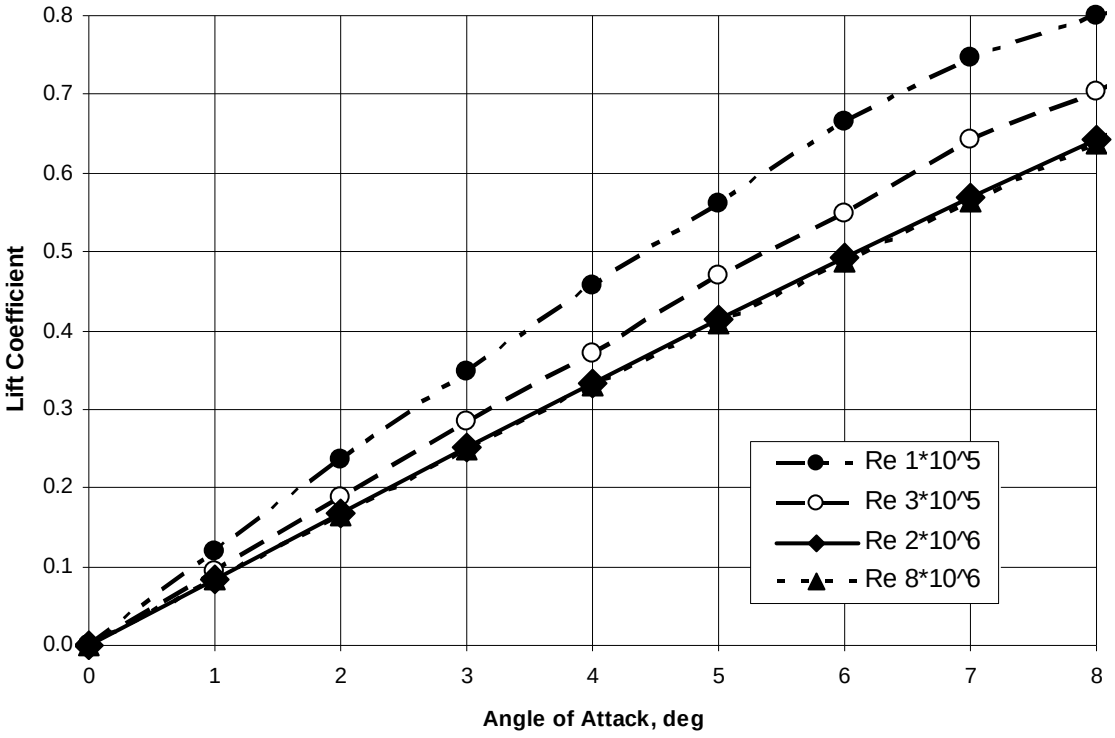

Figure 4.2 - Dependence of Lift Coefficient on angle of attack for a range of Reynolds numbers between $1*10^5$ and $8*10^6$.
t/c = 16%

Figure 4.2 shows more closely the effects of lower Reynolds numbers on lift performance in the small angle of attack region. As can be seen in Figure 4.1, lower Reynolds numbers (in the 10^5 region) showed significant improvement in lift slope for attack angles less that 6°. Improvements in lift slope for the range of Reynolds numbers investigated were calculated to be between 30% improvement, 0.024 1/° at 6° angle of attack, to 40% improvement, 0.036 1/° at 1° angle of attack. As can be noted, the dependence of lift coefficient on angle of attack showed to be slightly non-linear, which

would account for the decrease in lift slope as angle of attack increases, as shown in Table 4.1. Table 4.1 shows lift slopes for the investigated range of Reynolds numbers.

Table 4.1 - Lift slopes for the investigated range of Reynolds numbers and average Lift Slope for attack angles between 0 and 6 degrees

Angle of Attack	Reynolds Number			
	Re $1*10^5$	Re $3*10^5$	Re $2*10^6$	Re $8*10^6$
1	0.1198	0.0951	0.0839	0.0834
2	0.1167	0.0920	0.0836	0.0830
3	0.1122	0.0973	0.0829	0.0823
4	0.1083	0.0873	0.0819	0.0813
5	0.1055	0.0981	0.0805	0.0800
6	0.1021	0.0797	0.0787	0.0781
Average	**0.1108**	**0.0916**	**0.0819**	**0.0813**

The data presented in Table 4.1 can be more easily interpreted by looking at the dependency of lift slope average on Reynolds number, as seen in Figure 4.3.

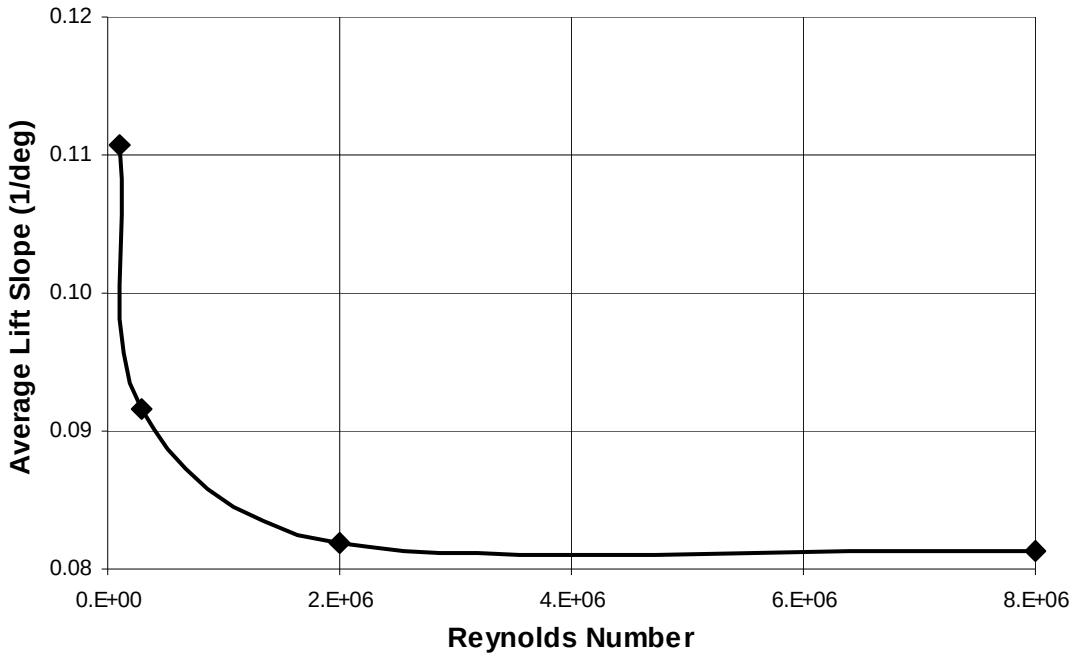

Figure 4.3 - Dependence of Average Lift Slope on Reynolds number, for $\alpha \in [0°, 6°]$. t/c = 16%

As can be seen in Figure 4.3, the average lift slope drops significantly between Reynolds numbers of $1*10^5$ and $2*10^6$, however, for Reynolds numbers greater than $2*10^6$, average lift slope showed little to no change. Presumably, this observation shows how lift performance is affected as the Reynolds number transitions into the purely laminar flow range.

Although Reynolds numbers in the 10^5 range showed better lift performance for attack angles between 0° and 8°, greater lift performance was observed Reynolds numbers in the 10^6 range at attack angles greater than 10°. This observation was supported by observation of stall angle, based on numerical results. In this study, stall angle was defined as the observed angle of attack at which the lift coefficient drops below the maximum lift coefficient. Stall angle observed for results obtained at a Reynolds number of $2*10^6$ was 5° higher than stall angle observed for results obtained at a Reynolds number of $1*10^5$. Presumably, this observation was caused by the higher Reynolds number flow having enough energy to prevent flow separation up to higher angles of attack. Figure 4.4 shows the dependence of stall angle on Reynolds number for a range of Reynolds numbers between $1*10^5$ and $8*10^6$.

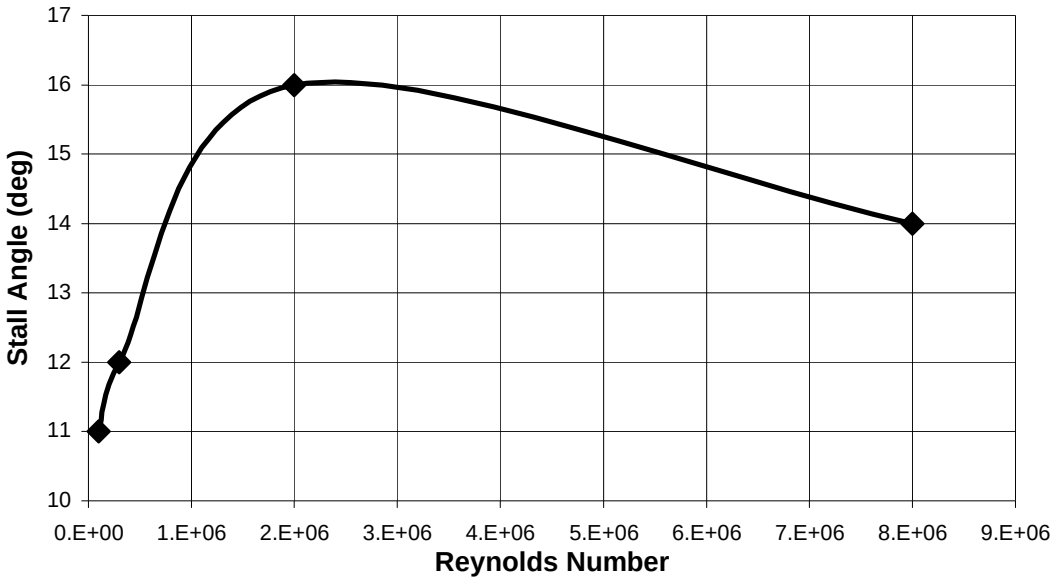

Figure 4.4 - Dependence of Stall Angle on Reynolds number for a range of Reynolds numbers between $1*10^5$ and $2*10^6$.
t/c = 16%

Figure 4.4 shows that significant improvements in stall characteristics were obtained for Reynolds numbers in the 10^6 range. However, at a Reynolds number of $8*10^6$, results can be observed to stall at 2° lower than results obtained at $2*10^6$. This observation could be linked to larger vortex separation aft of the airfoil which occurs at this higher value of Reynolds number. Another lift performance characteristic, maximum lift coefficient ($C_{L,max}$) was observed to have similar trends as stall angle. Figure 4.5 shows the dependence of $C_{L,max}$ on Reynolds number.

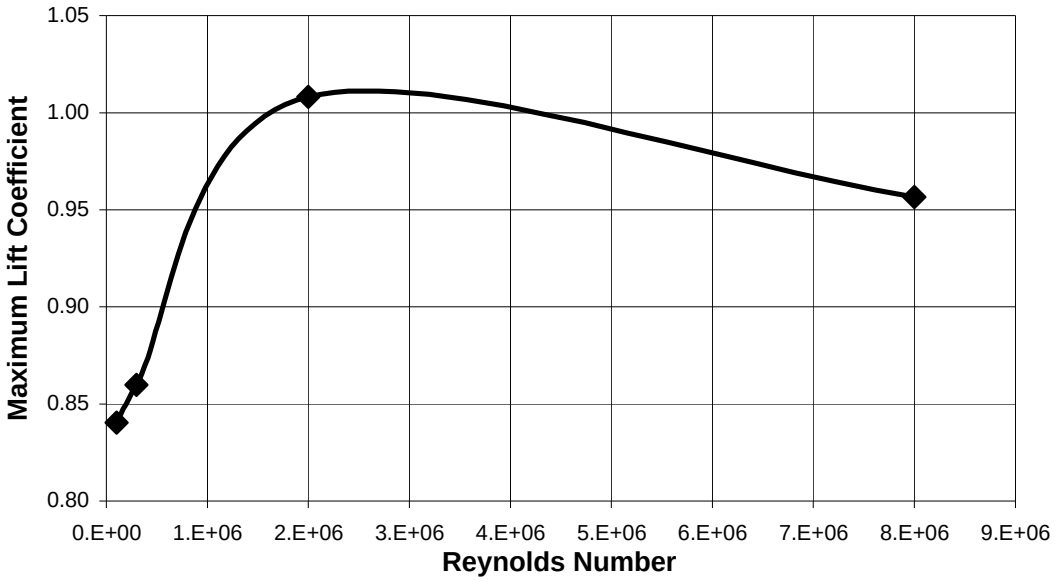

Figure 4.5 - Dependence of Maximum Lift Coefficient on Reynolds number for a range of Reynolds numbers between $1*10^5$ and $8*10^6$.
t/c = 16%

As can be seen in Figure 4.5, Reynolds numbers in the 10^5 range resulted in maximum lift coefficients in the 0.84 to 0.86 range, while the maximum lift coefficient observed at a Reynolds number of $2*10^6$ showed to be greater than 1.0, an increase in, roughly, 15%. However, at a Reynolds number of $8*10^6$, a maximum lift coefficient of 0.96 was observed, which resulted in only a 10% increase over the results observed in the

10^5 Reynolds number range and a 5% drop from results obtained at a Reynolds number of $2*10^6$. Presumably, this data would show that there is an optimal Reynolds number to be found in between $1*10^6$ and $3*10^6$. More analysis would need to be conducted for Reynolds numbers in the $1*10^6$ to $3*10^6$ range to determine the optimal value.

4.1.2. Influence of Reynolds Number on Airfoil Drag Characteristics.

Another aerodynamic performance characteristic investigated in this parametric study of Reynolds number was drag coefficient. Figure 4.6 shows the dependence of drag coefficient on angle of attack for a range of Reynolds numbers between $1*10^5$ and $2*10^6$.

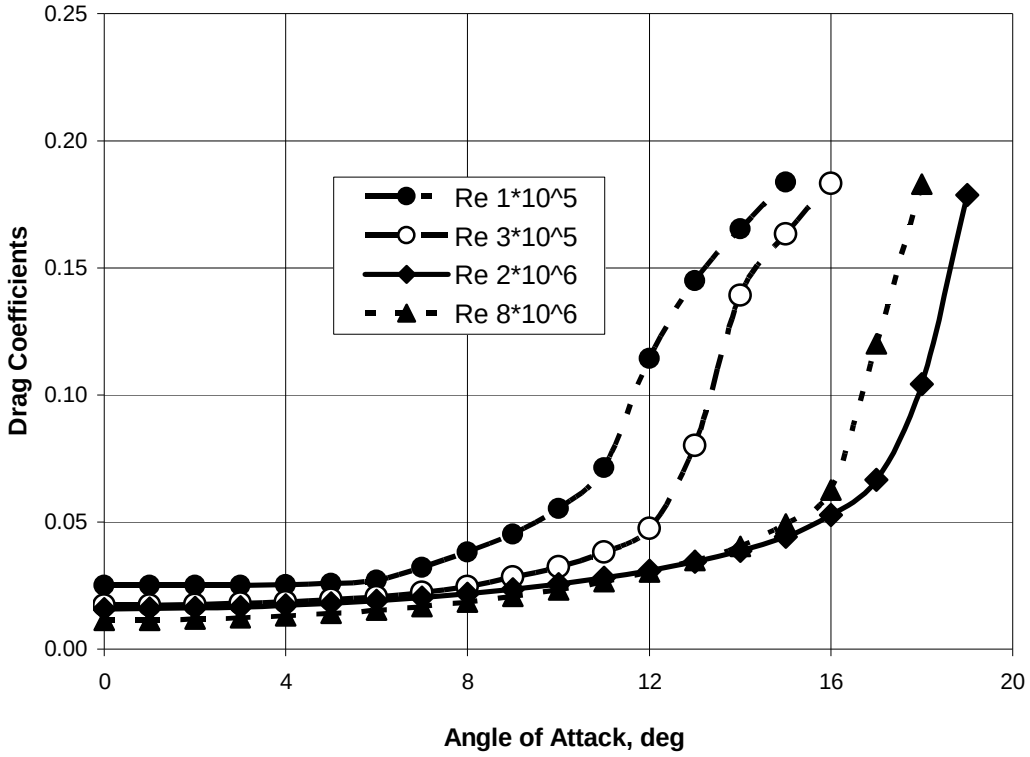

Figure 4.6 - Dependence of Drag Coefficient on angle of attack for a range of Reynolds numbers between $1*10^5$ and $8*10^6$.
t/c = 16%

As can be seen in Figure 4.6, the Drag Coefficients for the range of Reynolds number derivate non-linearly away from each other as attack angle increases. In Figure 4.6, drag performance observed for Reynolds numbers in the 10^5 range was consistently

worse than drag performance observed for Reynolds number in the 10^6 range. For angles of attack between 0° and 12°, the highest investigated Reynolds number (Re = $8*10^6$) was observed to have the best drag performance. However, since analysis showed that at a Reynolds number of $8*10^6$ a 16% elliptic airfoil begins to stall at a lower angle of attack than was observed for the same airfoil at a Reynolds number of $2*10^6$. Therefore, for angles of attack greater than 12°, better drag performance was observed at a Reynolds number of $2*10^6$ than at a Reynolds number of $8*10^6$.

An important aspect of this study focuses on the aerodynamic performance of elliptic airfoils in a range of attack angles in the 0° and 8°. In this range the largest amount of flying, for high speed UAVs, is conducted. Figure 4.7 shows the dependence of drag coefficient on angle of attack for a range of Reynolds numbers between $1*10^5$ and $8*10^6$ and for a range of attack angles between 0° and 8°.

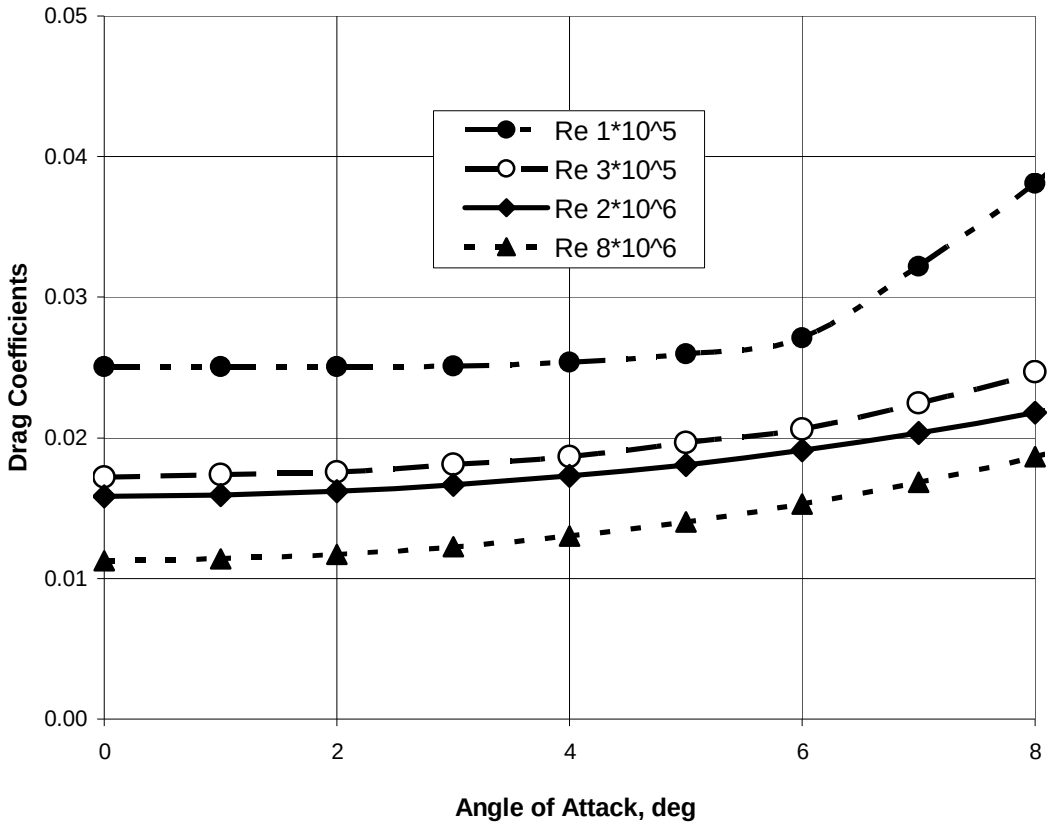

Figure 4.7 - Dependence of drag coefficient on angle of attack for a range of Reynolds numbers between $1*10^5$ and $2*10^6$.
t/c = 16%

4.1.3. Influence of Reynolds Number on Lift to Drag Performance. The overall performance of an airfoil can be better understood by observing the influence of a parameter on both lift and drag simultaneously, in the form of lift to drag ratio (L/D). Lift to drag ratio is defined as the observed lift coefficient divided by the observed drag coefficient. The dependence of lift to drag ratio on angle of attack for a range of Reynolds numbers is shown in Figure 4.8 below.

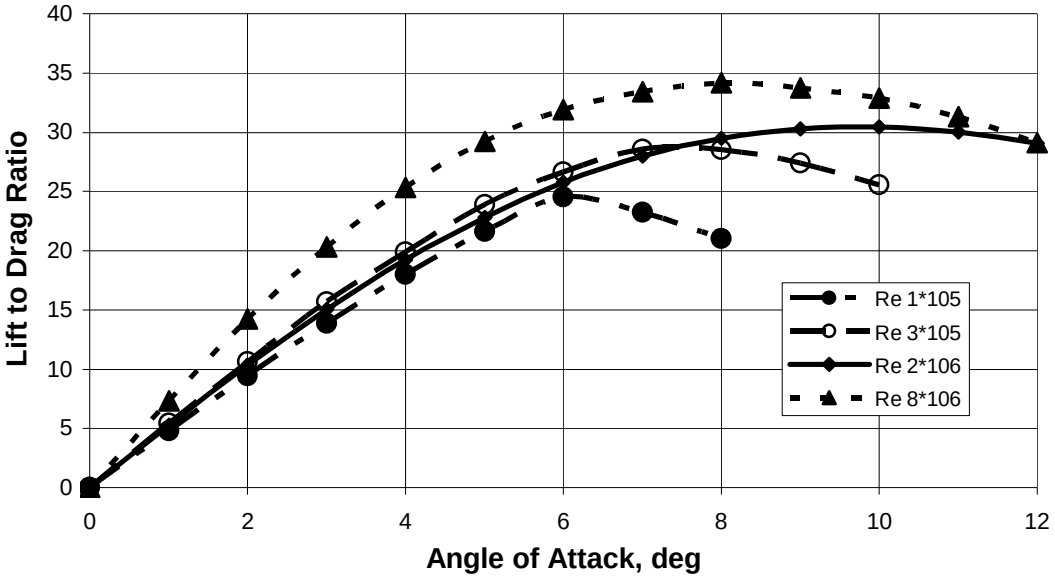

Figure 4.8 - Dependence of Lift to Drag Ratio on Angle of Attack and Reynolds number. t/c = 16%

As can be seen in Figure 4.8, lift to drag performance improves as Reynolds number increases. This comparison of lift to drag performance was the most comprehensive criteria for evaluating overall airfoil performance. Figure 4.8 shows clearly that the evaluated airfoil performed best at a Reynolds number of $8*10^6$. Also, the maximum observed L/D for the range of Reynolds numbers evaluated increased as Reynolds number increased. This was observed more decisively by plotting the dependence of maximum observed L/D on Reynolds number, as shown in Figure 4.9. As can be seen in Figure 4.9, the maximum observed lift to drag ratio for the evaluated elliptic airfoil at a Reynolds number of $8*10^6$ (approximately 34) was approximately 10

units greater than the maximum observed lift to drag ratio for the evaluated elliptic airfoil at a Reynolds number of $1*10^5$ (approximately 24), which was a 42% improvement in lift to drag performance. Presumably, the cause of this contrast in airfoil performance is due to the reluctance of an elliptic airfoil at high Reynolds numbers to stall until higher angle of attacks are reached.

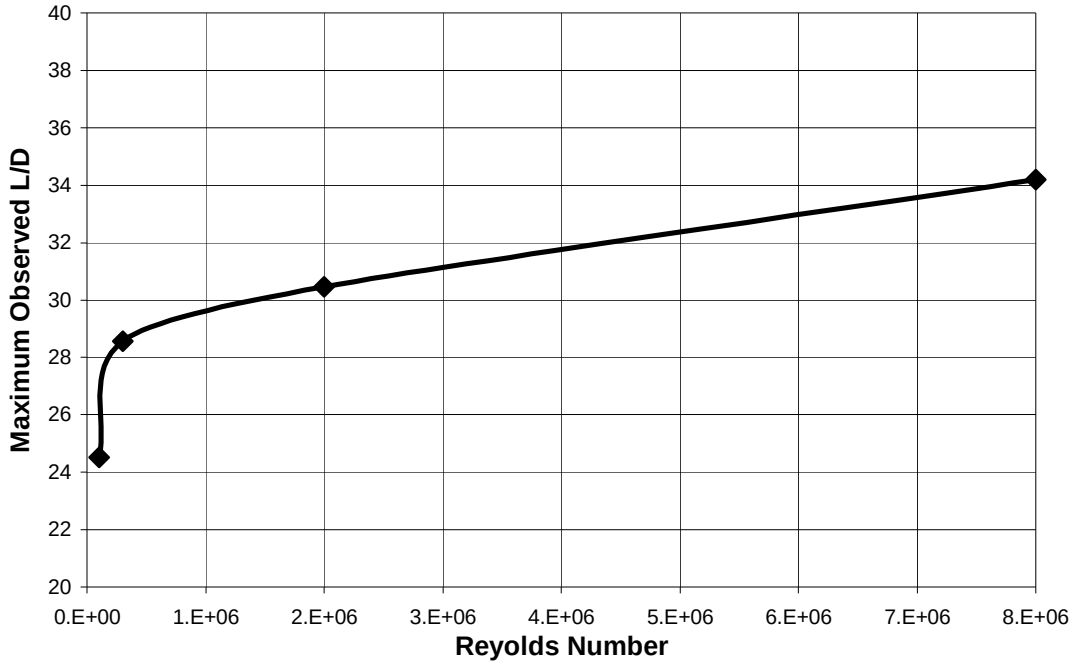

Figure 4.9 - Dependence of Maximum Observed Lift to Drag Ratio on Reynolds number. t/c = 16%

Based on the results of the L/D comparison, airfoil performance tends to improve as Reynolds number is increased. At higher Reynolds numbers, the evaluated airfoil was able to achieve greater maximum lift coefficients through prevention of stall until higher angles of attack. Also, the evaluated airfoil was observed to produce less drag as Reynolds number was increased. These factors combined to cause the lift to drag ratio to improve as Reynolds number was increased.

4.1.4. Influence of Reynolds Number on Pitching Moment. Also investigated in this study was the influence of Reynolds number on pitching moment. Pitching moment is important to aircraft design because affects the stability and control of the aircraft. Therefore, determination of the pitching moment coefficient (C_M) has an affect

on wing and tail design. The influence of Reynolds number on C_M was found employing FOMOCO to determine the dependence of C_M on Reynolds number and angle of attack. Figure 4.10 shows results obtained for C_M for a 16% thick elliptic airfoil over a range of Reynolds numbers between $1*10^5$ and attack angles between 0° and 20°.

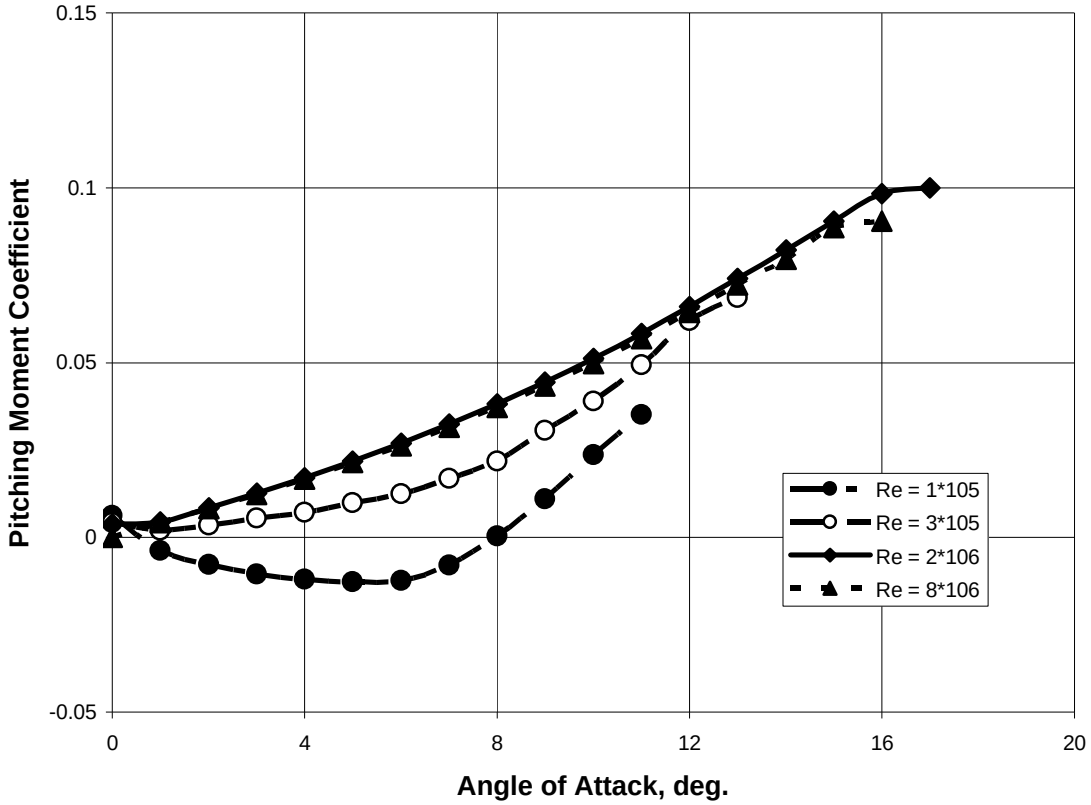

Figure 4.10 – Dependence of Pitching Moment Coefficient on Reynolds number. t/c = 16%

As can be seen in Figure 4.10, for Reynolds numbers between $1*10^5$ and $2*10^6$, the pitching moment coefficient was found to increase as Reynolds number increased. At a Reynolds number of $8*10^6$, the moment coefficient decreased slightly than that of $2*10^6$, but was approximately equivalent for angles of attack less than or equal t 15°.

4.1.5. Influence of Reynolds Number on Flow Developments. In order to better understand the influence of Reynolds number on airfoil performance, further examination into contour plots of streamlines for varying Reynolds numbers was conducted to show visualizations of how trailing edge vortices and leading edge separation bubbles may

affect the aerodynamic characteristics of an elliptic airfoil. Figure 4.11 shows contour plots of streamlines for a 16% thick elliptic airfoil at Reynolds numbers of $1*10^5$, $3*10^5$, $2*10^6$, and $8*10^6$. For these visualizations, an attack angle of 10° was selected to show differences in flow fields at an angle were similar lift performance was observed for each Reynolds number.

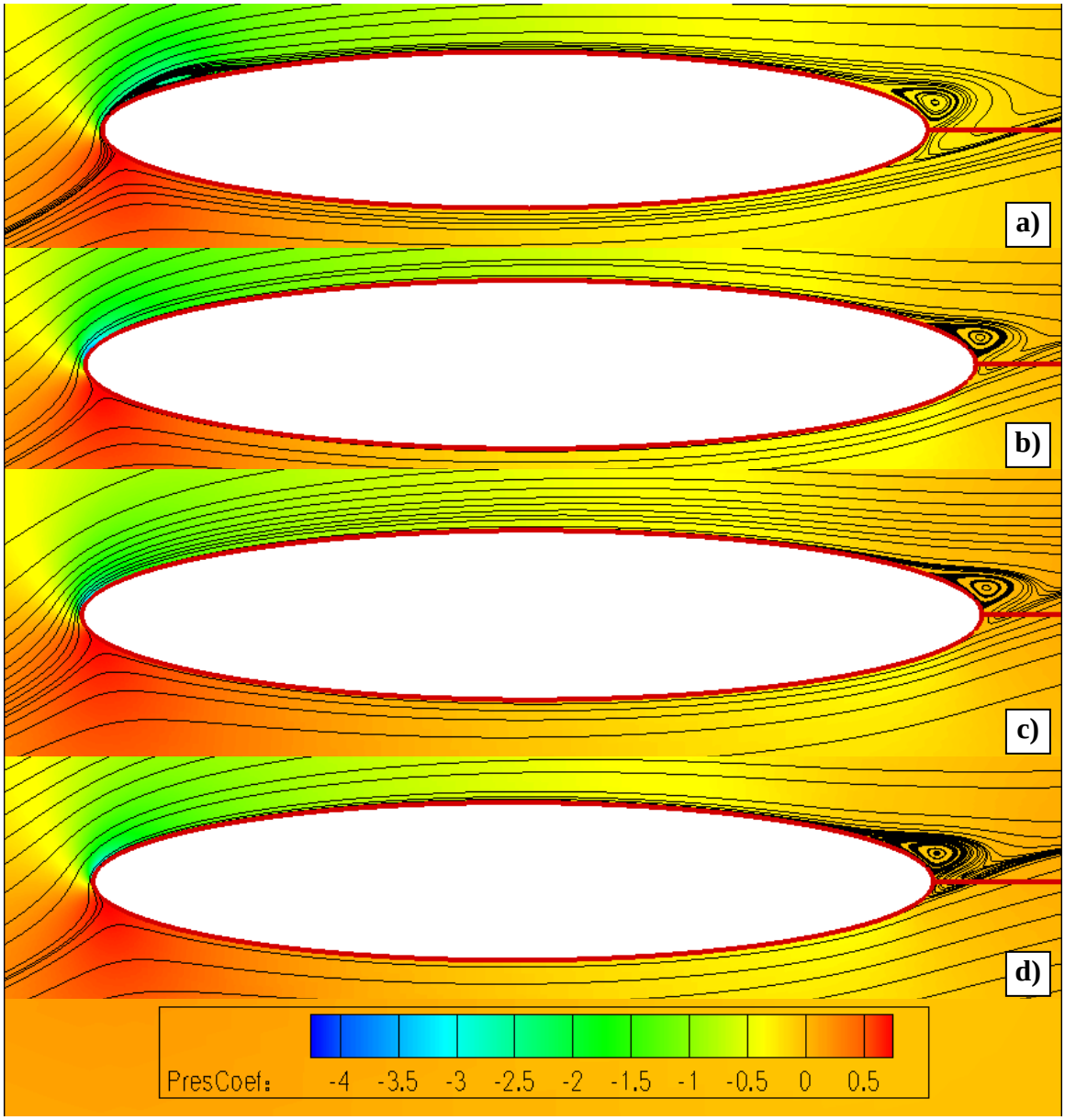

Figure 4.11 – Pressure distribution and flow streamlines around elliptic airfoil for various Reynolds numbers.
t/c = 16%, α= 10°
a)Re = $1*10^5$, b)Re = $3*10^5$, c)Re = $2*10^6$, d)Re = $8*10^6$

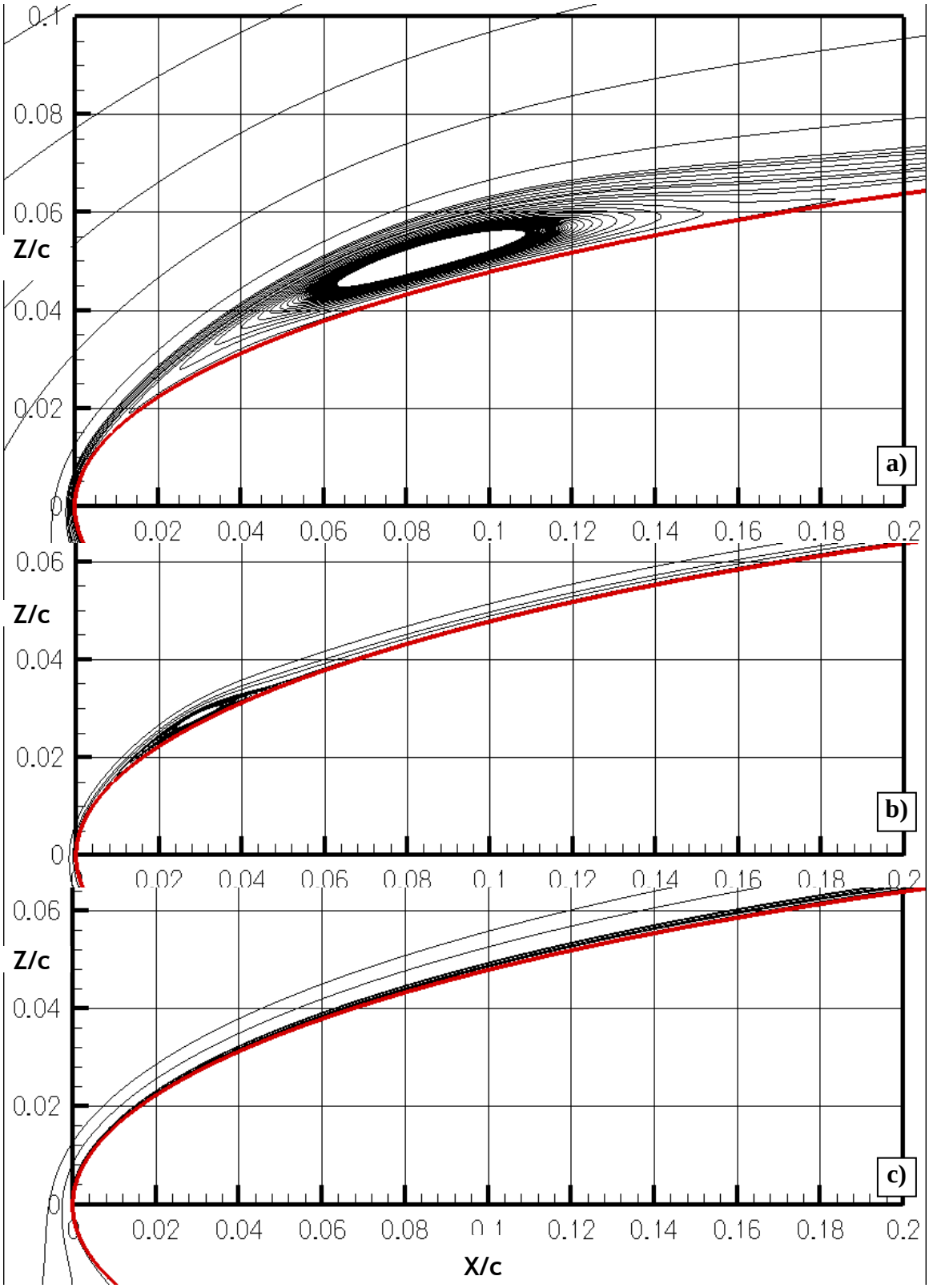

Figure 4.12 – Streamline visualizations of flow developments close to leading edge.
t/c = 16%, α = 10°
a) Re = $1*10^5$, b) Re = $3*10^5$, c) Re = $2*10^6$

As can be seen in Figure 4.11, flow characteristics of a 16% thick elliptic airfoil for a range of Reynolds number while at an attack angle of 10° include aft vortex shedding at all Reynolds number, however, leading edge separation bubbles were only observed at Reynolds number in the 10^5 range. Reynolds numbers of $1*10^5$ and $3*10^5$ exhibited separation bubbles close to the leading edge of the lifting surface.

Figure 4.12, above, shows close-up views of the separation bubble development on the leading edge of the airfoil for Reynolds numbers of $1*10^5$ and $3*10^5$, and Figure 4.12-c shows that no separation over the leading edge occurred at a Reynolds number of $2*10^6$. As can be seen in Figure 4.12, at a Reynolds number of $1*10^5$, a large separation bubble was observed just aft of the leading edge. However, at a Reynolds number of $3*10^5$, a very small separation bubble was observed very close to the tip of the airfoil leading edge. These observations showed that leading edge separation bubbles would have a significant effect on aerodynamic characteristics at a Reynolds number of $1*10^5$, a minor effect on aerodynamic characteristics at a Reynolds number of $3*10^5$, and no effect on aerodynamic characteristics at a Reynolds number of $2*10^6$.

Presumably, the formation of a laminar separation bubble over the leading edge of an elliptic airfoil was affected significantly by variants of energized flow at differently Reynolds numbers. At a Reynolds number of $1*10^5$, when the flow would be the least energized, the largest separation bubble was formed. This separation bubble was observed to have a height of approximately 1% chord of the airfoil and a length of 18% chord of the airfoil. At a Reynolds number of $3*10^5$, the separation bubble was observed to have a height less than 0.5% of the airfoil chord length and a length of approximately 4% of the airfoil chord length, which was, roughly, a 78% decrease in length.

The effect of the separation bubbles on the lift characteristics of an elliptic airfoil became more apparent when the surface pressure distributions were investigated. Plots of surface pressure distribution over the upper and lower airfoil surfaces showed a noticeable drop in pressure in the locale of the preciously observed separation bubbles. Figure 4.13 shows plots of surface pressure distribution for Reynolds numbers between $1*10^5$ and $8*10^6$.

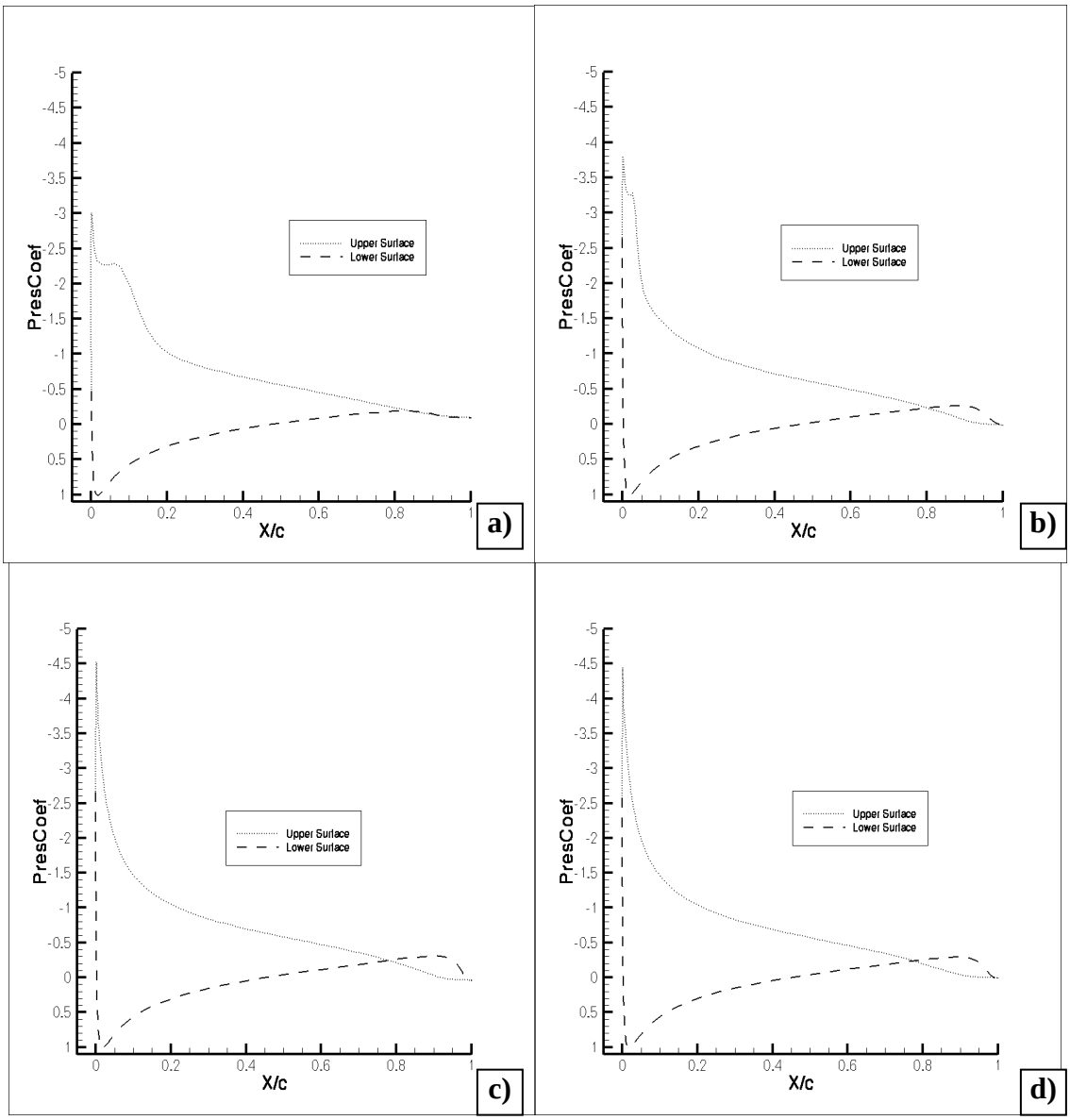

Figure 4.13 – Plots of surface pressure distribution showing pressure drops caused by separation bubbles over the leading edge.
t/c = 16%, α = 10°
a) Re = $1*10^5$, b) Re = $3*10^5$, c) Re = $2*10^6$, d) Re = $8*10^6$

A significant contrast can be observed in Figure 4.11 regarding aft vortex shedding. As can be seen in Figure 4.6, results for drag coefficients improve for increasing Reynolds number when the angle of attack is 10°. This can be further investigated by examining more closely the vortex structures aft of the trailing edge for the range of Reynolds numbers evaluated.

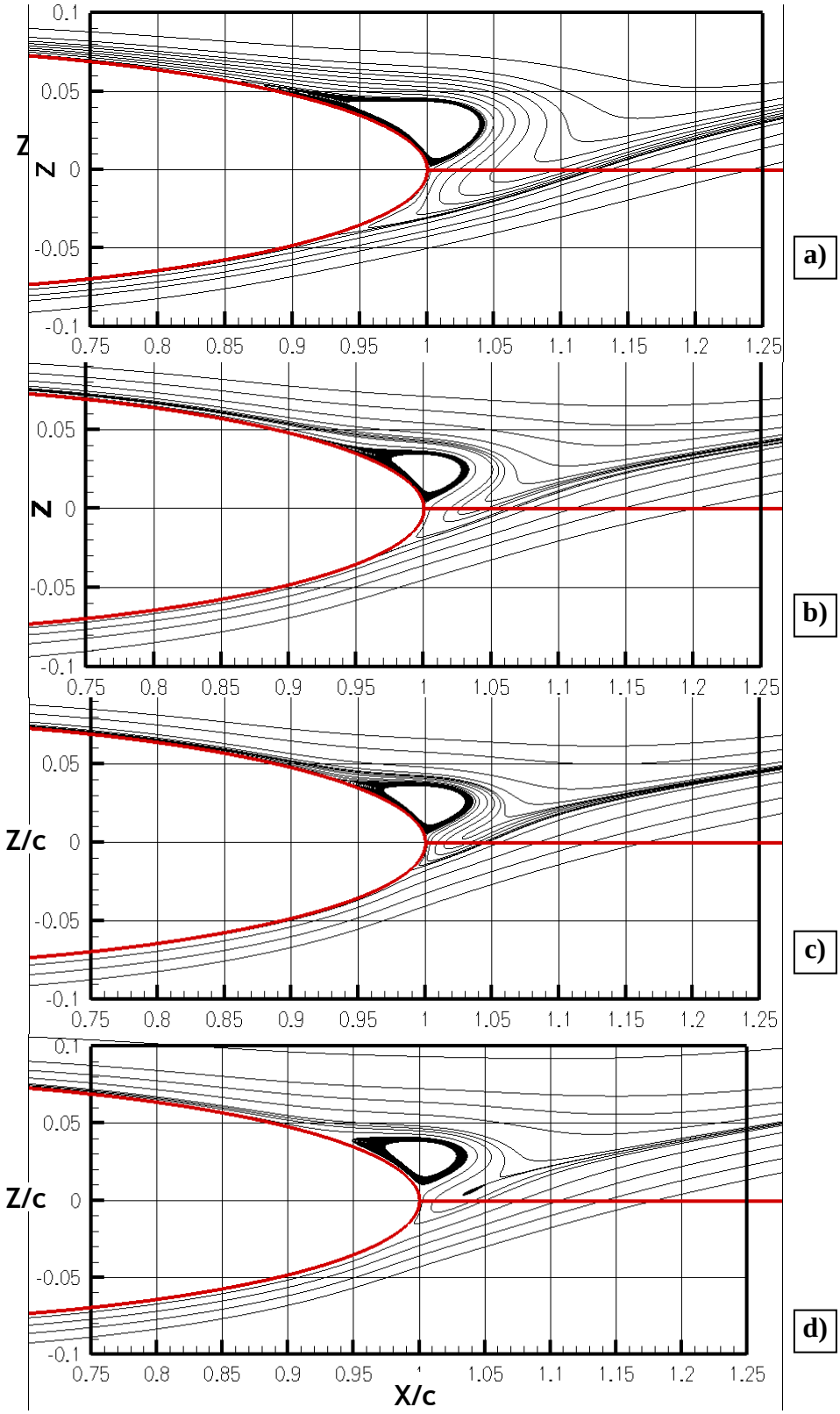

Figure 4.14 - Streamlines visualizations of vortex developments near trailing edge.
t/c = 16%, α = 10°
a) Re = $1*10^5$, b) Re = $3*10^5$, c) Re = $2*10^6$, d) Re = $8*10^6$

Figure 4.14 shows close-up views of the vortex structures aft of the trailing edge for a range of Reynolds numbers at an attack angle of 10°. These close-up views show that the vortex was largest at a Reynolds number of $1*10^5$. Also, as the Reynolds number was increased, the point at which the aft vortices separated moved closer to the airfoil trailing edge, which is locate at X/c = 1. As can be seen in Figure 4.14, formation of the aft vortex shifts backward, toward the trailing edge, as the Reynolds number increases. At a Reynolds number of $1*10^5$, formation of the aft vortex starts at a point on the suction surface located long the x-axis at approximately 86% of the airfoil chord length. At a Reynolds number of $3*10^5$, formation of the aft vortex starts at approximately 91% of the airfoil chord length. At a Reynolds number of $2*10^6$, formation of the aft vortex starts at approximately 93% of the airfoil chord length. At a Reynolds number of $8*10^6$, formation of the aft vortex starts at approximately 95% of the airfoil chord length, which was a 10% increase in percent chord. Also, as seen in Figure 4.14-d, at a Reynolds number of $8*10^6$, an additional aft vortex was formed beneath the first vortex, which flowed in an opposing direction.

In order to better understand differences in flowfield characteristics, contour plots of streamlines were produced for the range of investigated Reynolds numbers at an angle of attack of 8° and grouped together for comparison. Figure 4.15 depicts contour plots of streamlines for a 16% thick elliptic airfoil over a range of Reynolds numbers between $1*10^5$ and $8*10^6$.

As can be seen in Figure 4.15, below, flowfield characteristics at 10° angle of attack and 8° angle of attack are very similar. The primary difference to be observed was that flow separation on the aft trailing edge of the airfoil was observed was observed to increase at the higher angle of attack for a Reynolds number of $1*10^5$. This observation correlates with results for lift performance, which shows the evaluated airfoil approaching stall around 10° angle of attack for a Reynolds number equal to $1*10^5$. Presumably, this is caused by the flow being pulled a greater distance downward by the more inclined airfoil.

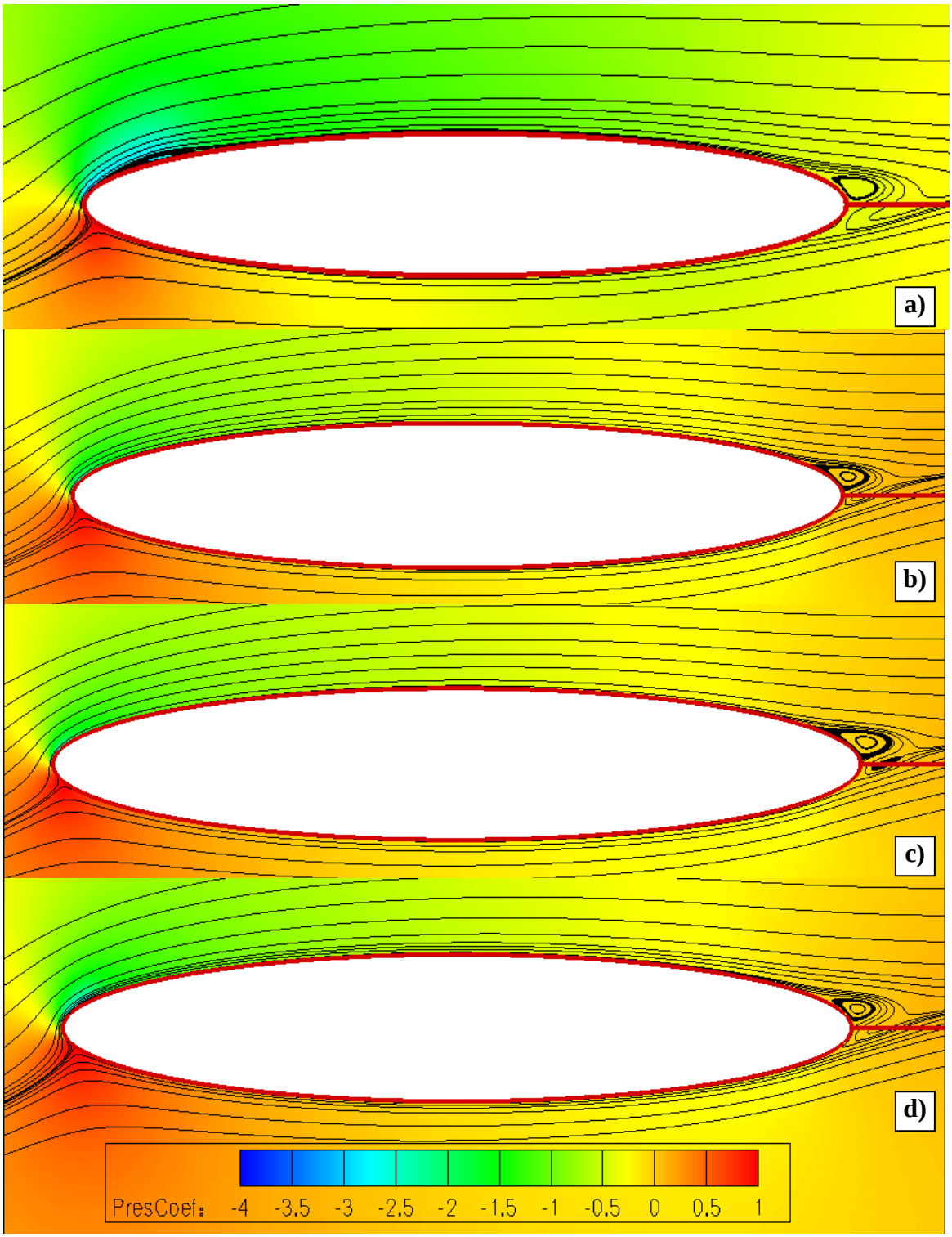

Figure 4.15 - Pressure distribution and flow streamlines around elliptic airfoil for various Reynolds numbers.
t/c = 16%, α = 8°
a) Re = $1*10^5$, b) Re = $3*10^5$, c) Re = $2*10^6$, d) Re = $8*10^6$

4.1.6. Influence of Thickness Ratio on Airfoil Lift Characteristics. In order to better understand the aerodynamic characteristics of elliptic airfoils, the influence of thickness ratio on airfoil lift characteristics was evaluated. Airfoil lift performance of an elliptic airfoil was evaluated for attack angles ranging from 0° to 20°, and thickness ratios of 5, 10, 16, 20, and 25%. These thickness ratios were chosen to show changes in aerodynamic performance for airfoils that could be used for different types of UAV applications. A thickness ratio of 5 or 10% could be applied to small UAVs or miniature UAVs. Smaller thickness ratios could also be used on high-speed UAVs to reduce drag. A full scale UAV, like the CRW UAV, would have an airfoil thickness ratio between 10 and 20%. Thickness ratios greater than 20% would be applicable for Mico-UAV's which experience very low Reynolds numbers and operate primarily in laminar flow.

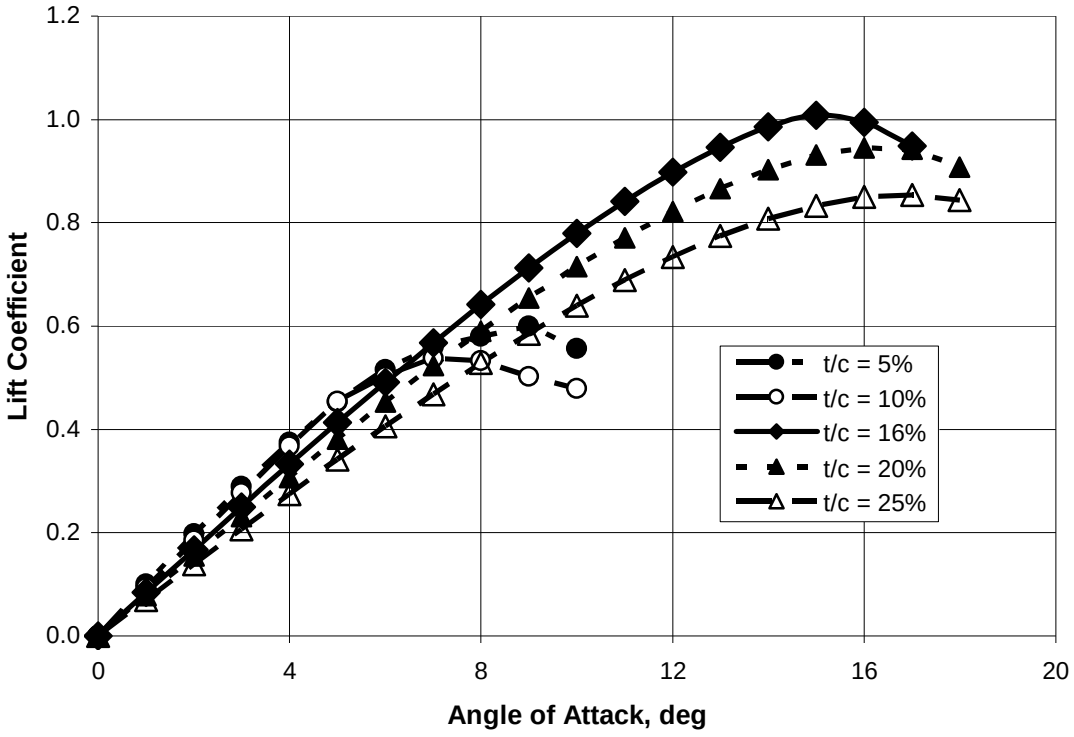

Figure 4.16 - Dependence of Lift Coefficient on angle of attack for a range of thickness ratios between 5% and 25%.
Re = $2*10^6$

Aerodynamic performance for an elliptic airfoil at a Reynolds number of $2*10^6$ was evaluated for a range of airfoil thickness ratios between 5% and 25%. Figure 4.16, above, shows the dependence of lift coefficient on angle of attack of an elliptical airfoil at a Reynolds number of $2*10^6$ over a range of airfoil thickness ratios between 5% and 25%.

As can be seen in Figure 16, for attack angles between 0° and 6°, greater lift performance was observed for lower thickness ratios. At 5° angle of attack, the difference in lift coefficient for a 5% thick elliptic airfoil over a 25% thick elliptic airfoil was observed to be 0.112, or approximately 29.4%. This was the greatest observed difference, however, the percent difference ranged up to 39.0% at 1° angle of attack. Figure 4.17 shows a zoomed in view of the dependence of lift coefficient on angle of attack for 0° to 5° range and for each of the investigated thickness ratios.

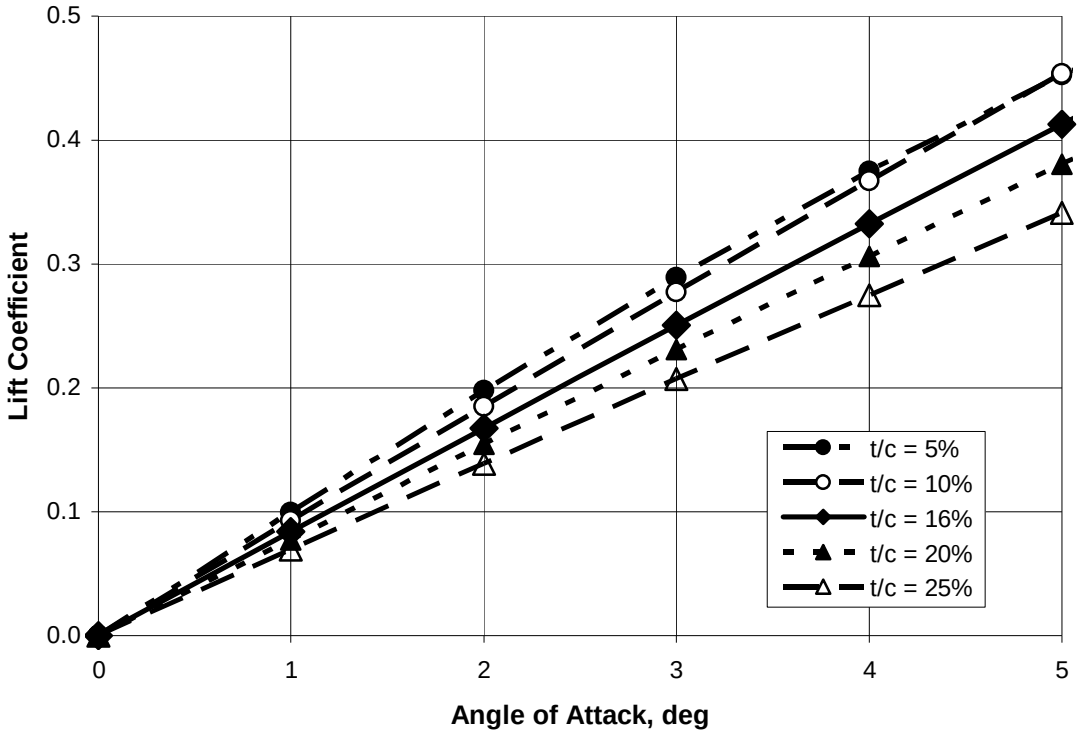

Figure 4.17 - Dependence of Lift Coefficient on angle of attack for a range of thickness ratios between 5% and 25%.
Re = $2*10^6$

As can be seen in Figure 4.17, lift slope increased as the thickness ratio decreases. However, lift slope was not observed to be linear. Table 4.2, below, shows observed values for lift slope for a range of attack angles between 1° and 5° and for a range of thickness ratios between 5% and 25%.

Table 4.2 – Lift slopes for angles of attack between 1° and 5° and a range of thickness ratios between 5% and 25%.

$Re = 2*10^6$

Angle of Attack	Thickness Ratio				
	5%	10%	16%	20%	25%
1	0.0997	0.0927	0.0839	0.0774	0.0695
2	0.0984	0.0925	0.0836	0.0771	0.0692
3	0.0913	0.0919	0.0829	0.0764	0.0685
4	0.0856	0.0899	0.0819	0.0754	0.0676
5	0.0779	0.0865	0.0805	0.0741	0.0663
Average	**0.0937**	**0.0907**	**0.0826**	**0.0761**	**0.0682**

Table 4.2 shows that the observed lift slopes were slightly non-linear and that the average lift slope, for angles of attack between 1° and 5°, increases as the thickness ratio decreases. This can also be seen in Figure 4.18, below, which shows the dependence of the average lift slope for angles of attack between 1° and 5° for a range of thickness ratios between 5% and 25%.

While lower thickness ratios outperformed higher thickness ratios in the range of angles of attack between 0° and 6°, for angles of attack greater than 6°, thickness ratios of 5% and 10% approached stall at lower attack angles than thickness ratios between 16% and 25%. Overall, a thickness ratio of 16% outperformed all other thickness ratios for attack angles greater than 6°. This can be seen clearly in Figure 4.19, which shows the dependence of observed stall angle of attack on thickness ratio at a Reynolds number of $2*10^6$ and for a range of thickness ratios between 5% and 25%.

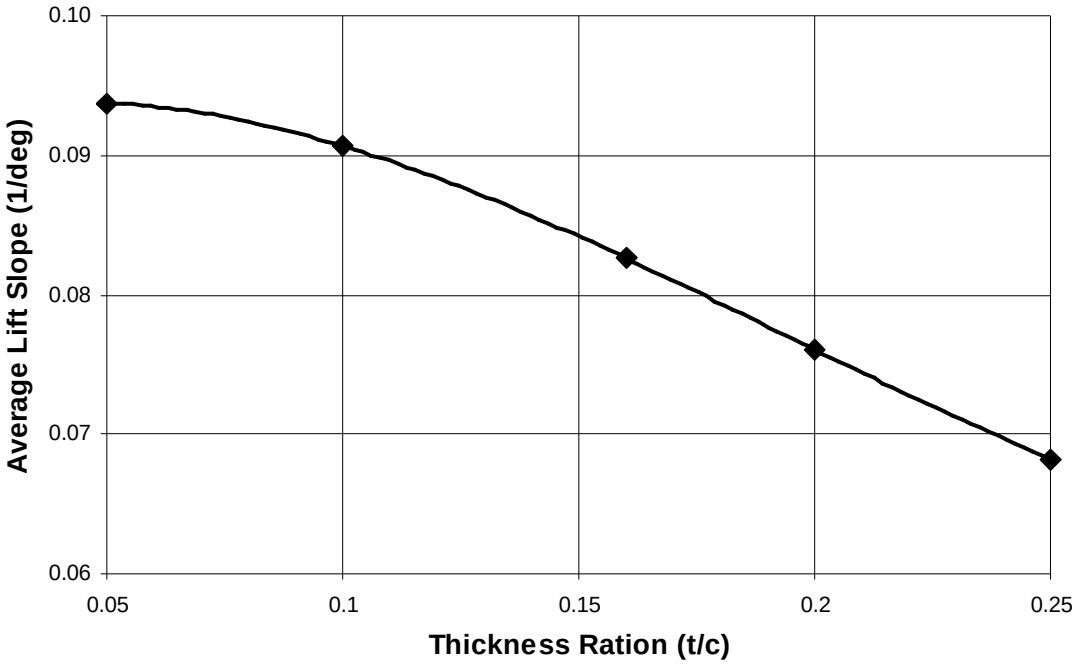

Figure 4.18 - Dependence of average lift slope on thickness ratio for angles of attack between 1° and 5°
Re = $2*10^6$

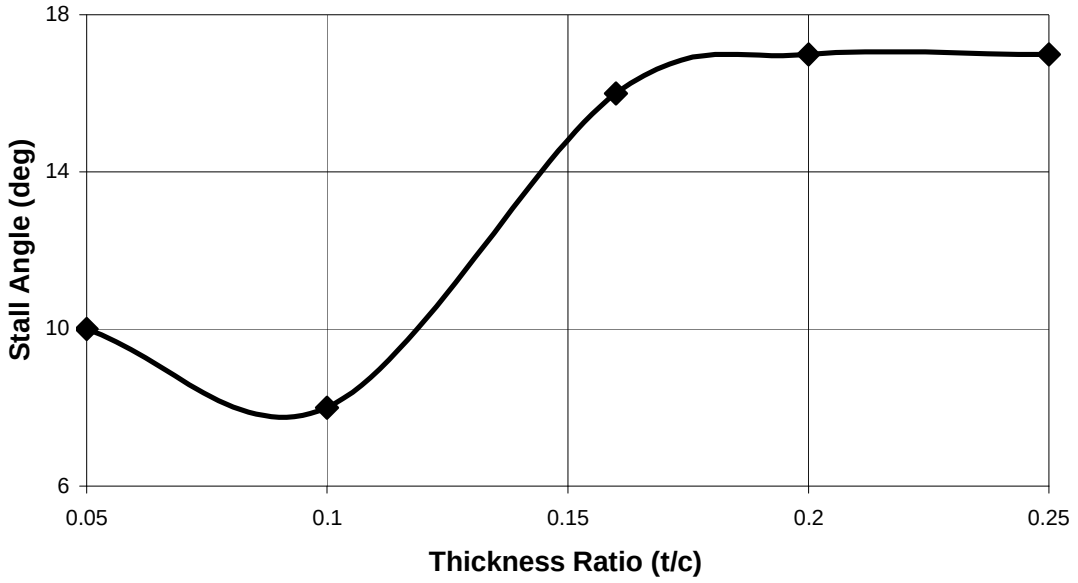

Figure 4.19 - Dependence of stall angle on thickness ratio for a range of thickness ratios between 5% and 25%.
Re = $2*10^6$

As can be seen in Figure 4.19, stall angle is greater at thickness ratios greater than 15°. Presumably the reason for small thickness ratios stalling at a lower angle is caused by flow separating from the sharp over the top of the leading edge of the airfoil. Another important characteristic to investigate is maximum lift coefficient. Figure 4.20 shows the dependence of maximum lift coefficient on thickness ratio at a Reynolds number of $2*10^6$ and for a range of thickness ratios between 5% and 25%.

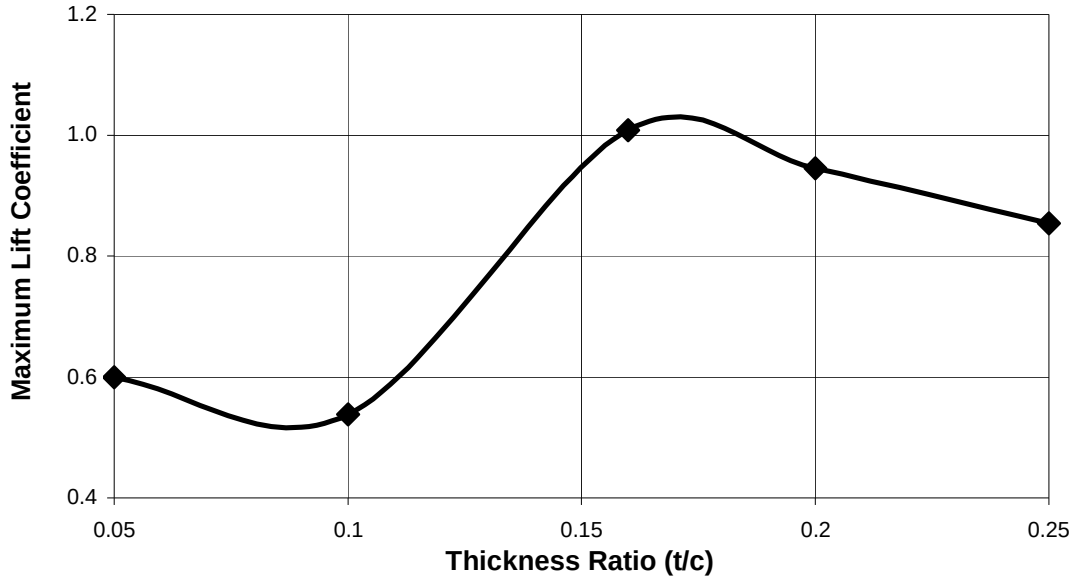

Figure 4.20 - Dependence of maximum lift coefficient on thickness ratio for a range of thickness ratios between 5% and 25%.
Re = $2*10^6$

As can be seen in Figure 4.20, maximum lift coefficient peaks at around 16% thickness ratio. This observation suggests that there is an optimal thickness ratio which would yield the highest maximum lift coefficient. This optimal thickness ration could be determined if more cases were ran to find maximum lift coefficients for elliptic airfoils with thickness ratios between 10% and 20%.

4.1.7. Influence of Thickness Ratio on Airfoil Drag Characteristics. Another aerodynamic performance characteristic investigated in the parametric study to gain a better understanding of aerodynamic performance was drag coefficient. Figure 4.21

shows the dependence of drag coefficient on angle of attack at a Reynolds number of $2*10^6$ and for a range of thickness ratios between 5% and 25%.

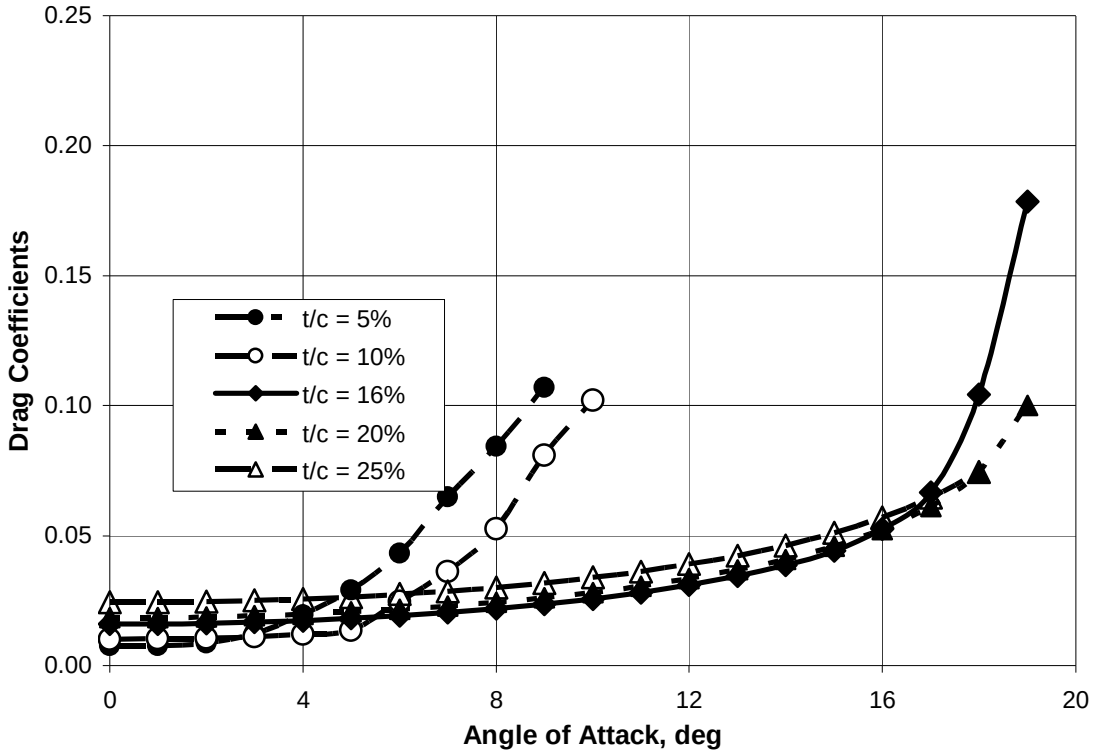

Figure 4.21 – Dependence of Drag Coefficient on angle of attack for a range of thickness ratios between 5% and 25%.
Re = $2*10^6$

As can be seen in Figure 4.21, for angles of attack less than 4°, the smallest thickness ratio, 5%, was observed to have the best drag performance, while the greatest thickness ratio, 25%, was observed to have the most drag. This observation was to be expected because thicker airfoils generally yield greater drag than thinner airfoils. However, at angles of attack greater than 4°, drag coefficient for each thickness ratio was observed to rise sharply at the angle of attack which the particular thickness ratio was observed to show stall characteristics.

In order to investigate more thoroughly the drag characteristics of elliptic airfoils for a range of attack angles between 0° and 5°, Figure 4.22 shows a zoomed in view of

the dependence of drag coefficient on angle of attack for a range of thickness rations between 5% and 25% and for a range of attack angles between 0° and 5°.

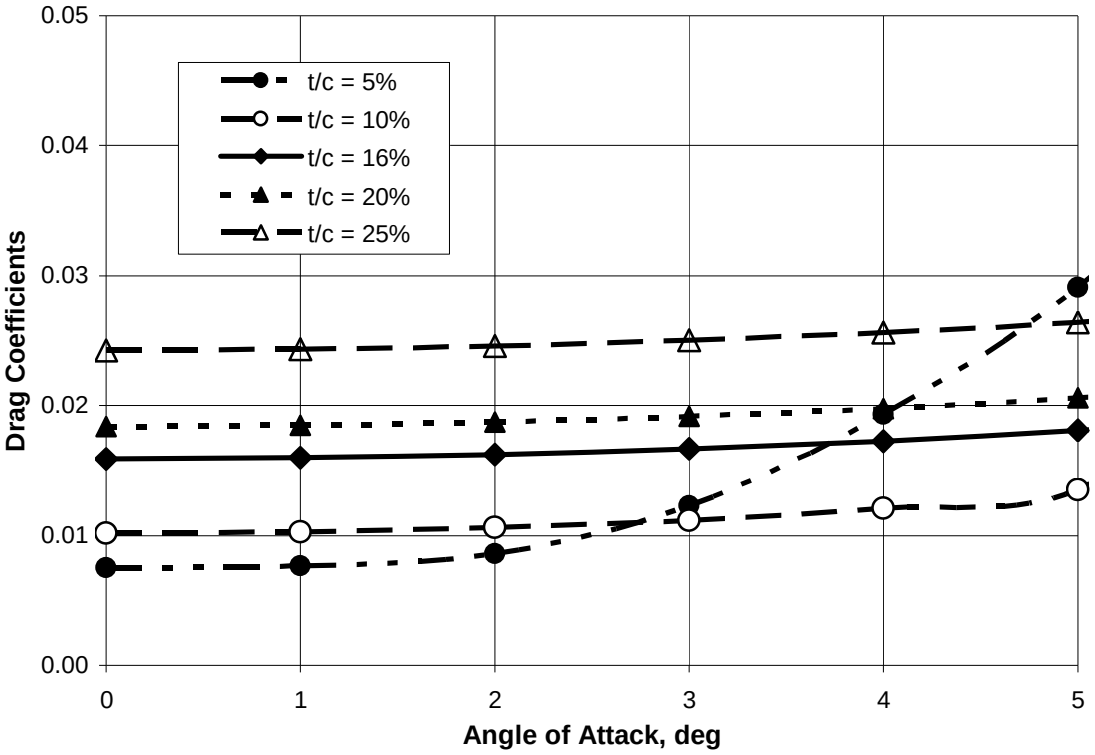

Figure 4.22 – Dependence of Drag Coefficient on angle of attack for a range of thickness ratios between 5% and 25%.
Re = $2*10^6$

As can be seen in Figure 4.22, a thickness ratio of 5% yields the lowest drag at 2° angle of attack and the worst drag performance at 5° angle of attack. This observation is due to flow separation over the leading edge of the airfoil. Drag performance of a 5% thick elliptic airfoil at 1° angle of attack is roughly 68% better than drag performance of a 25% thick elliptic airfoil at the same angle of attack.

4.1.8. Influence of Thickness Ratio on Lift to Drag Performance. In order to gain a better understanding on the overall airfoil performance, including lift and drag characteristics, lift to drag performance was considered in this investigation. Figure 4.23 shows the dependence of lift to drag ratio on angle of attack for a range of thickness ratios between 5% and 25%.

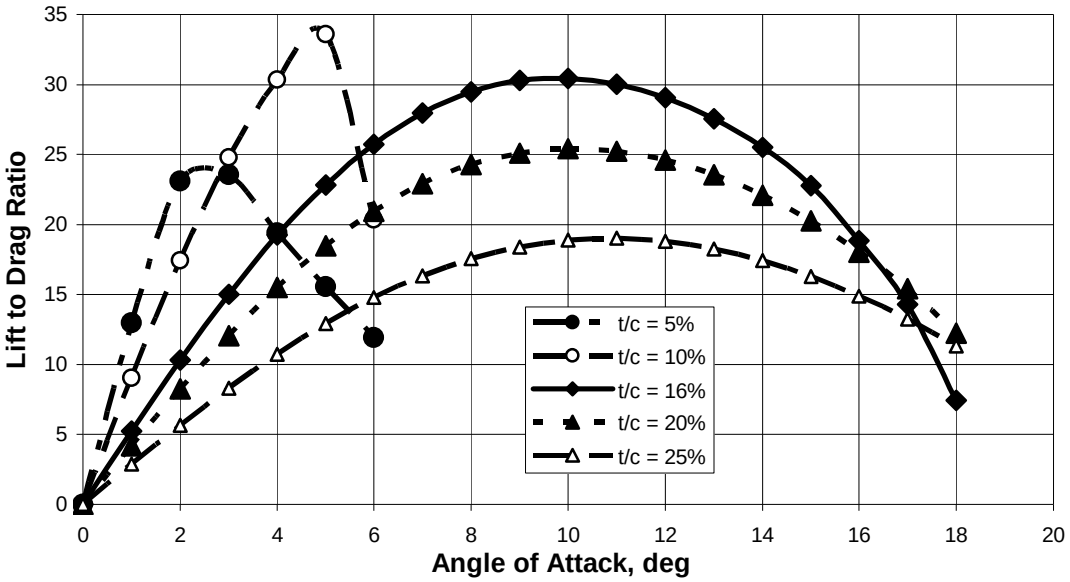

Figure 4.23 - Dependence of Lift to Drag Ratio on Angle of Attack for a Range of Thickness Ratios between 5% and 25%.
Re = $2*10^6$

As can be seen in Figure 4.23, the greatest lift to drag ratio is observed for a thickness ratio of 10%. This observation can be seen more clearly in Figure 4.24, which shows the dependence of maximum observed L/D on thickness ratio.

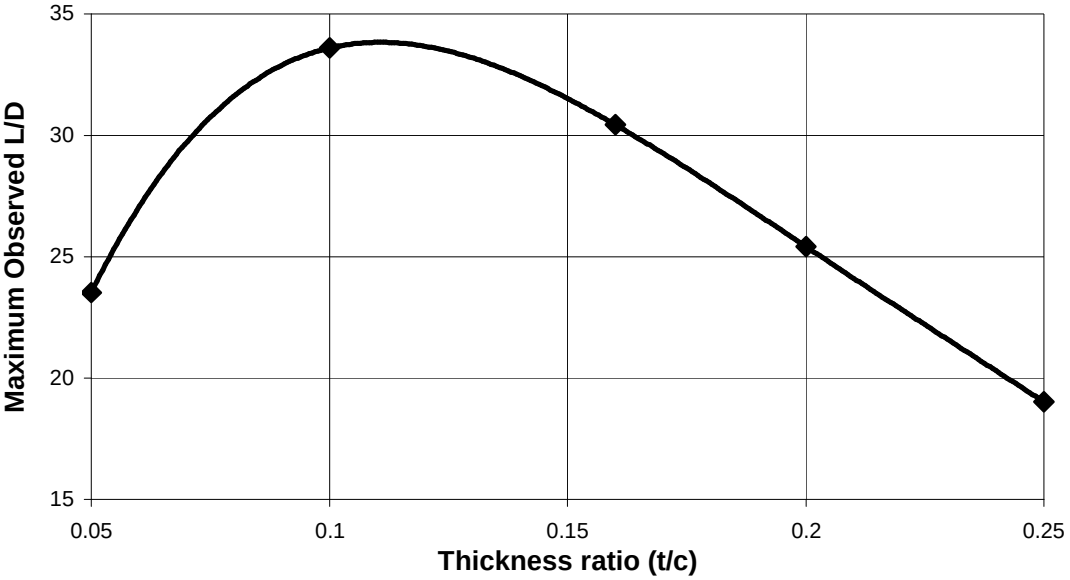

Figure 4.24 - Dependence of Maximum Observed L/D on Thickness Ratio.
Re= $2*10^6$

As can be seen in Figure 4.24, the maximum observed L/D alludes to having optimal lift to drag performance at a thickness ratio between 10% and 16 %. More investigation into the lift to drag performance for elliptic airfoils with thickness ratios between 10% and 16% would need to be conducted to validate this observation.

4.1.9. Influence of Thickness Ratio on Pitching Moment. Also investigated in this study was the influence of thickness ratio on pitching moment. Pitching moment is important to aircraft design because affects the stability and control of the aircraft. Therefore, determination of the pitching moment coefficient (C_M) has an affect on wing and tail design. The influence of Reynolds number on C_M was found employing FOMOCO to determine the dependence of C_M on thickness ratio and angle of attack. Figure 4.25 shows results obtained for C_M at a Reynolds number of $2*10^6$ and over a range of thickness ratios between 5% and 25% and angles of attack between 0° and 20°.

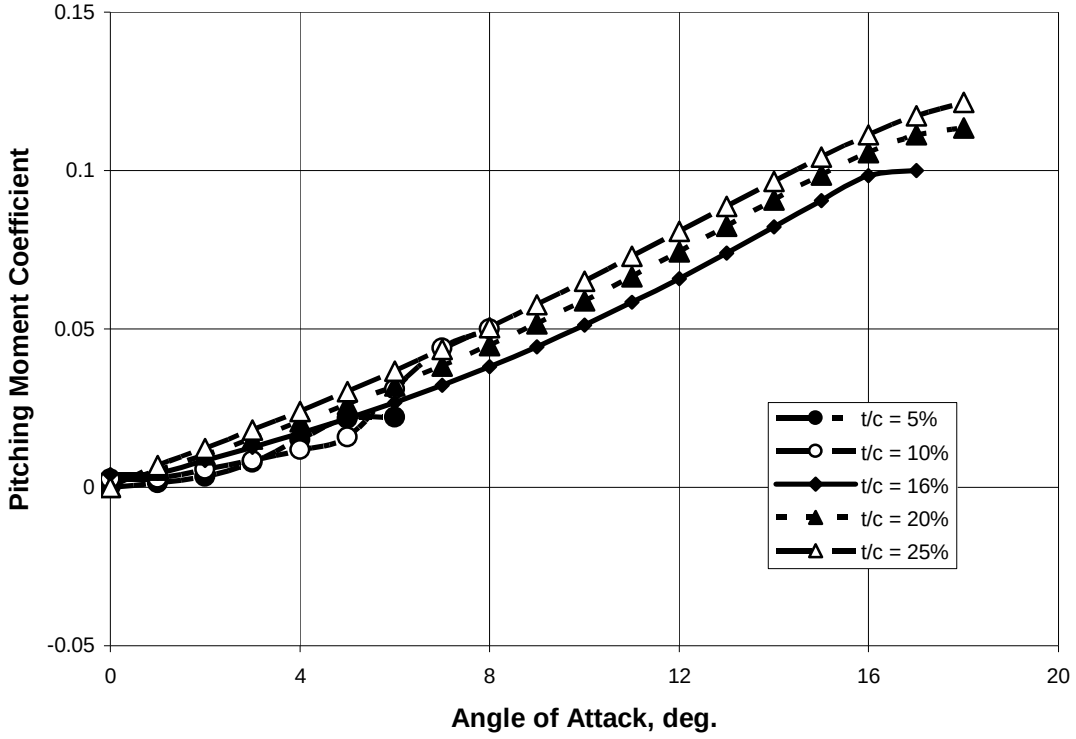

Figure 4.25 – Dependence of Pitching Moment Coefficient on Thickness Ratio. Re = $2*10^6$

As seen in Figure 4.25, the pitching moment coefficient was found to be positive for all thickness ratios, and for each thickness ratio the moment coefficient was found to increase with angle of attack. For attack angles less than or equal to 5°, the pitching moment coefficient was found to increase as the thickness ratio increased. For thickness ratios between 16% and 25%, the moment coefficient was found to increase as thickness ratio increased for all angles of attack.

4.1.10. Influence of Thickness Ratio on Flow Developments. Results obtained for the thickness ratio comparison showed the effects of changes in thickness ratio on aerodynamic performance. For attack angles between 0° and 5°, higher thickness ratios were found to decrease lift performance, for thickness ratios between 16% and 25%, which is contrary to typical sharp trailing edge airfoils that show increased performance for higher thickness ratios. Further examination into contour plots of streamlines for varying thickness ratios might show how trailing edge separation and leading edge separation bubbles affect the aerodynamic characteristics of an elliptic airfoil. Figure 4.26 shows contour plots of streamlines for an elliptic airfoil at Reynolds numbers of a $2*10^6$, attack angle of 5° for thickness ratios between 5% and 25%.

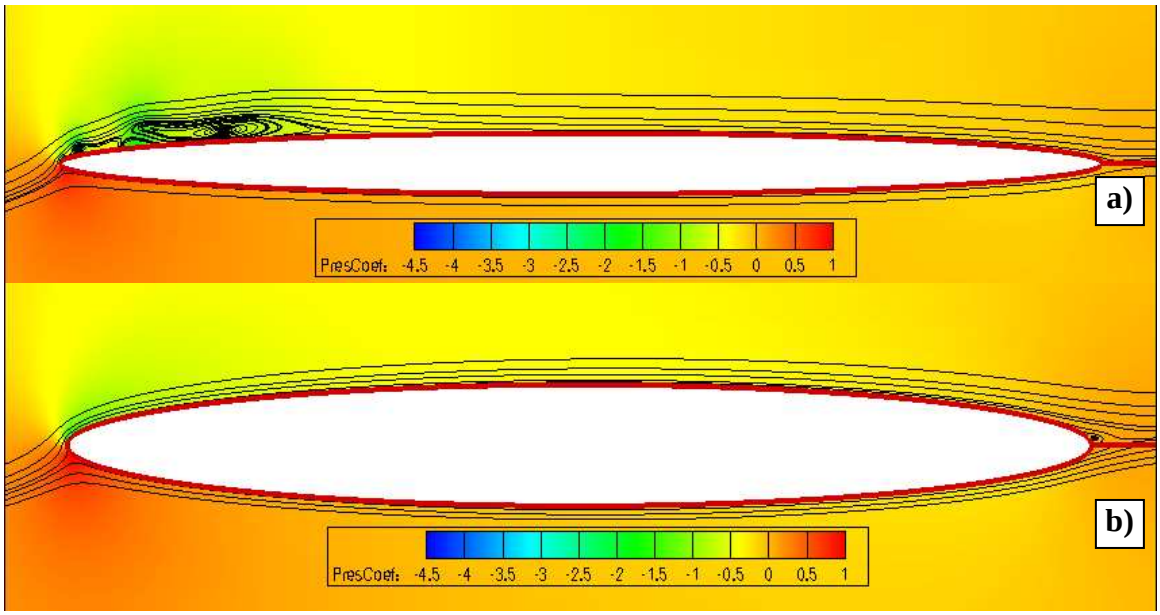

Figure 4.26 - Pressure distribution and flow streamlines around elliptic airfoil for various Reynolds numbers.
Re = $2*10^6$, α= 5°
a)t/c = 5%, b)t/c = 10%

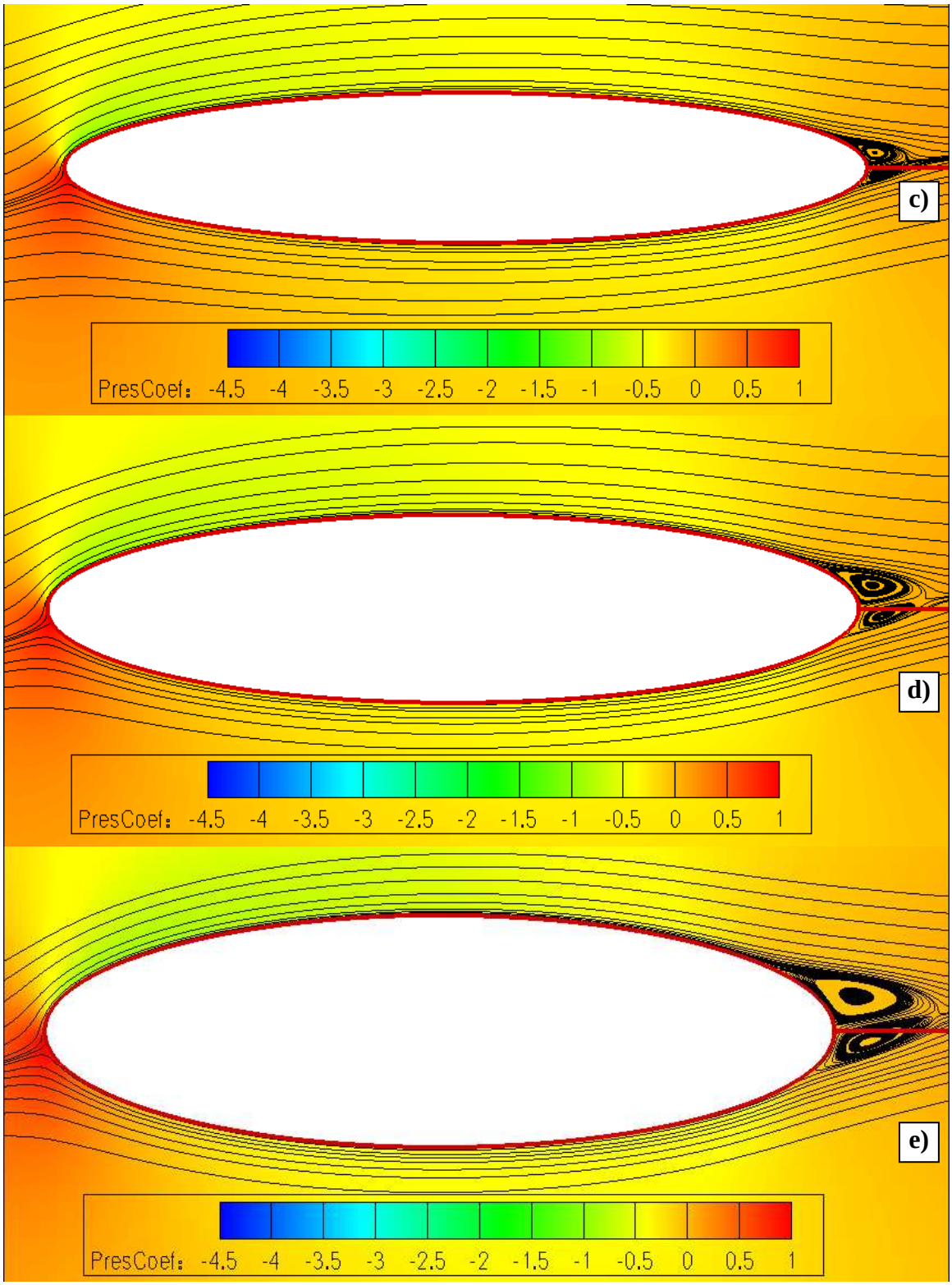

Figure 4.26 (Continued) - Pressure distribution and flow streamlines around elliptic airfoil for various Reynolds numbers.
Re = $2*10^6$, α= 5°
c)t/c = 16%, d)t/c = 20%, e)t/c = 25%

As can be seen in Figure 4.26, above, larger thickness ratios were subject to greater flow separation along the aft trailing edge. As shown in Figure 4.26-a, a 5% thick elliptic airfoil (Re = $2*10^6$ and $\alpha = 5°$), a large leading edge separation bubble was observed. A very thin separation bubble can be observed in Figure 4.26-b, which shows results for a 10% thick elliptic airfoil, however, no separation bubbles over the leading edge were observed for thickness ratios between 16% and 25%.

Elliptic airfoils with smaller thickness ratios showed higher lift coefficients and lower drag coefficients for angle of attacks in the range between 0° and 4°. This observation is supported by noting that the airfoils with smaller thickness showed less aft flow separation along with LESB formation and reattachment. While these flow characteristics are beneficial at lower angles of attack, they also cause the airfoil to observe stall and lower angle of attacks than higher thickness ratios, which decreases lift and increases drag. Figures 4.27 and 4.28 show formation of LESB for 5% and 10% thick elliptic airfoils. Due to the complexity of the turbulent flow fields in the separation bubbles, the solution would only reach “fuzzy convergence”. This results is typical when a turbulent flow condition may exist. Multiple attempts were made to obtain smooth convergence, however, no such changes allowed for smoother convergence.

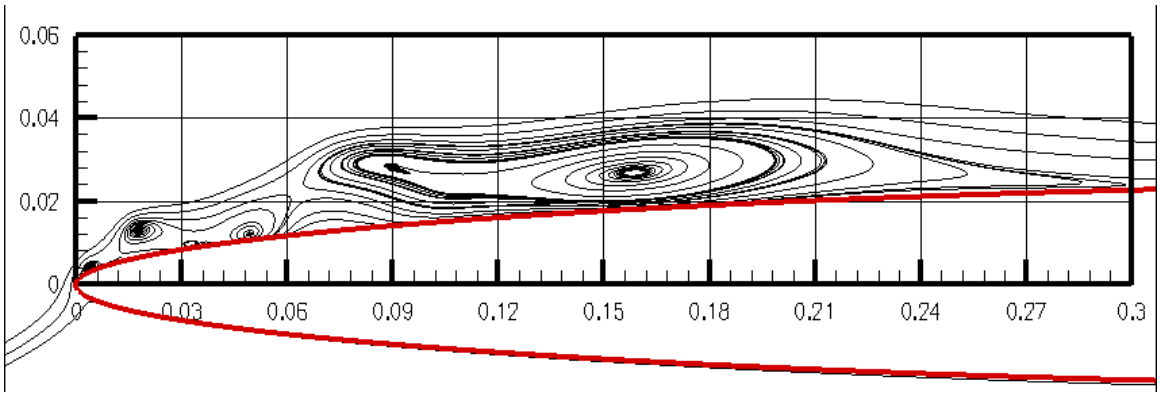

Figure 4.27 – Streamline visualizations of flow developments near the airfoil leading edge.
Re = $2*10^6$, t/c = 5%, $\alpha = 5°$

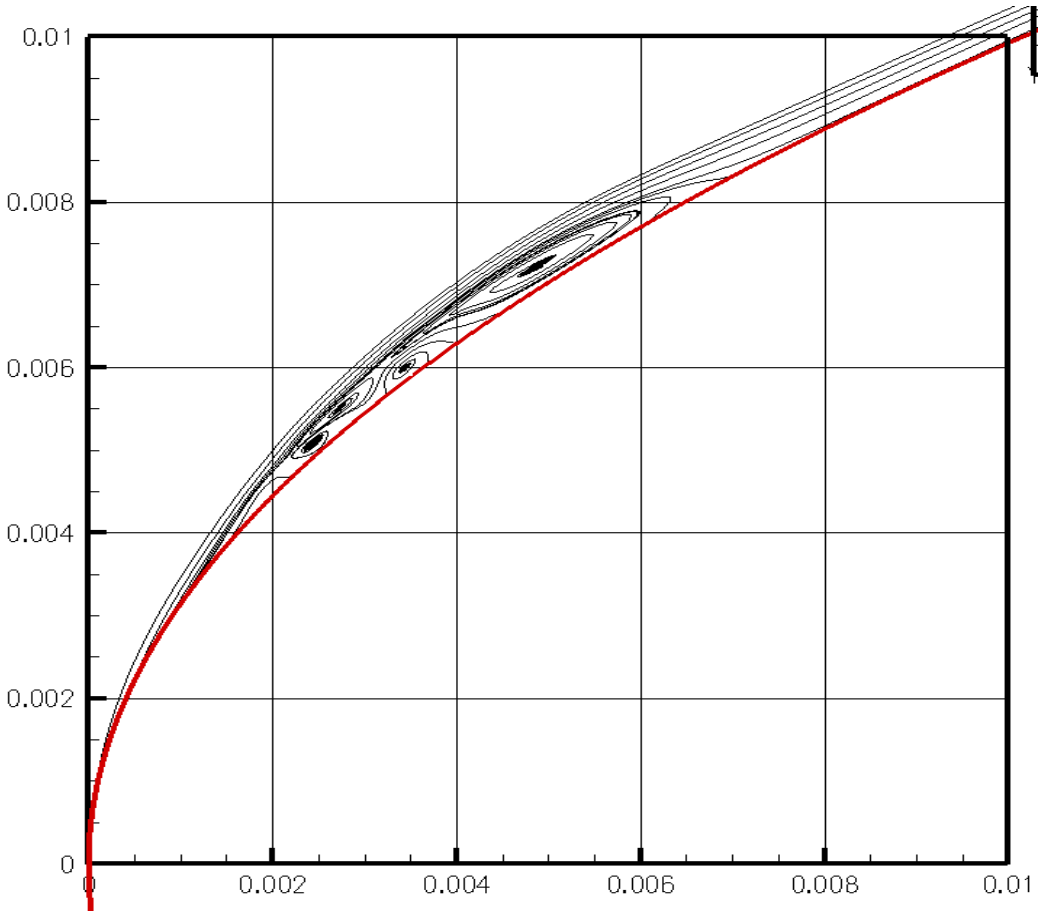

Figure 4.28 - Streamline visualizations of flow developments near the airfoil leading edge.
Re= $2*10^6$, t/c = 10%, α = 5°

The effect of the separation bubbles on the lift characteristics of an elliptic airfoil became more apparent when the surface pressure distributions were investigated. Plots of surface pressure distribution over the upper and lower airfoil surfaces showed a noticeable drop in pressure in the locale of the preciously observed separation bubbles. Figure 4.29 shows plots of surface pressure distribution for Reynolds numbers between $1*10^5$ and $8*10^6$.

Elliptic airfoils with thickness ratios between 16% and 25% were observed to have lower lift coefficients for attack angles between 0° and 5°, however, they were not subject to stall until much higher attack angles and therefore were able to achieve greater lift coefficients and retain lower drag coefficients. For attack angles of 5° and less, the thicker airfoils exhibited lower lift coefficients, most likely do to the lack of LESB

formation. Also, for attack angles of 5° and less, the thicker airfoils exhibited higher drag coefficients, which is supported by increase flow separation aft of the trailing edge. Figure 4.30 shows close-up views of vortex structures observed aft of the trailing edge for 10%, 16%, 20%, and 25% thick elliptic airfoils at a Reynolds number of $2*10^6$.

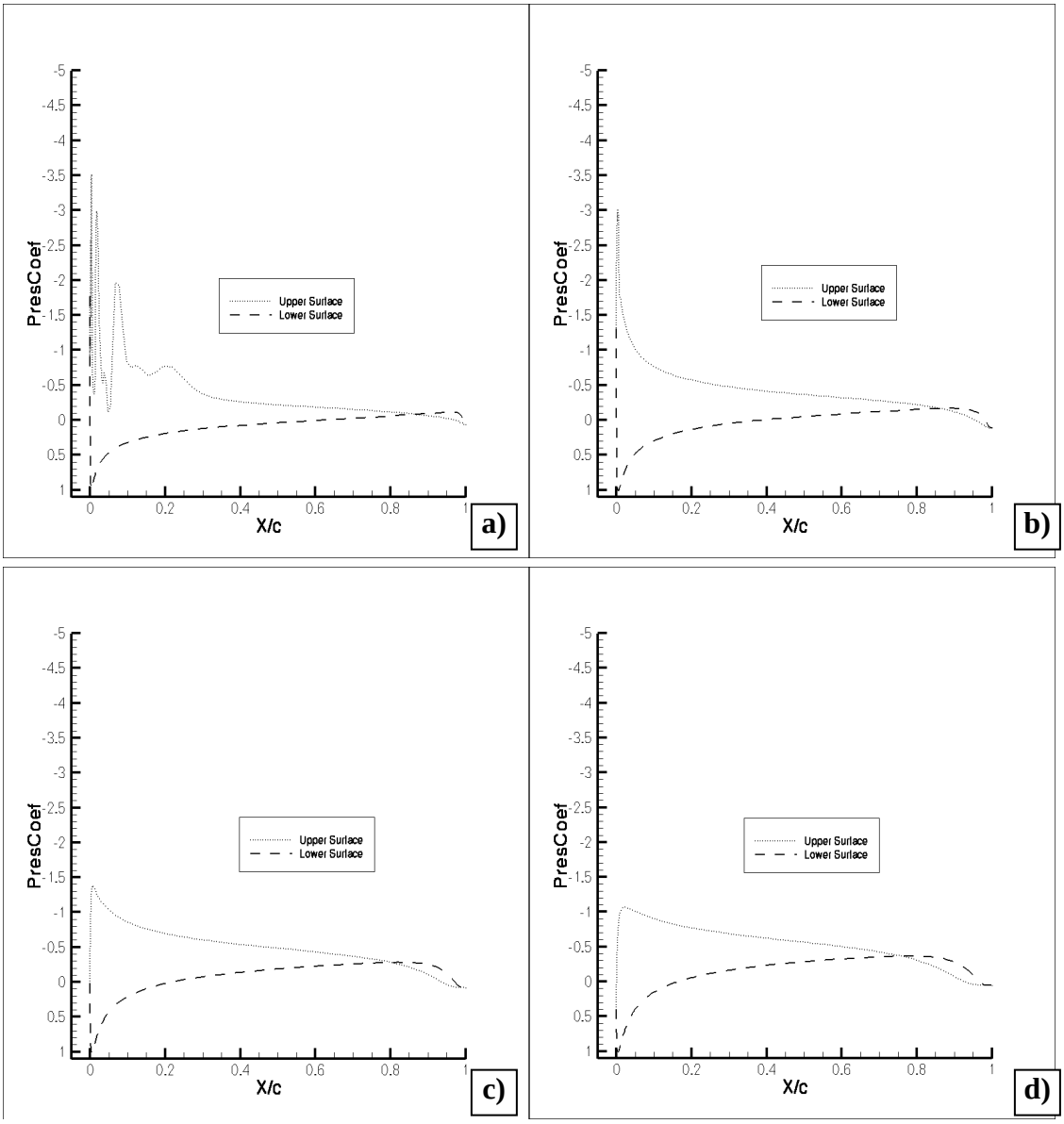

Figure 4.29 - Plots of surface pressure distribution showing pressure drops caused by separation bubbles over the leading edge.
Re = $2*10^6$, α = 5°
a) t/c = 5%, b) t/c = 10%, c) t/c = 16%, d) t/c = 20%

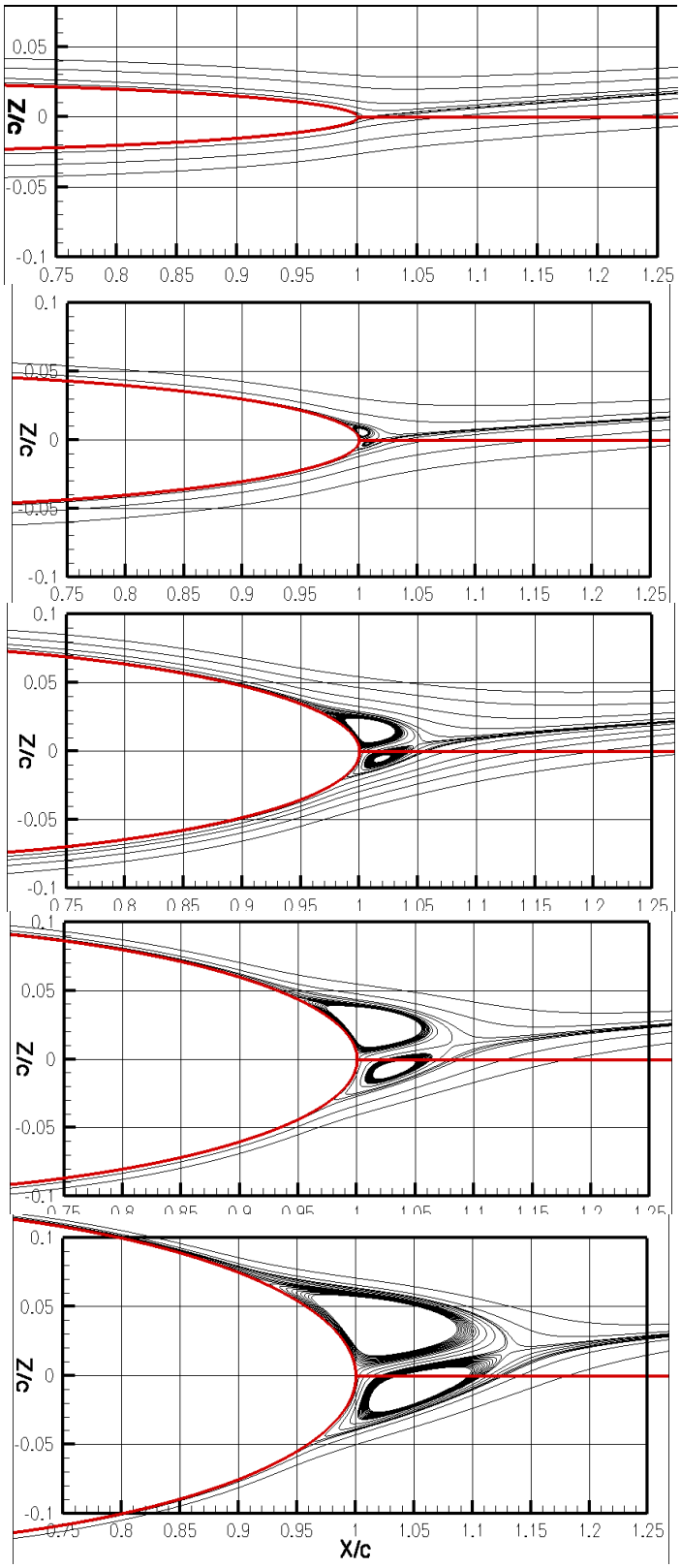

Figure 4.30 – Streamlines visualizations of vortex developments near trailing edge.
Re = $2*10^6$, α = 5°
a) t/c = 5%, b) t/c = 10%, c) t/c = 16%, d) t/c = 20%, e) t/c = 25%

As can be seen in Figure 4.30, the height of the aft vortices increased as the thickness ratio was increased. For a thickness ratio of 5%, shown in Figure 4.30-a, the vortices were so small as not to be visible at the current level of magnification. For a thickness ratio of 10%, the height of the primary vortex was approximately 2% chord of the airfoil. For a thickness ratio of 16%, the height of the primary vortex was approximately 3%. For a thickness ratio of 20% the height of the primary vortex was approximately 4%. For a thickness ratio of 25% the height of the primary vortex was approximately 6%, which was a 200% increase over the height of the primary vortex of an elliptic airfoil with a thickness ratio of 5%.

Also shown in Figure 4.30, was that the point along the upper surface of the airfoil where the aft vortex began to form moved forward as thickness ratio increased. For a thickness ratio of 10%, the vortex began to separate at approximately 99% chord of the airfoil. For a thickness ratio of 16%, the vortex began to separate at approximately 97% chord of the airfoil. For a thickness ratio of 20%, the vortex began to separate at approximately 95% chord of the airfoil. For a thickness ratio of 25%, the vortex began to separate at approximately 92% chord of the airfoil, which was a 7% chord shift in the point where the vortex began forming over that of a 10% thick elliptic airfoil.

Results obtained for 5% elliptic airfoils showed that complex vortex flow was occurring on the leading edge of the airfoil resulting in LESB formation. In order to better understand the formation of LESB as the angle of attack increases from 0° to 8°, Figure 4.31 shows contour plots of streamlines for a 5% thick elliptic airfoils at a Reynolds number of $2*10^6$ for angles of attack between 0° and 10°.

As can be seen in Figure 4.31, separation over the leading edge starts to form small bubbles at around 3° and eventually covers the entire upper surface at 8°. LESB formation starts with a small bubble on the leading edge at 3°, as seen in Figure 4.31-d, and grows to a large bubble with very turbulent flow, as seen in Figures 4.31-c through 4.31-g. At an attack angle of 7° an wake vortex begins to shed from the trailing edge, as seen in Figure 4.31-h. At 8° angle of attack, the trailing edge vortex connects with flow separation over the leading edge and covers the entire upper surface. This observation occurs well into the previously observed stall-range of attack angles.

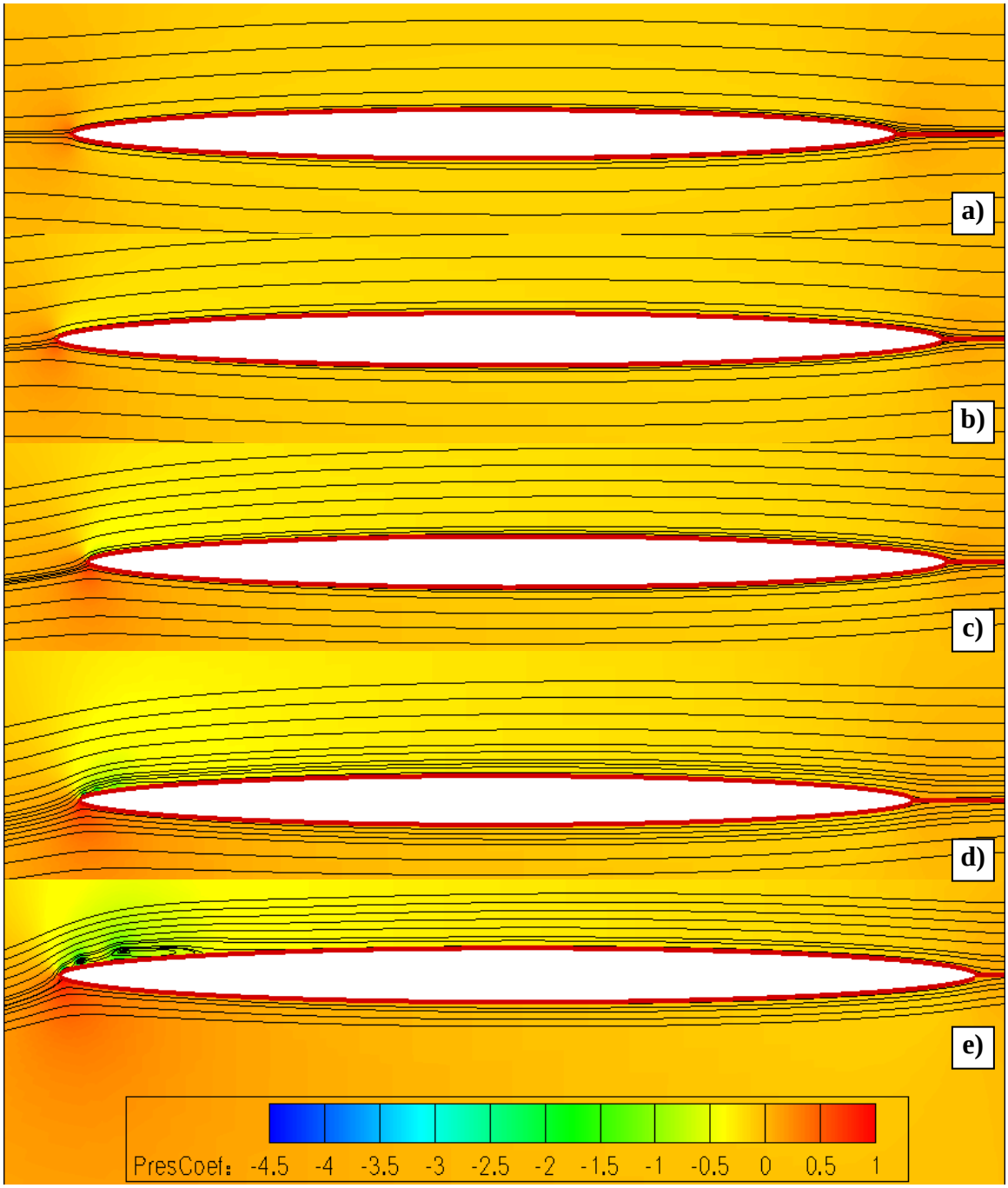

Figure 4.31 - Pressure distribution and flow streamlines around elliptic airfoil for various Reynolds numbers.

Re = $2*10^6$, t/c = 5%

a) α = 0°, b) α = 1°, c) α = 2°, d) α = 3°, e) α = 4°

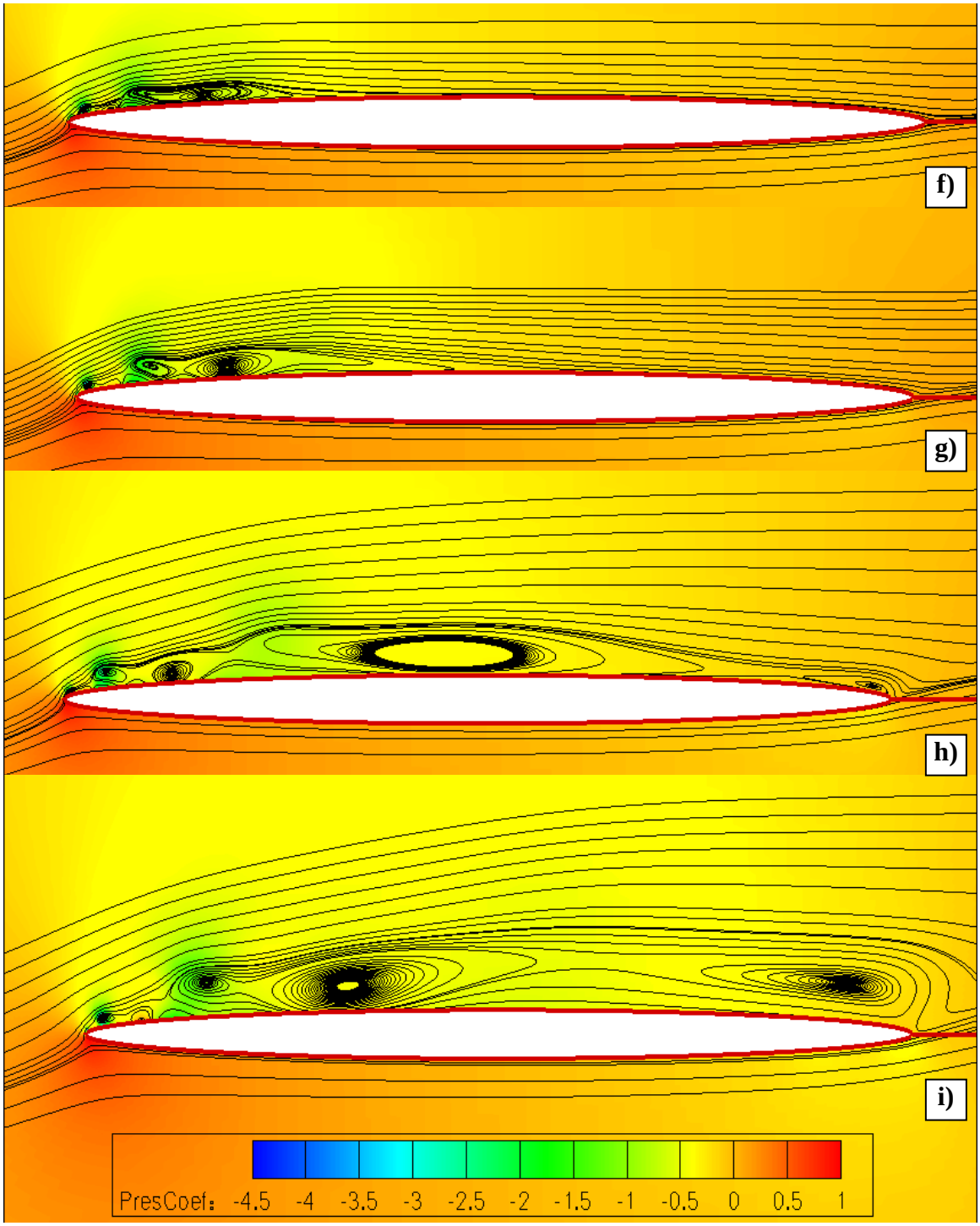

Figure 4.31 (Continued) - Pressure distribution and flow streamlines around elliptic airfoil for various Reynolds numbers.
Re = $2*10^6$, t/c = 5%
f) α = 5°, g) α = 6°, h) α = 7°, i) α = 8°

In an attempt to obtain more accurate observations of flow separation and reattachment over the leading edge for a 5% thick elliptic airfoil, an additional set of cases were investigated with grids of increased density. Figure 4.32 shows contour plots of streamlines for 5% thick elliptic airfoils at a Reynolds number of $2*10^6$ for angles of attack between 0° and 10°, which were conducted using the grids of increased density.

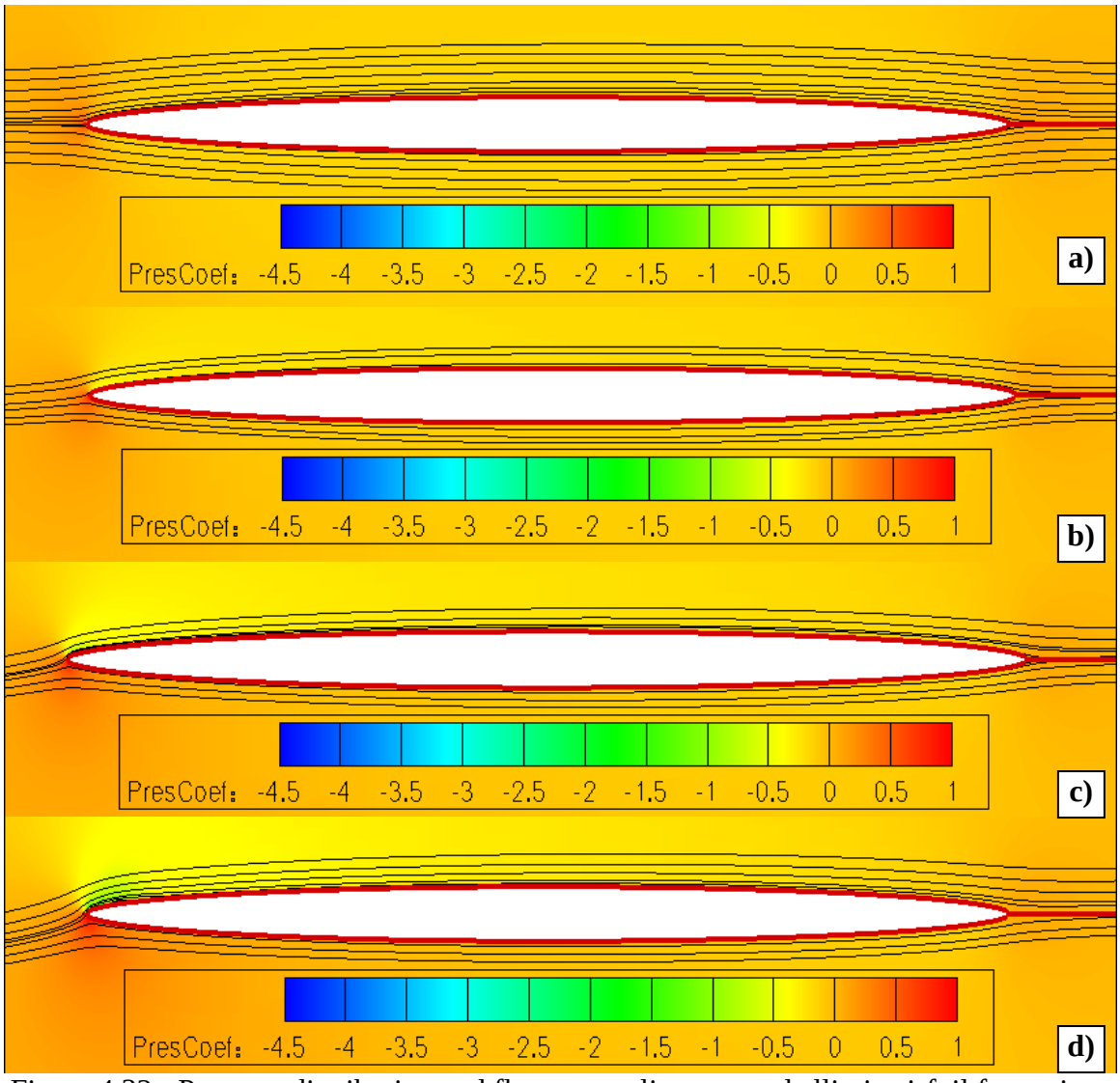

Figure 4.32 - Pressure distribution and flow streamlines around elliptic airfoil for various Reynolds numbers.
Re = $2*10^6$, t/c = 5%
a) α = 0°, b) α = 1°, c) α = 2°, d) α = 3°

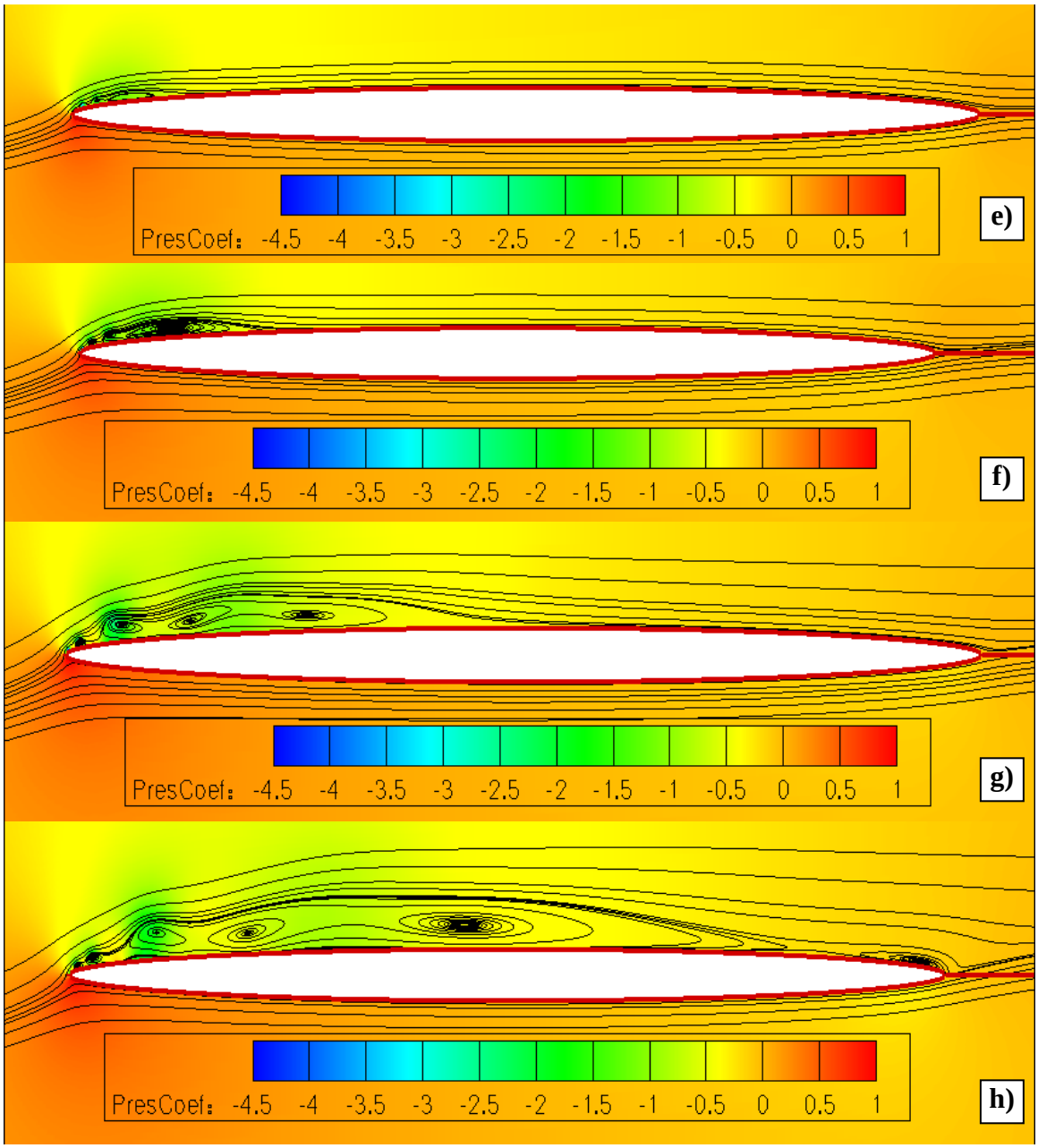

Figure 4.32 (Continued) - Pressure distribution and flow streamlines around elliptic airfoil for various Reynolds numbers.
Re = $2*10^6$, t/c = 5%
e) α = 4°, f) α = 5°, g) α = 6°, h) α = 7°

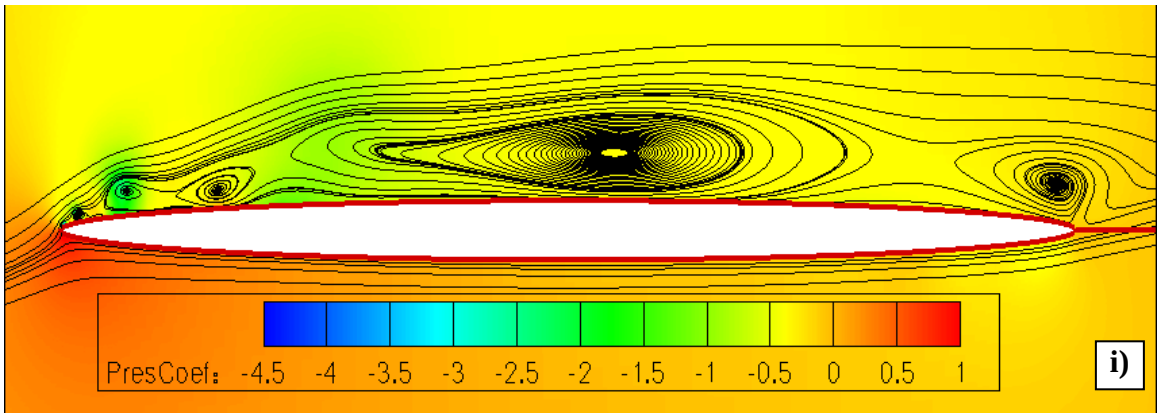

Figure 4.32 (Continued) - Pressure distribution and flow streamlines around elliptic airfoil for various Reynolds numbers.
Re = $2*10^6$, t/c = 5%
i) α = 8°

4.2. CONCLUSIONS

In this parametric study, the effects of Reynolds number, thickness ratio and attack angle on the aerodynamic characteristics of an elliptic airfoil were investigated. Reynolds numbers were evaluated for a range between $1*10^5$ and $8*10^6$ to show an identifiable effect on aerodynamic performance and are varied for a reasonable range of rotary and fixed wing flight conditions: high Reynolds numbers during rotary flight, low Reynolds numbers during transition, and medium-ranged Reynolds numbers during fixed-wing flight. Thickness ratio was evaluated for a range between 5% and 25% to account for a reasonable range of airfoil thicknesses that would be used on UAVs. Angle of attack was evaluated from 0° to 20° in order to analyze aerodynamic characteristics up to stall condition.

Aerodynamic performance for a 16% thick was determined for attack angles ranging from 0° to 20° and for Reynolds numbers between $1*10^5$ and $8*10^6$. As shown previously, for angles of attack between 0° and 8°, lower Reynolds numbers showed improved lift performance over higher Reynolds numbers. The average lift slope was shown to drop significantly between Reynolds numbers of $1*10^5$ and $2*10^6$, however, for Reynolds numbers greater than $2*10^6$, average lift slope showed little to no change. Although Reynolds numbers in the 10^5 range showed better lift performance for attack angles between 0° and 8°, greater lift performance was observed Reynolds numbers in the 10^6 range at attack angles greater than 8°. Results showed that significant

improvements in stall characteristics were obtained for Reynolds numbers in the 10^6 range. Reynolds numbers in the 10^5 range resulted in maximum lift coefficients in the 0.84 to 0.86 range, while the maximum lift coefficient observed at a Reynolds number of $2*10^6$ showed to be greater than 1.0. However, at a Reynolds number of $8*10^6$, a maximum lift coefficient of 0.96 was observed, which resulted in only a 10% increase over the results observed in the 10^5 Reynolds number range and a 5% drop from results obtained at a Reynolds number of $2*10^6$. Presumably, this data would show that there is an optimal Reynolds number to be found in between $3*10^5$ and $2*10^6$. More analysis would need to be conducted for Reynolds numbers in the $3*10^5$ and $2*10^6$ range to determine the optimal value.

In consideration of drag performance, for angles of attack between 0° and 12°, the highest investigated Reynolds number, $8*10^6$, was observed to have the lowest drag coefficient. For angles of attack greater than 12°, better drag performance was observed at a Reynolds number of $2*10^6$ than at a Reynolds number of $8*10^6$. This observation was due to the fact that a 16% thick elliptic airfoil at a Reynolds number of $8*10^6$ stalled at a lower angle of attack than at a Reynolds number of $2*10^6$. Based on a comprehensive comparison of lift-to-drag ratio, airfoil performance was shown to improve as Reynolds number was increased. At higher Reynolds numbers, the evaluated airfoil was able to achieve greater maximum lift coefficients through prevention of stall until higher angles of attack. Also, the evaluated airfoil was observed to produce less drag as Reynolds number was increased. These factors combined to cause the lift to drag ratio to improve as Reynolds number was increased. Overall, a Reynolds number of $8*10^6$ was found to be the best of the evaluated Reynolds numbers in drag and lift to drag performance in a range of attack angles applicable to UAVs.

In this study, some interesting conclusions were made regarding the influence of Reynolds number on airfoil performance. Flow separation was found to be dependent on Reynolds number. In regards to the formation of laminar separation bubbles, the cross sectional area of the laminar separation bubbles increased as Reynolds number decreased. The formation of laminar separation bubbles was found to have an effect on lift performance. At attack angles less than 8°, lift performance increased by LSB formation. For attack angles greater than 8°, flow separation over the leading edge was not observed

to reattach to the airfoil, thus causing stall characteristics. Also, the flow structures of vortices downstream of the trailing edge were affected by Reynolds number. As the Reynolds number was increased, the point at which flow separation occurred on the airfoil surface moved closer to the airfoil trailing edge. The vortex structure had the largest cross sectional area at a Reynolds number of $1*10^5$. Flow separation over the trailing edge and formation of vortices downstream of the airfoil were found to coincide with increases in drag as Reynolds number was decreased.

Aerodynamic performance for an elliptic airfoil at a Reynolds number of $2*10^6$ was evaluated for a range of airfoil thickness ratios between 5% and 25%. As shown previously, for attack angles between 0° and 6°, greater lift performance was observed for lower thickness ratios. Lift slope was shown to increase as the thickness ratio decreased. While lower thickness ratios outperformed higher thickness ratios in the range of angles of attack between 0° and 6°, for angles of attack greater than 6°, thickness ratios of 5% and 10% approached stall much sooner than thickness ratios between 16% and 25%. Overall, a thickness ratio of 16% outperformed all other thickness ratios for attack angles greater than 6°. As was previously shown, maximum lift coefficient peaks at around 16% thickness ratio. This observation suggests that there is an optimal thickness ratio which would yield the highest maximum lift coefficient. This optimal thickness ratio could be determined if more cases were ran to find maximum lift coefficients for elliptic airfoils with thickness ratios between 10% and 16%.

Concerning the influence of thickness ratio on drag performance, for angles of attack less than 4°, the smallest thickness ratio, 5%, was observed to have the best drag performance, while the greatest thickness ratio, 25%, was observed to yield the most drag. At attack angles between 4° and 5°, a 10% thick elliptic airfoil was found to have the best drag performance. At angles of attack between 6° and 16°, a 16% thick elliptic airfoil was found to have the best drag performance. Regarding lift-to-drag ratio, a 10% thick elliptic airfoil was shown to have the greatest lift-to-drag ratio, approximately 34, which occurred at and angle of attack of 5°. However, L/D dropped sharply for attack angles greater than 5°. For attack angles of 6° and greater, a 16% thick elliptic airfoil was shown to have the best L/D. Overall, data for L/D showed that an even greater L/D might

be attainable for thickness ratios between 10% and 16%, however, more research would be needed to reach this conclusion.

In regards to the influence of thickness ratio on flow development around the airfoil, laminar separation bubbles were found to form over the leading edge of airfoils with smaller thickness ratios, and the separation of flow over the trailing edge and formation of vortices downstream of the airfoil was found to be affected by thickness ratio. The effect of the separation bubbles on the lift characteristics of an elliptic airfoil became more apparent when the surface pressure distributions were investigated. Plots of surface pressure distribution over the upper and lower airfoil surfaces showed a noticeable drop in pressure in the locale of the preciously observed separation bubbles. Flow separation over the trailing edge and formation of vortices downstream of the airfoil were found to coincide with increases in drag as thickness ratio was increased.

In conclusion, results of the parametric studies into Reynolds number and thickness ratio showed trends in aerodynamic performance characteristics of elliptic airfoils for a range of Reynolds number between $1*10^5$ and $8*10^6$ and a range of thickness ratios between 5% and 25%. These trends tended to show that best lift and drag performance of the evaluated parameter values was a Reynolds number of $2*10^6$ and a thickness ratio of 16%. Observation of the results in this study showed that better performance might be obtained for a parameter range of Reynolds numbers between $3*10^5$ and $2*10^6$ and a parameter range of thickness ratios between 10% and 16%. More in depth investigation into the aerodynamic characteristics of elliptic airfoils in these ranges of Reynolds number and thickness ratio would need to be conducted to determine if an optimal Reynolds number and optimal thickness ratio might exist and what the optimal Reynolds number and thickness ratio might be.

In order to promote future advancements in rotor/wing design and development, more research into the influence of Reynolds number and thickness ratio on aerodynamic performance and flow characteristics of elliptic airfoils is needed. One of the more significant needs for investigation is in-depth CFD and wind tunnel analysis of elliptic airfoils in Reynolds number and thickness ratio ranges which would be applicable to UAVs. Based on the results of this investigation, the range of parameters which would yield the most useful results would be Reynolds numbers between $3*10^5$ and $2*10^6$ and

thickness ratios between 10% and 16%. Also, CFD analysis employing more accurate turbulence models and higher density volume grids would be greatly beneficial to more closely simulate and evaluate flow developments about and elliptic airfoil.

5. CONCLUSIONS AND OUTLOOK

5.1. CONCLUSIONS

Investigation into advancements in UAV technology, primarily the CRW-UAV concept, resulted in the conclusion that a parametric study into the aerodynamic performance of elliptic airfoils would benefit future research in CRW technology development and could serve as a tool for new rotor-wing design concepts. Therefore, the flow problem investigated in this study was turbulent viscous flow developments over elliptic airfoils. This study investigated two-dimensional flowfields surrounding elliptic airfoils for a range of parameters. These parameters included: Reynolds number, angle of attack, and thickness ratio.

The methodology used to conduct the CFD analysis was validated by comparing results for aerodynamic characteristics of a symmetrical, 16% thick elliptic airfoil at a Reynolds number of 3×10^5 to results of wind tunnel testing conducted by Kwon [21]. The purpose of a validation test case was to verify that the flowfield solution results obtained from CFD analysis compared similarly to experimental data. Results of the validation test case showed that flowfield simulations generated using CFD analysis compared similarly to results obtained using experimental wind-tunnel analysis. This conclusion allowed for reasonable verification of the methodology employed to simulate flowfields about an elliptical airfoil using CFD analysis.

Once the CFD analysis techniques and methodology had been validated, the parametric study of elliptical airfoil performance was conducted. Reynolds number was evaluated at values of $1*10^5$, $3*10^5$, $2*10^6$, and $8*10^6$, to show a reasonable range of rotary and fixed wing flight conditions. Thickness ratio was evaluated for a range between 5% and 25% to account for a reasonable range of airfoil thicknesses that would be used on UAVs. Angle of attack was evaluated from 0° to 20° in order to analyze aerodynamic characteristics up to stall condition.

Results of the parametric study into Reynolds number showed that for angles of attack between 0° and 8°, Reynolds numbers in the 10^5 range showed improved lift performance over Reynolds numbers in the 10^6 range. However, greater lift performance was observed Reynolds numbers in the 10^6 range at attack angles greater than 8°. Results

showed that significant improvements in stall characteristics were obtained for Reynolds numbers in the 10^6 range. For Reynolds numbers greater than $2*10^6$, higher Reynolds numbers showed a decrease in lift performance. These observations were found to correspond to formation of laminar separation bubbles shown in flowfield visualizations and surface pressure distributions. Also, the evaluated airfoil was observed to produce less drag as Reynolds number was increased. Correspondingly, flowfield visualizations showed that flow separation over the trailing edge and formation of vortices downstream of the airfoil were found to coincide with increases in drag as Reynolds number was decreased. These factors combined to cause the lift to drag ratio to improve as Reynolds number was increased. Overall, a Reynolds number of $8*10^6$ was found to be the best of the evaluated Reynolds numbers in drag and lift to drag performance in a range of attack angles applicable to UAVs.

Results of the parametric study into thickness ratio showed that for attack angles between 0° and 6°, greater lift performance was observed for lower thickness ratios. However, for angles of attack greater than 6°, thickness ratios of 5% and 10% approached stall much sooner than thickness ratios between 16% and 25%. Overall, a thickness ratio of 16% outperformed all other thickness ratios for attack angles greater than 6°, outperforming higher and lower thickness ratios. Analysis of drag performance and lift-to-drag performance also showed that better performance might be attainable for thickness ratios between 10% and 16%, however, more research would be needed to reach this conclusion. Also, these observations were supported by flowfield visualizations, as flow separation over the trailing edge and formation of vortices downstream of the airfoil were found to coincide with increases in drag as thickness ratio was increased.

5.2. FUTURE WORK

A significant amount of work has been conducted to study flow past elliptic cylinders. Most of this work was not conducted within parameter ranges which would be applicable to UAV design and development. However, some work with elliptic airfoils which could be applied in UAV design has been conducted. Kim studied turbulent viscous flow over elliptic cylinders using two-dimensional, incompressible, Navier-Stokes equations for a limited range of thickness ratios and Reynolds numbers. Also,

Kwon and Park have investigated vortex flow structures and aerodynamic characteristics using wind tunnel testing for a single thickness ratio and Reynolds number. Kwon found that vortex shedding aft of a thin elliptic airfoil had a significant affect on lift and drag forces; and aerodynamic characteristics of elliptic airfoils have been found to differ greatly from the characteristics of conventional airfoils. In his study, Kwon noted that an accurate judgment on the origination of wake structures could not be made using results from wind tunnel tests alone which only show velocity profiles, and Kwon went on to suggest that more further work regarding wake vortex structures could more clearly indicate laminar to turbulent boundary layer transition over elliptic airfoils.

In this study, some interesting conclusions were made regarding trends in aerodynamic performance characteristics of elliptic airfoils for a range of Reynolds number between $1*10^5$ and $8*10^6$ and a range of thickness ratios between 5% and 25%. Results of the parametric study of elliptic airfoils tended to show that an optimal Reynolds number and an optimal thickness ratio may exist which would yield the best lift and drag performance for an elliptic airfoil. Observation of the results in the study showed that these optimal performance parameters might exist in a range of Reynolds numbers between $1*10^6$ and $3*10^6$ and in a range of thickness ratios between 10% and 16%. Additional investigation of elliptic airfoils in the observed ranges might prove beneficial in future design and development of rotor-wing aircraft which employ elliptic airfoils to achieve VTOL and fixed-wing, high-speed flight.

In addition to more in-depth investigations into the trends of aerodynamic characteristics for elliptical airfoils in the above specified parameter ranges, more investigation into the aerodynamic characteristics of flowfields surrounding elliptic airfoils would be needed to better understand the causes of observed trends. As observed in this study, aerodynamic characteristics are most greatly affected by trailing edge vortices and leading edge separation bubbles. An important fact to note is that a more suitable turbulence model than the one employed in this study would be needed to accurately solve and plot the shedding of trailing edge vortices and the formation of leading edge separation bubbles. A more complete grid convergence study and a more in-depth validation study would both need to be conducted to develop better techniques and methodology for aerodynamic analysis of elliptic airfoils. As better computational

resources become available, more computationally involved techniques and methodology (Higher grid densities, Detached Eddy Simulation,…) could be utilized to study the aerodynamic characteristics of flowfields about elliptic airfoils.

More aptly, the results of this investigation could be used in the design and development of future rotor/wing aircraft. Aerodynamic performance characteristics could be used size rotor/wing geometry including chords and thicknesses, as well as design speeds. Also, computational methods developed in this study could be employed along with more accurate turbulence models and higher density grids to better predict aerodynamic performance and more closely simulate complex flow developments. In addition, the visualizations of flow developments provided in this study could be compared to future CFD or wind-tunnel analyses for reference or validation.

BIBLIOGRAPHY

[1] Wilson, J. R., "UAVs a Worldwide Roundup," in Aerospace America. June, 2003

[2] Cross, Peter, *Conceptual Design, Development, and Simulation of a Tilt-Duct Unmanned Aerial Vehicle with Vertical Takeoff and Landing Capabilities,* Published by the author, 2006.

[3] http://www.boeing.com/ids/advanced_systems/hummingbird.html , Copyright 1995 - 2007 Boeing. Accessed March 2007.

[4] http://www.northropgrumman.com/unmanned/index.html , Copyright 2007 Nothrop Grumman Corporation. Accessed March 2007.

[5] http://www.naval-technology.com/projects/firescout/ , Copyright 2007 SPG Media Limited. Accessed March 2007.

[6] http://www.aurora.aero/tactical/GoldenEye-100.html , Copyright Aurora Flight Sciences Corporation. Accessed March 2007.

[7] http://www.spacewar.com/reports/Aurora_GoldenEye_80_Makes_Successful_First_Flight_999.html , Copyright 1995-2006 SpaceDaily. Accessed March 2007.

[8] "Eagle Eye Pocket Guide," Edited by Dave Wyatt. Copyright 2005 Bell Hellicopter Textron Inc.

[9] http://www.globalsecurity.org/military/systems/aircraft/x-50.htm , Copyright 2000-2007 GlobalSecurity.org, Accessed March 2007.

[10] http://www.boeing.com/news/frontiers/archive/2002/may/ts_pw.html , Copyright 2002 The Boeing Company. Accessed March 2007.

[11] http://www.boeing.com/news/frontiers/archive/2005/june/ts_sf04.html , Copyright 2005 The Boeing Company. Accessed March 2007.

[12] Boeing X-50. (2007, February 20). In *Wikipedia, The Free Encyclopedia*. Retrieved 06:24, March 5, 2007, from http://en.wikipedia.org/w/index.php?title=Boeing_X-50&oldid=109525161

[13] Sikorsky S-72. (2007, February 25). In *Wikipedia, The Free Encyclopedia*. Retrieved 06:23, March 5, 2007, from http://en.wikipedia.org/w/index.php?title=Sikorsky_S-72&oldid=110889810

[14] Mitchell, Clark A. and Vogel, Barbara J., "The Canard Rotor Wing (CRW) Aircraft – A New Way to Fly," AIAA/ICAS International Air and Space Symposium and Exposition, July 2003, AIAA 2003-2517. Copyright 2003.

[15] Pandya, S. A. and Aftosmis, M. J., "Computation of External Aerodynamics for a Canard Rotor/Wing Aircraft," AIAA Paper 2001-0997. January 2001.

[16] Zahm, A. F., Smith, R. H., and Louden, F. A., "Forces on Elliptic Cylinders in Uniform Air Stream," NACA Report No. 289, NACA TR-315, 1929.

[17] Schubauer, G. B., "Air Flow in the Boundary Layer on an Elliptic Cylinder," NACA Report No. 652, 1939.

[18] Kaplan, Carl, "Two-Dimensional Subsonic Compressible Flow past Elliptic Cyllinders," NACA Report No. 624, 1938.

[19] Hantsche, W. and Wendt, H., "The Compressible Potential Flow past Elliptic Symmetrical Cylinders at Zero Angle of Attack and with no Circulation," NACA Technical Memorandum No. 1030, 1942.

[20] Johnson, S. A., Thompson, M. C., and Hourigan K., "Flow Past Elliptical Cylinders at Low Reynolds Numbers," Australasian Fluid Mechanics Conference, Published by the Author, December 2001.

[21] Kwon, Kijung, and Park, Seung O., "Aerodynamic Characteristics of an Elliptic Airfoil at Low Reynolds Number," AIAA 2005-4762, Copyright 2005.

[22] Kim, M. S., "Unsteady Viscous Flow over Elliptic Cylinders at Various Thickness with Different Reynolds Numbers," *17th AIAA Computational Fluid Dynamics Conference,* AIAA 2005-5130, Copyright 2005.

[23] Johnson, Forrester T., Tinoco, Edward N. and Yu, N. Jong, "Thirty Years of Development and Application of CFD at Boeing Commercial Airplanes, Seattle," *16th AIAA Computational Fluid Dynamics Conference,* AIAA 2003-3439, Copyright © 2003 by The Boeing Company.

[24] Norton, Keith Edward, *A Computational Study of the Flow Fields around Supersonic Airfoils and Subsonic Speeds,* Published by the author, 2006.

[25] W.M. Chan, I.T. Chin, and P.G. Buning, "User's manual for the HYPGEN Hyperbolic Grid Generator and the HGUI Graphical User Interface," NASA TM 108791, October, 1993.

[26] P.G. Buning, D.C. Jespersen, T.H. Pulliam, G.H. Klopfer, W.M. Chan, J.P. Slotnick, S.E. Krist, and K.J. Renze, "OVERFLOW User's Manual : Version 1.8aa," NASA, April, 2003.

[27] TecPlot User's Manual, Version 10, Amtec Engineering, Inc., Bellevue, Washington, December 2003.

[28] Hoerner, S. F., and Borst, H. V., *Fluid-Dynamic Lift,* Second Edition, Published by L. A. Hoerner, 1985.

VITA

Tim Assel was born in Holt, Missouri on January 9th, 1984. Assel grew up on a farm outside of Cameron, Missouri, where he received elementary and secondary education, as well as being active in the community and the First Baptist Church. Developing early on an aptitude for math and science and an interest in space and aviation, he attended the University of Missouri – Rolla to pursue a Bachelor's degree in Aerospace Engineering.

While an undergraduate student at UMR, Assel participated in and served in leadership positions for many extra-curricular activities including: American Institute of Aeronautics and Astronautics (Chair, Vice-Chair, and Secretary), Society of Flight Test Engineers (President and Secretary), Advanced Aero-Vehicle Group (Treasurer, Aerodynamics Lead, and Controls Lead), Missouri-Rolla Satellite Team (Program Manager) and the 1st Responder's Design Competition Team (Team Leader); as well as participating in the Missouri-NASA Space Grant Consortium and Opportunities for Undergraduate Research Experience program. After graduating in May of 2002, Assel continued his studies as a Chancellor's Fellow at the University of Missouri – Rolla, receiving an M.S. in Aerospace Engineering in December of 2007.